Characterisation of human TASK-1 mutations in atrial fibrillation

W. E. Perfect
ID: 18907934

A thesis submitted to the University of Kent for degree of

Masters of Science by Research

2019

Supervised by Prof. A Mathie

Medway School of Pharmacy
Anson Building
Central Avenue
Chatham Maritime
Kent ME4 4TB

Declaration

No part of this thesis has been submitted in support of an application for any degree or other qualification of the University of Kent, or any other University or Institution of learning.

Signed: ……..

Date: ……..

Acknowledgements

I would like to state my appreciation for the support and guidance provided by my supervisor Prof. Alistair Mathie, throughout the course of this investigation.

I would further like to extend gratitude to Dr. Emma Veale for the help and support you have given me throughout the course of this project, and your guidance throughout the molecular biology contained within this thesis. Additionally, I thank you for your primer designs and ideas you have donated to me.

To Dr. Kevin Cunningham I say thanks the early experiences of patching and cell culture that you gave to me and further for the TASK models you have allowed me to use. To Dr. Yvonne Walsh I thank you for your time and patience in teaching me to 'properly patch'; and for your sanity I must drain with all my ridiculous questions. Alessia, I thank you for your friendly chat and laughs that we have had in lab. And Robyn, I thank for your help with the confocal microscopy, and I wish you the best of luck on your new engagement.

I express much love to my family: Mum, Dad, Shannon and George; all of whom I know will never care to read this thesis, but would always be there for me if I need them. I additionally honor my Nan, who sadly passed during the duration of this project, but who wise words, love and support will never be forgotten.

To Jack Burchmore, I applaud that the last year has somehow been a success and thank you for every second you have sacrificed in helping with the creation and maintenance of Mill Barn Equestrian. Let's hope there are many more successful years to come!

Abstract

Atrial fibrillation (AF) is the most common cardiac arrhythmia, affecting over two million Americans and this is set to triple by 2050, incurring an estimated U.S. treatment cost of $6.65 billion yearly. AF is a chronic condition associated with electrical changes within the heart that are related to atrial remodeling caused by variation in gene expression. The TWIK related acid sensitive potassium channel 1 (TASK-1, $K_{2P}3.1$) is a protein with the ability to induce AF. The manifestation of TASK-1 induced AF has been categorized by three factors: incorrect protein trafficking, defective $K_{2P}3.1$ channel assembly and TASK-1 electrophysiological dysfunction. However, the genomic variations that can induce these changes is not well documented, and so this project is aimed at characterising TASK-1 in human AF.

This was conducted by the creation of mutant TASK-1 constructs pathogenic in AF. These included mutation of a transmembrane domain (V123L), and two Kozak mutations (-3A>U and -4G>A). These mutants were proposed to effect channel conformation and protein translation. For those reasons these mutations were picked for investigation, along with a C-terminally truncated protein, and a N-terminally mutated protein as to investigate the effects of phosphorylation sites and 14.3.3 binding in the trafficking of the protein. These constructs were individually or co-expressed on the membrane of tsA-201 cells; where they underwent electrophysiological analysis and confocal microscopy imaging.

Overall TASK-1 mutants were shown, to present themselves in varied states. The C-terminus truncation and -3A mutations suggested an increased expression, by providing a significant increase in current compared to the wildtype. Whilst V123L proved to be potentially pathogenic, by demonstrating a significantly decreased current plus a significantly depolarized reversal potential. However, the mutational effects of V123L were rectified by heterodimerization with wildtype TASK-1, as would occur in native atrial tissue. Additionally, TASK-1 proved dominant in heterodimer formation with TASK-3, reducing the current amplitude close to that of TASK-1 homodimers, yet, the reversal potential was between the two reversal potential figures for homodimers of TASK-1 and TASK-3.

Confocal imaging experiments showed that wildtype TASK-1 channels were expressed at the cell membrane. However, both the N-terminus and Kozak mutations imaged, proved even localization at the membrane, with no intracellular retention visible, suggesting that by use of another protocol, a quantifiable increase in expression maybe provided compared to wildtype.

Contents

List of figures

List of tables

Abbreviations

µl – Microliter
Å – Angstrom
Ach – Acetylcholine
AF - Atrial Fibrillation
AP - Action Potential
APD – Action potential duration
APD_{50} – Action potential duration at 50%
APD_{90} – Action potential duration at 90%
bpm -Beats per min
Ca^{2+} - Calcium ion
cDNA – complementary DNA
Cl^- - Chloride ion
C_m – Cell membrane capacitance
CMR – Cell mask red
DNA – Deoxyribonucleic acid
ECG – Electrocardiogram
E_x – Equilibrium potential (of ion X)
GCPR – G coupled protein receptor
GFP – Green fluorescence protein
GHK – Goldman – Hodgkin's – Katz equation/potential
Gq – Guanin nucleotide binding protein (G-protein)
GΩ - Giga Ohm
HBS – Heaps buffer solution
HRV – Heart rate variability
I – Current (Amps)
I_f – Funny current
K^+ - Potassium ion
K_{2P} – Two-pore domain K^+ channel
$K_{2P}3.1$ - TWIK-related acid sensitive K^+ channel 1
KCNK3 – Gene encoding TASK-1
KCNK9 – Gene encoding TASK-3
K_{ir} – inwardly rectifying potassium channel
K_v – Voltage gated K^+ channel
LQTS - Long QT Syndrome
Ml – milliliter
Mm – millimeter
mmHg – Millimeters of mercury
mV – Millivolts
MΩ - Mega Ohm
Na^+ - Sodium ion
ng – Nanogram
nM – Nanometer
^oC – degrees Celsius
P – Pore forming domain
pA – Pico -Amp
PBS – Phosphate buffer saline
PCR – Polymerase chain reaction
pF – Pico-Farah
PO – Channel open probability
RMP – Resting membrane potential
RNA – Ribose nucleic acid
Rpm – Resolutions per min
SAN - Sinoatrial Node
ssDNA – Single stranded DNA
TASK-1 - TWIK-related acid sensitive K^+ channel 1
TASK-3 - TWIK-related acid sensitive K^+ channel 3
TM – Transmembrane domain
V – Voltage (Volts)
VF – Ventricular fibrillation

1 Introduction

1.1 The heart

1.1.1 Human heart

The mammalian heart is composed of two sides that are divided by a septum and four muscular chambers. The two top blood-receiving chambers are known as Atria, and the two lower more muscular blood-ejecting chambers are the Ventricles. Most mammalian species employ a double circulatory system – pumping blood through both pulmonary and systematic systems, and additionally engage the same vasculature, valves and conduction system, as seen in figure 1.1.1.1.

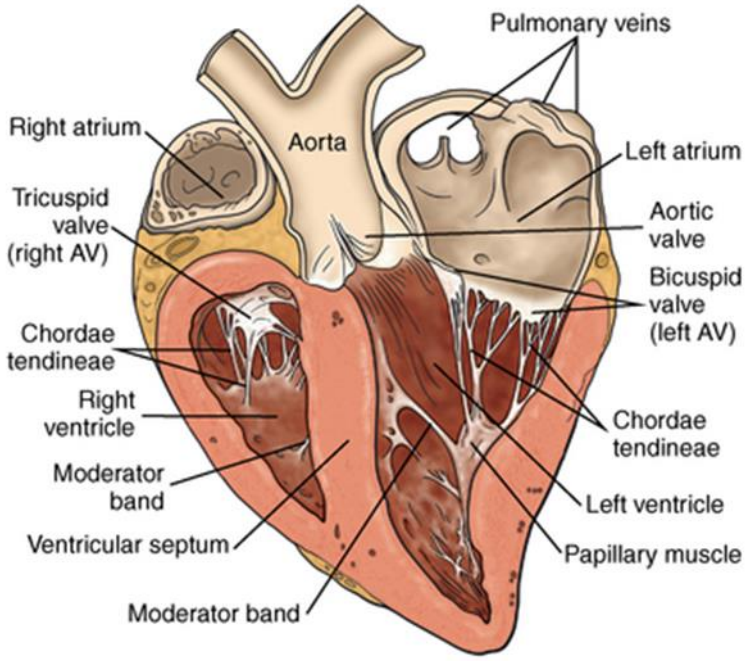

Figure 1.1.1: Figure to show the cross-sectional structure of the heart, presenting all chambers, valves, and main vessels [Marr, 2010].

Atrioventricular semi-lunar valves that prevent back flow upon contraction of the chambers separate the Atria and Ventricles of the heart, contributing to larger and stronger blood flow through the organ. These contractions are resultant of a depolarizing Action Potential (AP) stimulus, as initiated in the Sinoatrial Node (SAN); coordinating the hearts chambers, maintaining sinus heart rhythm, and characterizing physiological features of the heart, such as Heart rate (HR), as summarized in table 1.1.2.1. Nether the less, the complexity of this electrical system allows great potential for the hearts contractions to become disorganized; allowing dysrhythmia and inducing cardiac conditions such as Long QT Syndrome (LQTS) and Atrial Fibrillation (AF).

1.1.2 Mammalian hearts and research

Cardiac structure is proven similar amongst most mammalian species, and as section 1.1 describes, mammals have evolved hearts that employ a double circulatory system and engage the same vasculature, valves and conduction system seen in figures 1.1.1.1 and 1.2.6.1.

Further, the similarity of the mammalian heart means that drugs and external influences have equal ability to adapt cardiac function in the same manner across many species. For this reason, animal models such as the rat are predominantly used in human cardiac research. The rat is frequently chosen based upon the simple husbandry they desire, the fact they are ethically disposable and the close relationship between human and rat function systems.

However, the equine cardiac system is another heart model that proves of use, especially when contemplating Atrial fibrillation as a dysfunctional target. Further, considering the two-pore domain acid sensitive potassium channel 1 (TASK-1), the equine model of the protein provides greater similarity to the human analogue than the rat. More so, the occurrence and reversal of AF within the equine species is statistically higher than that of the rat and human; hence the comparison of human and equine AF and creation of the equine analogue in this project. With the equine model potentially giving insight to future human AF treatments.

The similarity and differences of human, rat and equine physiological heart properties are also displayed in table 1.1.2.1.

Table 1.1.2.1: Table to summarise cardiac properties in a comparison between human, rat and equine system; references 1[Molina, et al, 2012/2015], 2[Edward, 2019], 3[Roy, 2015], 4[Healthy living, 2019], 5[Chadda, et al, 2018], 6[Bui, et al, 2011], 7[Noarton, 2017], 8[Mlyneková et al, 2016], 9[Lyle, et al, 2010], 10[Mader, 2010], 11[Buttner, et al, 2014], 12[Sweet, et al, 1987].

Property	Human	Equine	Rat
Size	0.3Kg [1]	3.5Kg [7]	2g [11]
Average heart rate	60-100bpm [2]	25-40bpm [8]	250 [11]
Approximate max heart rate	(208–(0.7*age)) bpm [3]	240 bpm [8]	495 [11]
Average cardiac output	70ml (0.07L)/beat [3]	1 L/beat [8]	0.85ml/beat [12]
Average blood pressure	120/80mmHg [4]	120/70mmHg [7]	149/107mmHg [12]
% population presenting AF	1-3% [5] 10% over 60 years [5]	2.5% [9]	<90% in medical trials [11]
Approximate death by heart failure	12.5% [6]	56% [10]	3% [11]

1.2 Electrical properties of the Cardiomyocytes

1.2.1 Electrical properties of cells

All cells within the body contain ions; these are atoms that carry an electric charge based upon the loss or gain of an electron. Positively charged ions, or cations, are produced by the loss of an electron; whilst negatively charged ions, or anions, are produced by the gain of an electron.

An electrical cellular property created by the possession of charged ions is voltage (V). This is defined as the potential difference in electromotive force; and in cells this is created by the concentration of each type of charged ion presented on either side of the membrane, and this potential voltage is measured is millivolts (mV).

However, based upon the charge and concentration of ions within cells; continuous movement is induced – firstly to maintain a neutral charge over the cell membrane; and secondly to maintain a neutral ionic concentration gradient over the membrane. This movement is only ceased once the ions equilibrium potential is meet.

The equilibrium or Nernst potential is the principal that drives all passive ionic movements within cells. This occurs as ions strive to establish an equilibrium between their contrasting electrical and concentration gradients. The voltage value at which this balance is achieved is referred to as the equilibrium constant (E_x), and the Nernst equation, as used to calculate E_x is illustrated in figure 1.2.1.1. More so, relative E_x of the major cardiac ions are demonstrated in table 1.2.1.1; these play an important role in the production of both the resting membrane and action potentials.

$$E(ion) = \frac{RT}{zF}\ Ln\ \frac{(ion)o}{(ion)i}$$

Figure 1.2.1.1: Figure to demonstrate the Nernst equation as used to calculate equilibrium constant of an induvial ion, where: E(ion), equilibrium potential; R, gas constant ($8.31JK^{-1}mol^{-1}$); T, temperature (K); z, ion charge; F, faraday constant ($9.65x10^{4}Cmol^{-1}$); $(ion)_o$, extracellular ion concentration; $(ion)_i$, intracellular concentration of ion.

Table 1.2.1.1: Table to illustrate the equilibrium potentials of K^+, Ca^{++} and Na^+ [Lambert et al 2018]; the major cardiac action potential ions.

Ion	Equilibrium potential
K^+	-92mV
Na^+	+70mV
Ca^{2+}	+183mV

However, when considering the action and resting membrane potentials, all of the above ions have to be taken into consideration, based upon the fact that the E_x of each ion is different. Yet, by use of the Goldman Hodgkin Katz (GHK) equation E_x

can be descried for a whole system; considering the E_x of all ion involved and providing an overall voltage potential for the cell. The GHK equation is illustrated in figure 1.2.1.2.

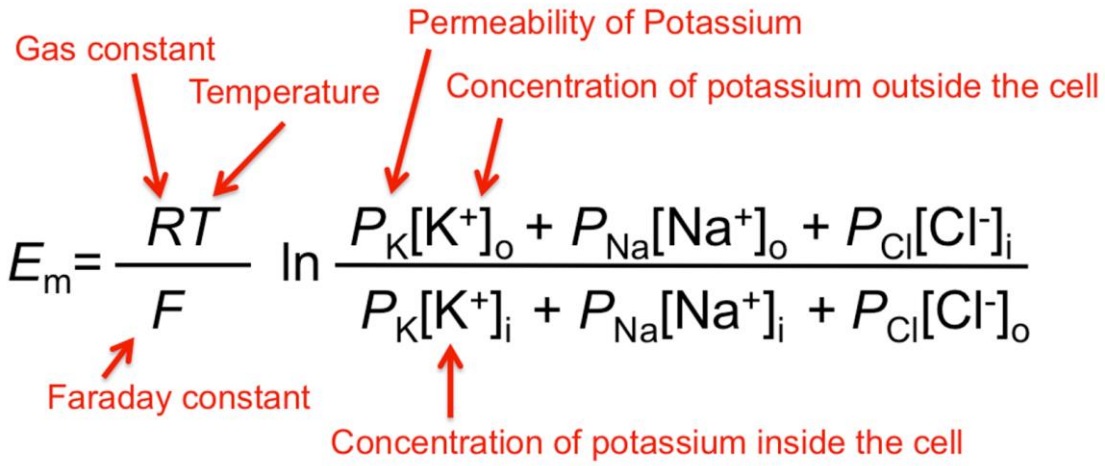

Figure 1.2.1.2: Figure to demonstrate the Goldman Hodgkin Katz equation as used to calculate an overall cellular potential, based upon the electrochemical and concentration gradients of the ions presented within and outside the cell in question; whilst describing each of the equation constituents.

1.2.2 Ionic conformation of Cardiomyocytes

The cardiomyocytes, as with all cell types, have ability to produce or respond to electrical signals. The ionic composition of the cells allows the cardiomyocytes to achieve this electrical activity, as demonstrated in cellular signaling and life cycle processes, aiding cellular communications and control.

The cellular cytosol which holds and supports the cells organelles is bound by the phospholipid bilayer, which additionally allows for a difference in ionic composition of the cell's cytoplasm compared to the extracellular medium. As seen in figure 1.2.2.1, the cytoplasm contains mainly potassium, whereas sodium and chloride ions are dominant concerning the extracellular matrix.

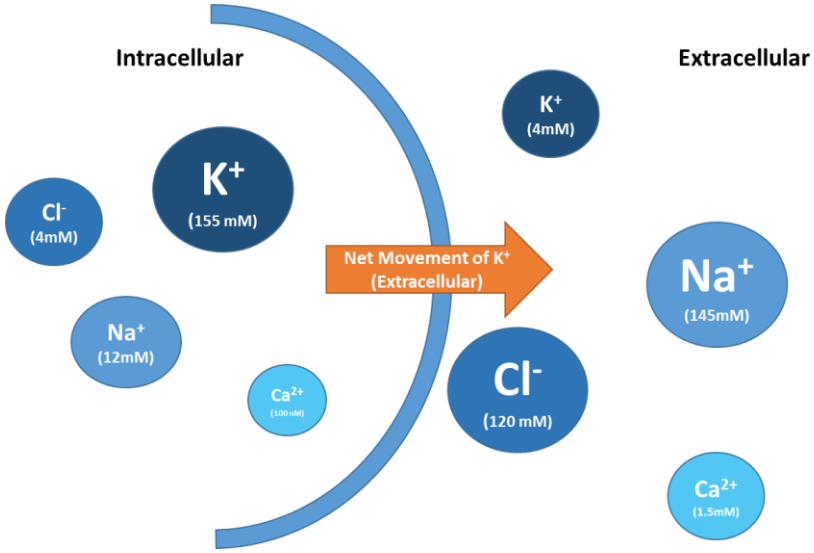

Figure 1.2.2.1: Figure to demonstrate the ionic concentrations in both intracellular and extracellular medium and illustrate the outward net movement of potassium caused by the uneven distribution of electrical charge over the cardiomyocyte membrane, based upon the negative cytoplasm compared to the extracellular space.

This difference in ionic composition induces a distribution of unequal electrical charge over the cell membrane, resulting in a negative cytoplasm compared to the extracellular space. This in turn is responsible for generating the electrical potential that cells possess.

The cell membrane being impermeable to charged ions additionally aids in creating ionic electrochemical gradients between the two sides of the membrane. This labels the cell as 'polar' and induces current though the transmembrane channel proteins that mediate ionic movement. Current occurs via passive flux (simple diffusion) moving ions down an electrochemical gradient; or active processes which requires energy to power ion specific pumps to move ions both with and against the electrochemical gradient, such as the Na^+, K^+-ATPase. An outlined summary of cellular ionic movement is illustrated in figure 1.2.2.2, and it is the movement of these ions that help contribute to the obtained resting membrane potential.

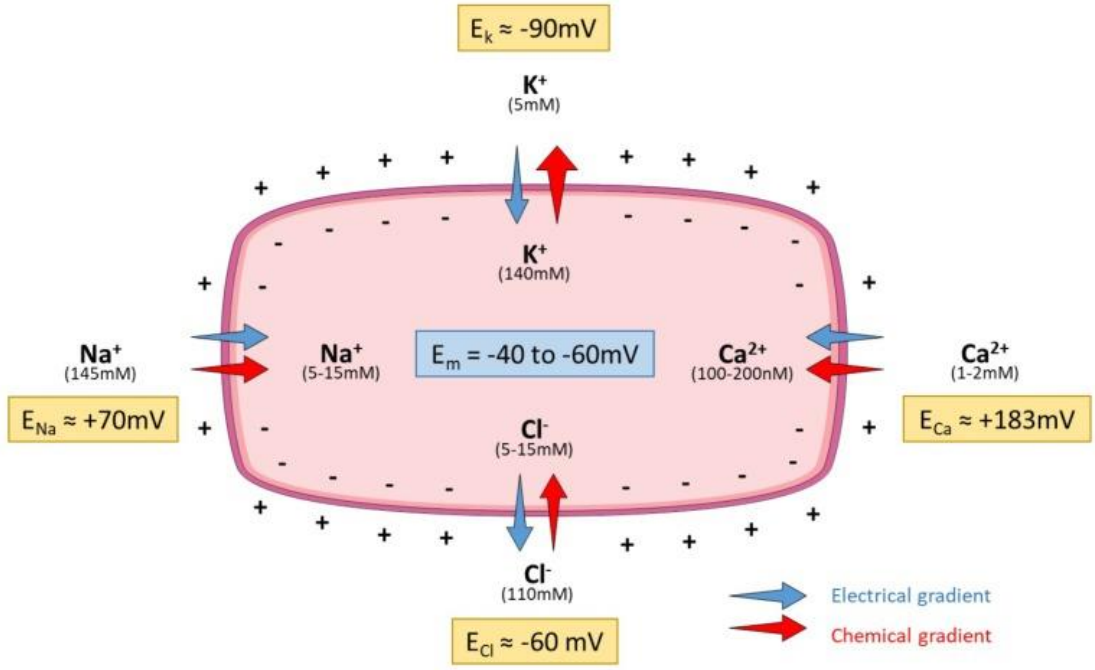

Figure 1.2.2.2: Figure to show the ionic movement of K^+, Ca^{++}, Cl^-, and Na^+ over the cellular membrane based upon the electrical and chemical gradients presented, figure adopted from Lambert et al 2018.

1.2.3 Resting membrane potentials

At rest, the membranes permeability to potassium allows its passive movement producing an increasingly negative resting membrane potential (RMP). This continues until the equilibrium constant of the ion is reached at -90mV [Lambert, *et al*, 2018].

However, despite to the membrane proving impermeable to cations at rest, a weak inward leak of sodium is still presented. To combat this and maintain a negative resting membrane potential; ion migration is facilitated by active transport proteins. The sodium/potassium ATPase pumps are electrogenic channels which build and maintain concentration gradients of sodium and potassium within cells by the unequal exchange of charge. This occurs by substitution of three intracellular sodium ions with two extracellular potassium ions; maintaining resting potentials of -60mV in the cardiac pacemaker cells, and -90mV in the cardiomyocytes [Meyer, *et al,* 2019].

1.2.4 Action potentials

As previously described, Action potentials (AP) that occur in cardiac tissues are consequential of ionic migration over the phospholipid bilayer of the natural pacemaker cells, the cardiomyocytes and the bands of specialist electrical conducting tissues (the bundle of His and Bachmann's bundle) [Choudhury, *et al*, 2015]. These ionic movements are due to ionic equilibrium potentials of Potassium (K^+), Sodium (Na^+) and Calcium (Ca^{2+}). These ionic migrations alter cellular charge - creating AP stimuli that coordinate heart contractions and optimizes blood flow [Bryant, 2014].

The pacemaker actional potential is a spontaneous wave of depolarization that constitutes cardiac conduction and dictates the start of a heartbeat. This is primarily produced by the Sinoatrial node (SAN) in the superior right atrium of the heart and is aided by the high rate of natural depolarization of the SAN. This occurs between 60 and 100 times per minute, with no input from the central nervous system or outside stimuli enabling the organs automaticity; functioning to maintain cyclic activity keeping the hearts rhythm frequent and consistent.

Additionally, and generic to all cardiac tissue, the cardiomyocyte action potential is induced by the transfection of excitement of neighboring myocytes by use of cellular gap junctions which allow Na^{+} and Ca^{++} to move between neighboring cells; rapidly propagating effective AP waves, encouraging functional syncytium and allowing for AP migration across the whole heart.

Different ions activate various phases of the AP and play different roles in AP propagation and progression with sodium and calcium entering the cell and depolarizing the cytosol, before potassium plays a role in repolarization; returning the cell back to its resting state, as aided by the TASK channels, as in section 1.5, which aid in the holding of the resting potential and refractory processes. The phases of the AP can be seen summarized in figure 1.2.4.1, as based on a cardiomyocyte AP.

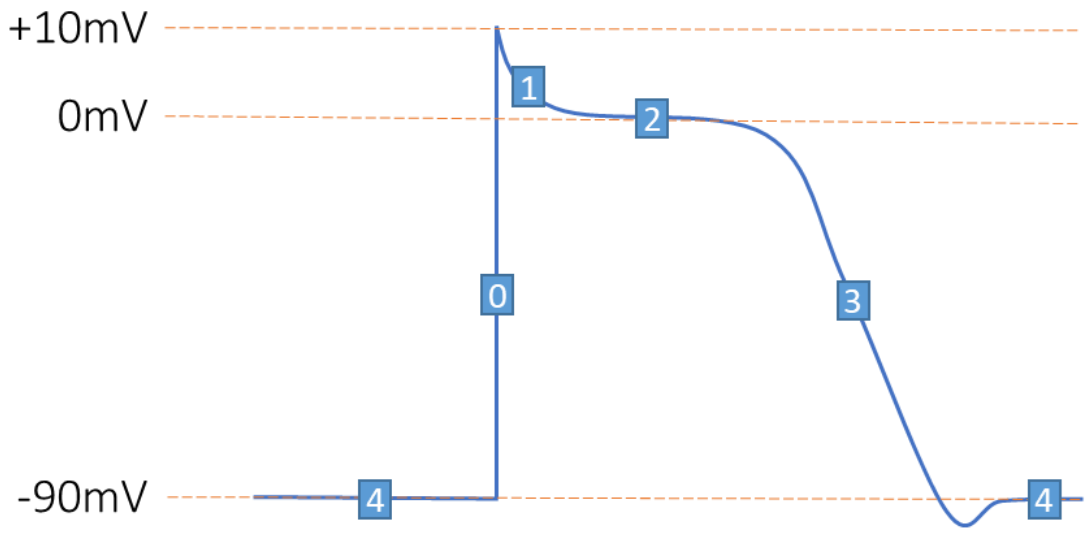

Figure 1.2.4.1: Figure to illustrate the shape and phases of the cardiomyocyte action potential, where phase 4 represents the cell at rest, phase 0 represents the cell during depolarization due to voltage gated Na^{+} channels, phase 1proves partial repolarization as the K^{+} channels open, phase 2 shows the plateau produced the conflicting ion movements as the heart contracts and phase 3 illustrates the repolarization phase of the action potential as driven by K^{+} efflux.

The phases of the action potential prove similar between both pacemaker and cardiomyocyte action potential, however the channels and voltages at which each phase occur can differ. Yet generically, phase 4 of the AP is induced at rest whilst the cell presents its resting membrane potential. Phase 0, involves the depolarization of the cell due to voltage gated Na^{+} channels. Phase 1, proves partial

repolarization as the K^+ channels open; whilst phase 2 proves a plateau produced the conflicting ion movements. Phase 3 illustrates the repolarization phase of the action potential as driven by K^+ efflux, before phase 4 is again obtained.

1.2.4.1 Pacemaker action potentials

The pacemaker action potential, as illustrated in figure 1.2.4.1.1, initiates within the sinoatrial node (SAN) of the right atria. These are a group of expert cells that have adapted - losing their ability to contract but specializing in the initiation of AP stimulus.

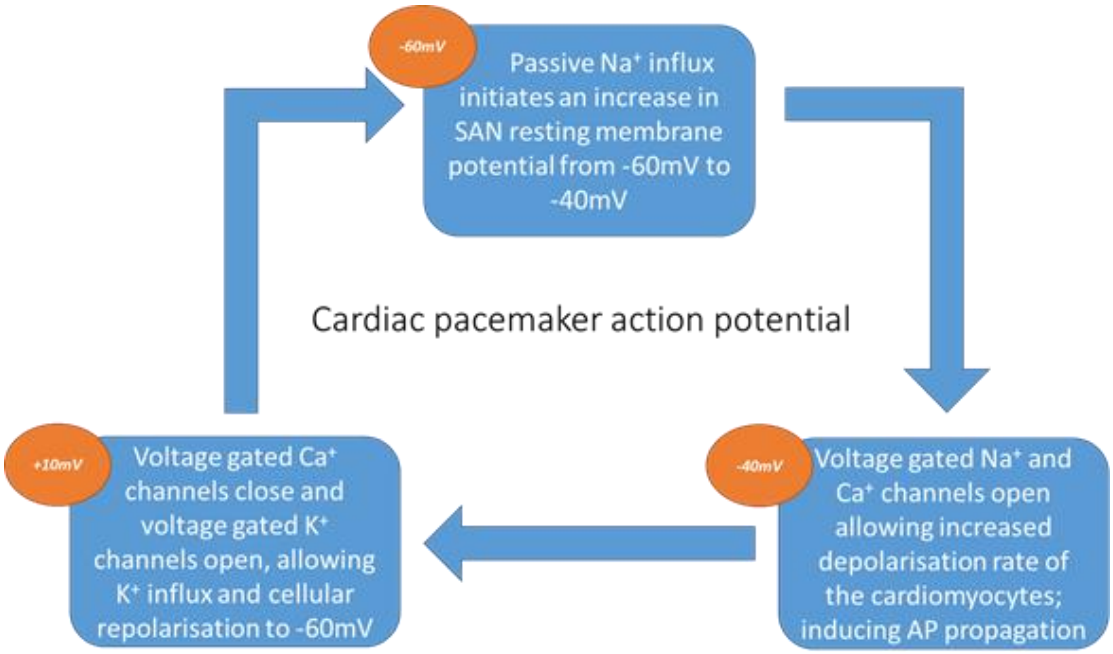

Figure 1.2.4.1.1: Schematic to highlight the various voltages and ion movements within the cardiac pacemaker action potential. Demonstrating depolarization by sodium influx at -60mV and calcium influx at -40mV; and repolarization from potassium influx at +10mV.

AP stimuli begins with the passive action of I_f channel currents, which are only found in the SAN pacemaker cells and a few cells of the Atrioventricular node (AV node) and the Bundle of His. These are voltage gated channels that function at voltages below -40mV and allow passive Na^+ influx, resulting in slow depolarization of the cell. At voltages above -50mV, this effect is endorsed by the action of T-type (transient) voltage gated Ca^{++} channels, allowing Ca^{++} influx contributing to cellular depolarization until a threshold of -40mV is achieved.

At -40mV, I_f channels then close, whilst voltage gated Na^+ channels open along with L-type (long-lasting) voltage gated Ca^{++} channels. Consequently, the cell undergoes further depolarization at an increased rate, until a voltage of +10mV is attained.

At +10mV both voltage gated Na^+ and Ca^{++} channels are inactivated, whilst voltage gated K^+ channels open. K^+ then passively moves back into the myocyte aided by the action of TASK channels, repolarizing the pacemaker cell to their resting voltage of -60mV.

1.2.4.2 Cardiomyocyte action potential

The cardiomyocyte action potential, as described in figure 1.2.4.2.1, is a repercussion of the stimulus produced by the SAN pacemaker cells and pulsates throughout the whole cardiac tissue conducting a heartbeat.

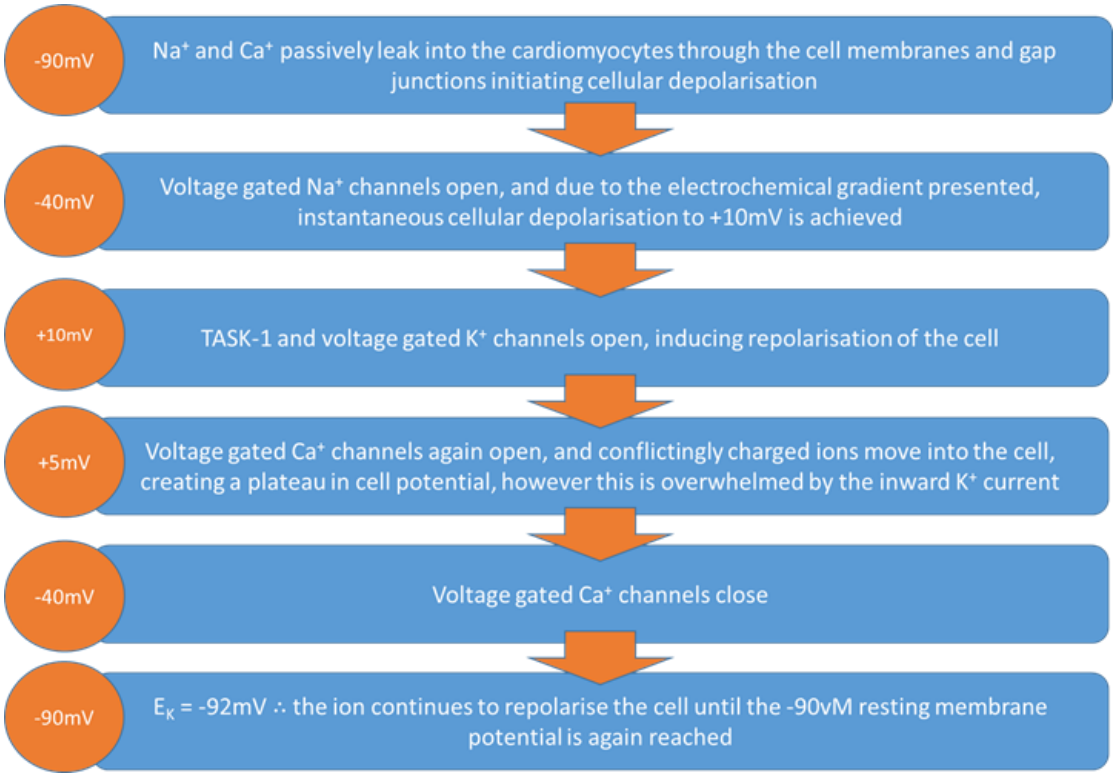

Figure 1.2.4.2.1: Schematic to highlight the voltages and ion movements within the cardiac cardiomyocyte action potential. Including leak and voltage gated sodium and calcium channels that depolarize the cell to +10mv, before leak and voltage gated potassium channels repolarize the cell to -90mV.

Differing to the pacemaker AP, the cardiomyocyte AP begins with a resting membrane potential of -90mV. At this voltage, all voltage gated channels are closed. However slow depolarization of the cardiomyocyte occurs from passive Na^+ and Ca^{++} influx; via intracellular gap junctions. These not only allow for metabolic interchange between cells, but physiologicaly aid intercellular communication [Dhein, 2004]; allowing impulse propagation and migration whilst maintaining normal cardiac rhythm [Rohr, 2004], and encouraging function syncytium [Raun, *et al*, 2009].

Once the gap junctions have induced a cellular depolarization, increasing voltage to meet the -40mV threshold, voltage gated Na^+ are then activated, with their effect endorse by Ca^{++} channels. This induces instantaneous depolarization of the cell to +10mV, based upon the great electrochemical gradient presented over the membrane, as created by Na^+,K^+ pumps.

At +10mV, Na^+ channels close and TASK K^+ channels induce partial repolarization of the cell. However, at +5mV voltage gated K^+ channels open as voltage gated Ca^{++}

channels again activate, this poses the conflicting movement of charged ions, and so creates a plateau in current. Nevertheless, the action of the TASK channels along with the voltage gated channels, overwhelms the action of the Ca^{++} channels; allowing the continued repolarization of the cell. Firstly, the cell repolarizes again to the -50mV threshold where the voltage gated K^+ and Ca^{++} channels deactivate, before repolarization via TASK action continues until the -90mV resting potential is again achieved [Schmidt, *et al,* 2017].

1.2.5 Action potential and cardiac chronotropy

Cardiac chronotropy, or heart rate, is a factor that is solely dictated by the SAN and its rate of neutral spontaneous depolarization, as gives the organ autonomic control. This mean no outside stimulus can conduct a heartbeat; however, heart rate can be influenced by the central nervous system (CNS) and hormone, which can affect the SAN's rate of depolarization [Rodger, *et al*, 2018].

Parasympathetic innervation from the CNS mainly affects the atria and functions with an inhibitory effect. This is induced by the release of neurotransmitters such as Acetylcholine (Ach) which can reduce the intrinsic rate of SAN from 90-120 to 60-100 in humans; and further reduced by protein binding to G-coupled protein receptors (GCPR) that inhibiting the signalling pathway [Enyedi et al, 2010]. The signalling pathway is additionally affected by parasympathetic stimulation increasing the cells permeability to K^+, this hyperpolarises cells and increases the action potential duration (APD) as phase four becomes extended [Rodger, *et al*, 2018].

Controversially, Sympathetic stimulation of the CNS affects the whole heart and functions with agonistic effect. This is encouraged by both the adrenal medulla releasing adrenaline which stimulates cardiac β1 receptors; and increased secretion of noradrenaline at post- ganglionic synapses. This increases the depolarization rate of the SAN by stimulating I_f currents, while further increasing ventricular inotropy (increasing contraction strength) and the cardiac dromotropy. Dromotropy is the speed of neuron conduction, as increased by shorter APD, as created when rectifying K^+ channels are opened [Rodger, *et al*, 2018].

1.2.6 Cardiac conduction systems

As discussed in section 1.2.4, AP initiated in the SAN migrates to the local area via cardiomyocyte gap junctions. However, for the stimulus to travel throughout the whole cardiac tissue and coordinate a viable sequence of muscular contractions, the heart employs an electrical conduction system, as illustrated in figure 1.2.6.1. This allows for the depolarization of all cardiomyocytes, and provides regulatory control of the impulse migration, ensuring that contraction of all four heart chambers are synchronized and cardiac function optimized.

To begin, SAN stimulus depolarizes the atria at a rate of $1ms^{-1}$, yet this is aided by Bachmann's bundle. Bachmann's bundle consists of three internodal tracks that join the SAN and Atrioventricular node (AV node). These tracks carry the impulses from the right to left atria and allow the stimulus to be well distributed throughout the whole of both atria, coordinating their contraction [Choudhury, *et al,* 2015].

Further, once conductance down Bachmann's bundle has reached the AV node a small delay is induced. The AV node is the only normal non-fibrous site of connection between the atria and ventricles and has proven to be of high vagal tone which reduces K^+ permeability and increases the refectory period to 250ms (relative refractory period: 50ms). This allows a 0.1 second delay before stimulating the ventricles allowing full atrial contraction [Bonagura, 2004]. This ensures that the atrial blood load has been ejected into the ventricles and the atrioventricular values have closed, before the ventricles begin to contract. This prevents the atria and ventricles contracting against each other, heart murmurs and arrhythmia [Raun, *et al,* 2009].

Proceeding the 0.1sec delay, the AP stimulus is conducted down the bundle of His which runs down the septum of the heart to the ventricles [Patteson, 1996]. Approximately 25% of the way down the septum, the bundle of His splits into two; a right bundle then continues down the septum before climbing the right ventricle myocardium, while a left bundle continues half way down the septum before again splitting into the posterior and anterior fascicles [Patteson, 1996].

Multiple divisions of the three neurons creates the Purkinje fibers that penetrate the ventricular tissue aiding in the fast spread of depolarization at a rate of 1-4ms-1, with the posterior and anterior fascicles increasing depolarization in the larger left ventricle [Patteson, 1996].

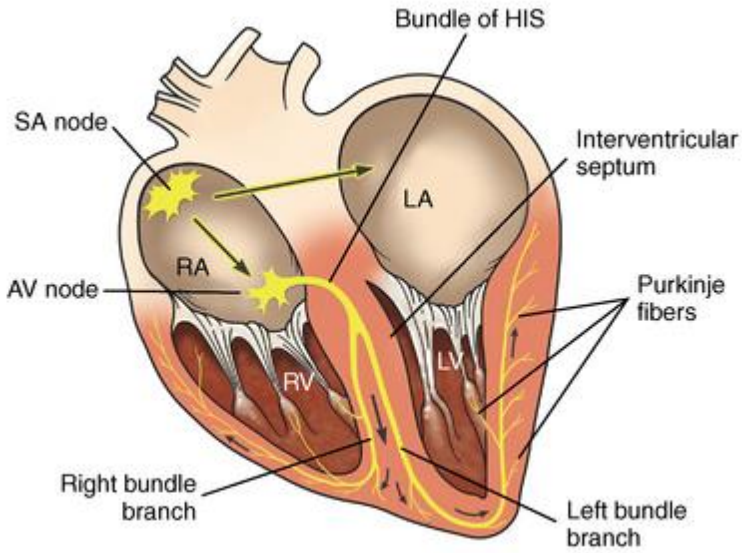

Figure 1.2.6.1: Figure to illustrate the cardiac conduction system in the mammalian heart, demonstrating the SA node that initiates the action potential stimulus; the internodal tacks that carry the stimuli across the atria; the AV node which induces a delay to coordinate the four chambers, and the bundle of His and Purkinje fibers which carry the action potential around the ventricles.

1.2.7 Electrocardiogram (ECG)

As many cells simultaneously re/depolarize during the process of AP production as described in sections 1.2.4; an external electric field is created which can be

measured from the bodies surface [Verheyen, *et al,* 2010]. By recording this electrical activity, it is then possible to map the wave of depolarization throughout the cardiac tissue, producing an electrocardiogram (ECG). In turn, ECG can then identify arrhythmias and abnormal heart function by study of the whole heart's electrical activity over time, as opposed to AP which studies the electrical activity of singular cells. This deems the ECG as a respectable diagnostic tool and is commonly used to evaluate drugs actions and effects [Brown, *et al,* 1988].

As demonstrated in a human model, figure 1.2.7.1, and an equine model, figure 1.2.7.2, the ECG consists of P, Q, R, S and T complexes (waves), which correlate to different parts of the fixed electrical conduction system as described in section 1.2.6.

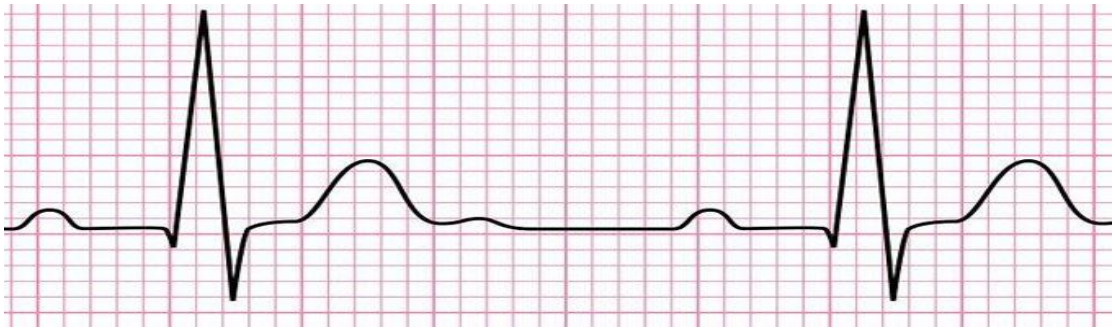

Figure 1.2.7.1: Figure to demonstrate the healthy, expected ECG of a human patient in sinus rhythm [Gaurab, 2018], illustrating distinct and clear P, QRS, and T waves/complex as the wave of depolarization encounters each part of the electrical conduction pathway.

Figure 1.2.7.2: Figure to demonstrate the healthy, expected ECG of an equine patient in sinus rhythm [Verheyen, et al, 2010], illustrating distinct and clear P, RSR', and T waves/complex as the wave of depolarization encounters each part of the electrical conduction pathway, and further demonstrating the effect of the larger organ size on the electrical traces obtained.

The ECG begins with production of the P wave. This is produced as the atria depolarize, and in humans is usually presented with single positive morphology [Patteson, 1996]. In equine however, the P wave can be presented in bifid nature, as a peak is produced on depolarization of the right atria, and a second upon depolarization of the left [Patteson, 1996]. More so, the equine P wave can be presented with biphasic morphology with both a positive and negative deflection representing depolarization of different atria. Yet overall, the equine P wave varies in morphology, even within the same animal upon study of successive beats [Bonagura, 2004].

Next presented on the ECG is the PR interval. This is a flat segment that lasts approximately 0.5seconds within a normal equine and is caused by the delayed electrical signal induced by the increased vagal tone of the AV node [Bonagura, 2004].

Following this comes the QRS complex. This is created as the bundle of His and Perkinje fibers are stimulated and fast depolarization of the ventricular myocardium occurs. Within humans this is demonstrated as a large deflection with the Q wave defined as the first negative deflection; the R wave the first positive deflection; and the S wave the first negative deflection following the R wave [Bonagura, 2004].

However, in equines this QRS complex is presented with a different morphology to other species [Tilley, 1992]. With Q, R, and S waves correlating the same function, but subsequent positive deflections are then labeled as R' waves; and negative deflections S' waves. So, as seen in figure 1.2.7.3, the equine QRS complex typically presents RSR' morphology [Bonagura, 2004].

Preceding this, the T wave represents ventricular repolarization, yet again, equines can present this wave with great variability even within the same animal on consecutive beats [Bonagura, 2004].

Concerning diagnostics, the ECG is a tool that can identify faults within individual parts of the electrical conduction system. Though, the large Perkinje fiber system, presented in the equine heart deems the RSR' complex of limited information concerning ectopic ventricular beats [Verheyen, *et al,* 2010]. Yet the ECG is still of use regarding heart rate and rhythm; and arrhythmia or fibrillation, as recognized by the abnormal presence or absence of waves.

ECG of a normal equine sinus rhythm can be identified in figure 1.2.7.3, whilst figure 1.2.7.4 presents an ECG of multiple bifid P waves, and increased distance between RSR' complexes – diagnosing atrial fibrillation (AF), as induced by pathophysiological action of TASK-1 channels.

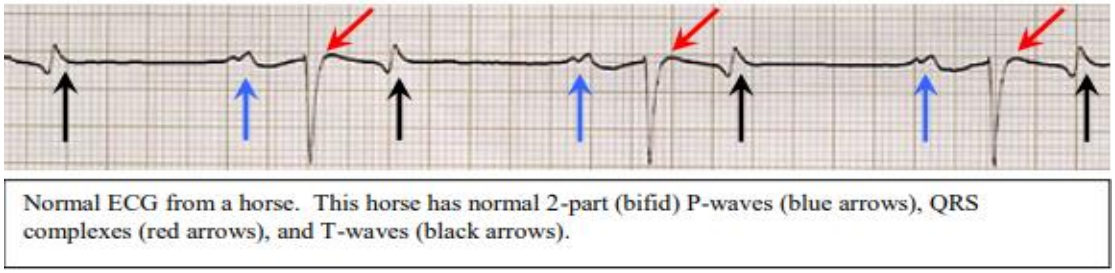

Normal ECG from a horse. This horse has normal 2-part (bifid) P-waves (blue arrows), QRS complexes (red arrows), and T-waves (black arrows).

Figure 1.2.7.3: Figure to illustrate the sinus rhythm of an equine, demonstrating bifid P waves, QRS complexes and T waves [Durham, 2008].

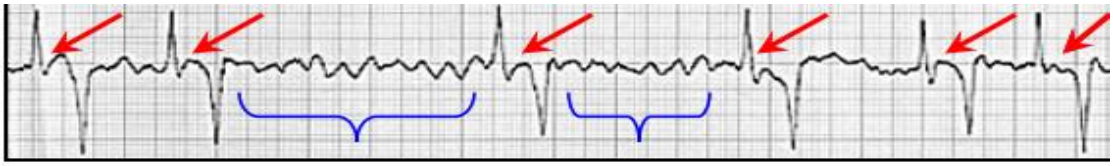

ECG of a horse in atrial fibrillation. Note random distribution of QRS complexes (red arrows) with no associated P-waves and the presence of an undulating baseline ('f-waves', blue brackets)

Figure 1.2.7.4: Figure to illustrate the ECG of an equine experiencing AF – as induced by TASK-1 dysfunction [Durham, 2008].

1.3 Human and Equine Atrial Fibrillation (AF)

Atrial fibrillation (AF) is the most common cardiac arrhythmia, affecting 1–2% of the general population [Olesen, *et al,* 2014] and over two million Americans [Harleton, *et al,* 2015]; incurring an estimated U.S. treatment cost of $6.65 billion yearly [Roberts, *et al,* 2014]. This figure is additionally set to triple by 2050, as the condition predominantly affects elder patients, proposing greater numbers of sufferers as the expanding population ages [Harleton, *et al,* 2015]. Moreover, concerning the horse, cardiac arrhythmias are more common than in any other domestic animal species [McGuirk, *et al,*1985]; with AF being the greatest performance-limiting arrhythmia, as concluded by a study of 2,500 horses where the condition was presented in 2.5% of subjects [McGurrin, *et al,* 2015].

AF is a chronic condition associated with structural, electrical and metabolic changes within the heart [Lazzerinin, *et al,* 2018/ Harleton, *et al,* 2015]. These changes can cause disturbances in impulse formation or conduction and are related to atrial remodeling caused by variation in gene expression, signaling pathways and ion channel activity and function [Harleton, *et al,* 2015/ Olesen, *et al,* 2014]. Leading to a disorganization of atrial impulses and electrical coordination as seen in figure 1.3.1.

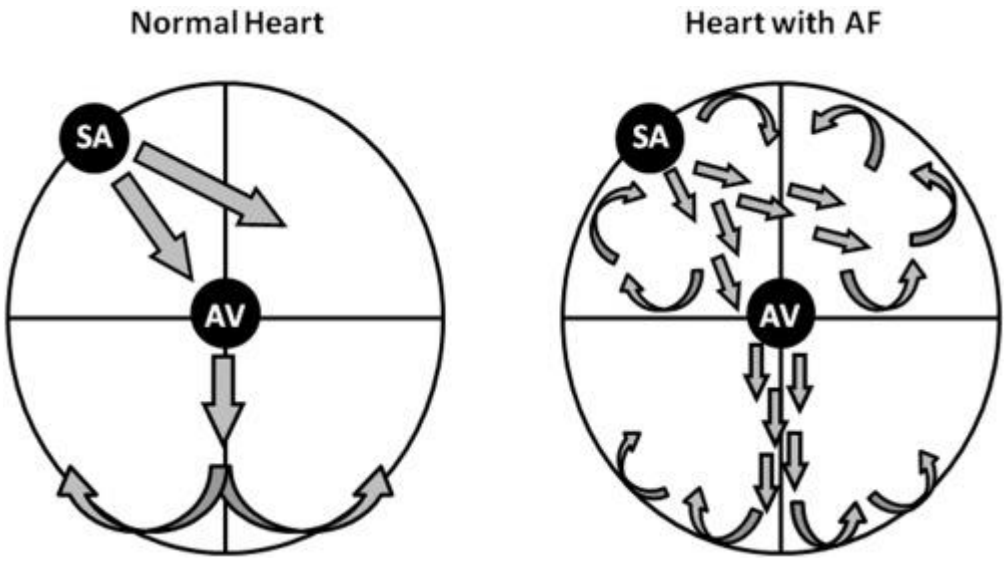

Figure 1.3.1: Schematic to suggest normal heart function (left), and the loss of atrial coordination, wave direction creating meandering waves and less ventricular stimulus as seen in AF patients (right) [Campuzano, et al, 2016].

Hypertensive and structural heart disease are repercussive of AF [Olesen, *et al,* 2014], along with an amplified risk of thrombotic occurrences and stroke, essentially increasing mortality rates [Harleton, *et al,* 2015]. Equine exercise intolerance is also frequently linked to AF and similarly to humans, equine AF presents auscultation abnormalities, fast or slow heart rate, irregular rhythm, irregular beats, extra sounds, long pauses, and abnormal heart sounds [McGuirk, *et al,*1985].

Definitive diagnosis of AF is concluded by use of an electrocardiogram (ECG), as first documented in the horse 1911 [McGurrin, *et al,* 2015]. However further cardiac tests are usually required to determine disease etiology and evaluate its severity [McGuirk, *et al,*1985].

When ECG identify clinical AF signs, or if hemodynamic parameters are affected by arrhythmia; antiarrhythmic therapies are given [McGuirk, *et al,*1985]. Yet, despite AF being a common occurrence and provoking significant welfare and finance issues [Harleton, *et al,* 2015], effective therapies are limited based upon the diverse causes of the condition. Additionally, deeming existing treatments only part adequate [Gierten, et al, 2010/Harleton, *et al,* 2015].

Most current therapies function by blocking K^+ channels in order to slow down atrial repolarization and extend the effective refractory period [Gierten, et al, 2010]. However due to a lack of specific ion targeting drugs, most treatments also prolong the ventricular action potential, increasing risk of sudden cardiac death and torsades de pointes arrhythmia, as characterized by long QT intervals due to ventricular fibrillation (VF) [Gierten, et al, 2010]. Historically, equine treatment has mostly consisted of Quinidine salts, however their use is vigilant due to toxic side effects [McGuirk, *et al,*1985]. Additionally, Digoxin is most commonly used concerning ventricular arrhythmias and heart rate increasing arrhythmias; however, dysrhythmia due to vagal tone are considered normal within equine hearts, and so no further therapies are available, equaling a poor prognosis if AF is induced by a underlying heart condition [McGuirk, *et al,*1985].

Considering the pathogenesis of AF in heavily endorsed by genetic factors [Liang, *et al,* 2014], and the absence of reliably effective treatments [Harleton, *et al,* 2015]. A deeper understanding of the genetic basis of AF would provide massive potential to aid in patient care. Allowing identification of individuals at higher risk; gaining a better understanding of pathophysiological mechanisms; and allowing a greater insight to possible future treatments [Lubitz, *et al,* 2010].

1.4 Potassium ion channels

The cellular movement of potassium ions plays a functional role in the regulation of neuron excitability and maintenance of resting membrane potentials, and the selective movement of potassium ion is conducted by three main types of ion channel. These channels all contain hydrophobic hairpin loops, which function as pore forming α-subunits; yet differ in the number and amino acid sequences of pore forming loops. However, despite the difference presented within the loop sequences, all channels continue to demonstrate a functional selectivity filter; allowing individual potassium ions to be rapidly selected and transported [Mathie and Veale, 2009].

The voltage gated potassium (K_V) channels, are formed from 6 transmembrane domains and provide one pore-forming loop. These channels are sensitive to voltage changes within the cell membrane; which induces conformation change to allow potassium efflux. This is utilized within the action potential to return depolarized cells back to resting membrane potential.

Similarly, the inward rectifying potassium (K_{ir}) channels reveal one pore-forming loop, but contain only 2 transmembrane domains. These channels are open across membrane voltages, however function to favor the influx of potassium, moving extracellular potassium into the cell's cytosol.

Further, the two pore domain potassium (K_{2P}) channels are additionally open across all voltages, however these support potassium efflux by production of leak currents; which prove pivotal in the neuron excitability and resting membrane determination [Mathie and Veale, 2009].

1.5 Two pore domain potassium ion channels (K_{2P})

The two pore potassium ion channels (K_{2P}) are a unique family of proteins that function to produce selective potassium pores, creating extracellular background leak of potassium without any voltage dependence [Enyedi et al, 2010]. K_{2P} potassium leak can be predicted by GHK equation and is controlled by electrodiffusion law, contributing to the maintenance of a baseline electrical potentials. This allows cells to produce action potentials and recover to a resting membrane state, at a voltage below the action potential threshold [Zúñiga, 2016]. Within neurons, this property then enables K_{2P} current to dictate both APD and resting membrane voltage.

Currently, 15 K_{2P} channels are known to function in humans, and based upon their primary structure, are subdivided into 6 families, as found in table 1.5.1 [Zúñiga, 2016]. The K_{2P} families however, present low sequence similarities, and prove the equal the variation seen between potassium channel types. Yet, all K_{2P} channels meet the classification criteria, and prove α-subunit (monomer) structure of 4 transmembrane domains and 2 pore forming domains, providing all K_{2P}'s with the same membrane spanning topology, producing functional K^+ channels in dimer formation.

Further, despite K_{2P} channels permitting constant K^+ leak due to their voltage independence - inducing a high open probability (PO). Each family of channel has its own gating mechanism stimuli, consequentially increasing PO (allowing greater current) but still the family presents no activation, deactivation, or inactivation kinetics [Enyedi et al, 2010]. These stimuli are additionally listed in table 1.5.1.

Table 1.5.1: Table to show the K_{2P} subfamily members in relation to their gene and corresponding loci, in addition to the channels range of gating mechanisms.

K2P Sub-family	Protein	Gene	Gene loci (Uniprot)	Gating mechanism	Reference
TWIK (Tandem of pore domains in a weak inward rectifying K^+ channel)	TWIK-1	KCNK1	1q42.2	Weak inward rectifiers	(Enyedi et al, 2010) / (Niemyre et al, 2016)
	TWIK-2	KCNK6	19q13.2		
		KCNK7	11q13.1		
TASK (TWIK-related acid-sensitive K^+ channel)	TASK-1	KCNK3	2p23.3	Acidification-inhibited	
	TASK-3	KCNK9	8q24.3		
	TASK-5	KCNK15	20q13.12		
TREK (TWIK-related K^+ channel)	TRAAK	KCNK4	11q13.1	Arachidonic acid activated	
	TREK-1	KCNK2	1q41	Lipid and mechanosensitive	
	TREK-2	KCNK10	14q31.3		
TALK (TWIK related alkaline pH-activated K^+ channel)	TALK-1	KCNK16	6p21.2	Alkalinization activated	
	TALK-2	KCNK17	6p21.2		
	TASK-2	KCNK5	6p21.2		
THIK (Tandem pore domain halothane-inhibited K^+ channel)	THIK-1	KCNK13	14q32.11	Inhibited by halothane	
	THIK-2	KCNK12	2p16.3		
TRESK (TWIK related spinal cord K^+ channel)	TRESK	KCNK18	10q25.3	Spinal cord channels	

1.5.1 K_2P structure

Structurally, basic K_{2P} protein structure includes an amino terminus (N-terminus), 4 transmembrane alpha helixes (TM1-4), 2 pore forming loop regions (P), and a carboxylic acid (COOH) terminus (C-terminus). These α-subunits are assembled in sequence M1-P-M2-M3-P-M4; with both N- and C- termini facing the cytosol [Zúñiga, 2016], as illustrated in figure 1.5.1.1. However, functional ion channels only exist in quaternary structure, with the unique molecular topology of K2P channels allowing two α-subunits to dimerize and produce a functional K^+ selectivity filter and ion conduction pore [Arakel, *et al,* 2014/ Enyedi et al, 2010].

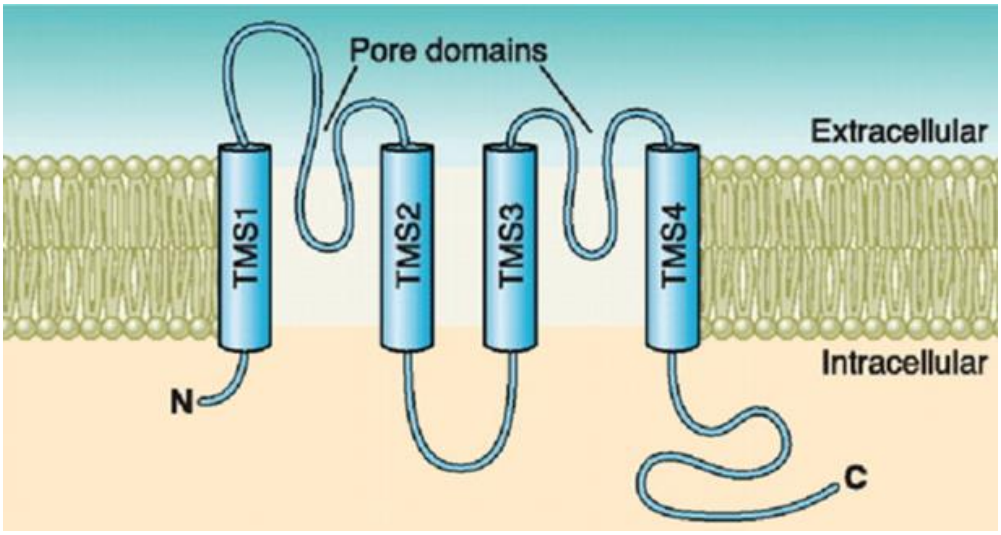

Figure 1.5.1.1: Cartoon description of the typical K2P α-subunit morphology; displaying 4 transmembrane domains; two pore forming loops and a cytosolic N and C terminus.

Dimer conformation achieves each monomer providing 2 P-loop regions with the TM2 and TM4 forming the walls lining the water filled inner conduction pore, resulting in the formation of a pseudoletrameric selectivity filter [Streit, *et al,* 2011], as demonstrated in figures 1.5.1.2 and 1.5.1.3.

This dimerization is mediated by an amphipathic α-helix that is positioned on the M1P1 loop between the first transmembrane domain (TM1) and the first pore loop (P1). This α-helicase encourages subunit interactions and dimerization; whilst presenting a Cystine at position 69 (C69), which further permits the formation of inter-chain disulfide bridges with another other α-subunit; producing a stable, covalent dimer [Zúñiga, 2016].

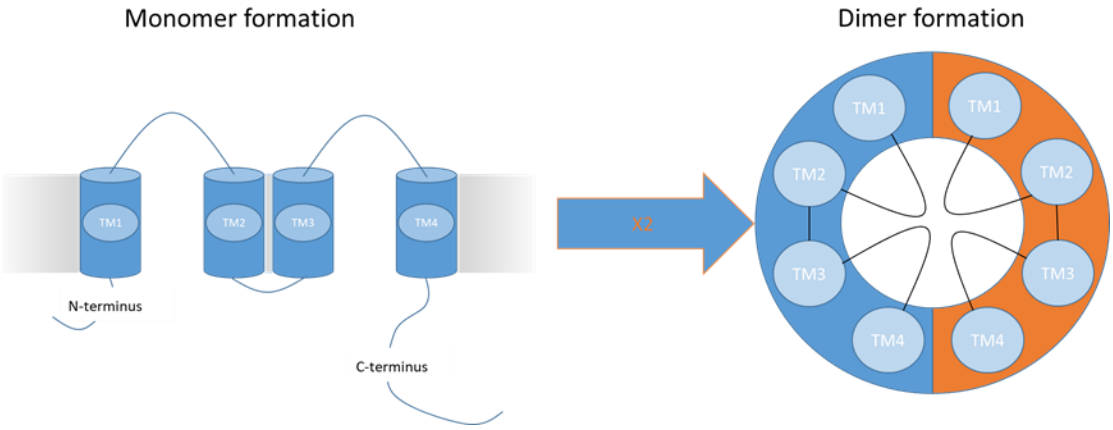

Figure 1.5.1.2: Schematic to imitate a K_2P monomer (left), and display an approximation of the pore formation from a top view (right) - based upon the two subunit interactions and interchain disulfide bridge formation that induces covalent dimer formation.

Additionally, interaction of the M1P1 loops, aids in the production of the K_{2P} cap structure, as illustrated in figure 1.5.1.3. These are created by the M1P1 loops interacting, and produce 'side like' portals for individual ions to enter the transmembrane pathway [Zúñiga, 2016]. However, little is known about this, and cap structures can differ between protein models, depending if the outer helix of one α-subunit is interacting with the inner helix of the same or opposite monomer [Zúñiga, 2016].

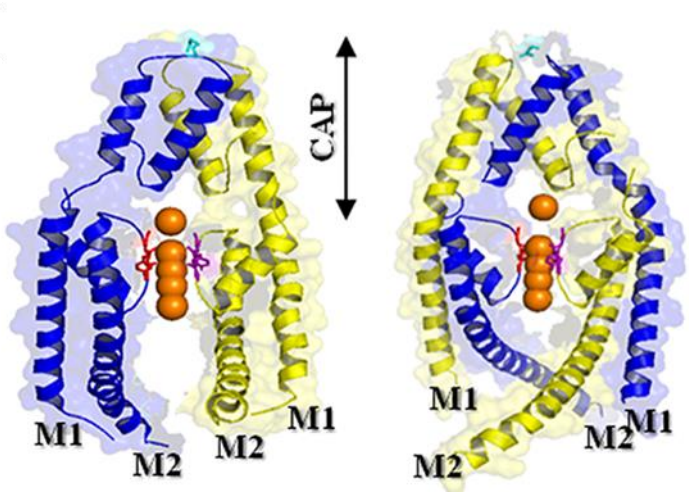

Figure 1.5.1.3: Figure to represent the structure of a K_{2P} dimer, displaying a functional pore and selectivity filter, in addition to the extracellular cap as produced from interaction of the helixes (Adopted from Zúñiga, 2016).

1.5.2 K_{2P} selectivity filter

Successful dimerization of two K_{2P} α-subunits, results in the production of a water filled inner conduction pore and the formation of a pseudoletrameric selectivity filter as demonstrated in figure 1.5.1.3 and schematically shown in figure 1.5.2.1 [Streit, *et al,* 2011].

This conduction pore is lined by the TM2 and TM4 segments of each α-subunit, resulting in 4 identical subunits that encircle the potassium ion pathway. Additionally, the carbonyl oxygens of the amino acids presented within the signature sequence of these subunits, then created a dehydration gate. The signature sequence consists of amino acids, Thr-Val-Gly-X-Gly, and further is responsible for the creation of the channel's selectivity filter [Doyle*, et al*, 1998].

The selectivity filter functions by the channels diameter and carbonyl oxygen positioning providing a channel of optimum width to interact with potassium ions (atom radius 1.33 angstrom, Å), whilst sodium atoms prove too small (0.95Å) to interact and pass through. Additionally, the signature sequence provides 5 sites that receive potassium alternately, with the ionic repulsion from the proceeding ion driving the movement through the channel [Doyle*, et al*, 1998].

The process of potassium efflux then commences with intracellular cationic potassium being solvated within a hydration sphere surrounded by water molecules which stabilize the ion. The cation is then attracted to the negative regions of the helix structures presented by the TM domains, and moves toward the channel mouth. Here, there is no thermodynamic expense created as the ion becomes dehydrated by exchanging electrostatic bonds with the water molecules for electrostatic bonds with the carbonyl oxygens. This proves an easy process, as the bond lengths created are the same as those terminated, and the distance of the D shells from the potassium's nucleus, makes bond breaking easy. The potassium then becomes chelated within the pore as the carbonyl group stabilize the ion,

however, attraction of further potassium ions pushes the ion though the 5 acceptance sites and out of the channel, into the extracellular space, where it again hydrates [Catalyst University, 2016].

Ion size therefore aids the selectivity filter, as the geometric attraction of water molecules to the potassium, matches that of the carbonyl oxygens within the pore. However, sodium ions are smaller so do not present this geometric match, and further due to the smaller radius, it is proven thermodynamically unfavorable to replace the attractions to water with those with the carbonyl groups. Concluding that sodium cannot pass through the pore [Catalyst University, 2016/Doyle*, et al*, 1998].

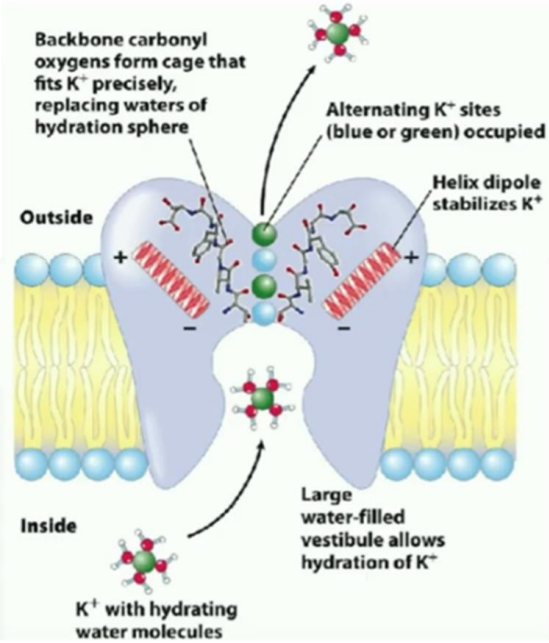

Figure 1.5.2.1: Schematic representation of the selectivity filter and pore formation in K_{2P} channels, with explanation of how K_+ moves through the channel based on electrostatic attraction to carbonyl oxygens, only possible due to atomic size; as adopted from Catalyst University, 2016.

1.5.3 TWIK-related acid-sensitive K^+ channel 1 (TASK-1 ($K_{2P}3.1$))

The TWIK-related acid sensitive K^+ channel 1 (TASK-1 or $K_{2P}3.1$), as seen in figure 1.5.3.1, is a pH gated member of the K_{2P} super family [Enyedi et al, 2010], and proves a 43,518 Da protein, of 394 amino acids, as encoded by the KCNK3 gene of chromosome 2.

Figure 1.5.3.1: Model to demonstrate the TASK-1 protein dimer morphology from a side view, as constructed by Swiss model, illustrating the 4 transmembrane domains of each monomer and the pore, selectivity filter and gate formation in the central region - as induced by interaction of the transmembrane domains.

The current carried by the $K_{2P}3.1$ channels present electrophysiological traits considered characteristic of potassium selective leak currents - exhibiting a voltage independent gateway and proving Goldman-Hodgkin-Katz (outward) rectification [Lesage, *et al,* 2000/ Schmidt, *et al,* 2014b]. However, TASK-1 function can be strongly inhibited by pH along with other environmental factors such as hypoxia, extracellular pH, inhalational anesthetics, G-coupled proteins and signaling molecules such as, phospholipase C, protein kinase C and protein kinase A [Enyedi et al, 2010, Harleton, *et al,* 2015/Bohnen, *et al,* 2017].

Whilst intracellular pH change poses no effect on channel activity [Enyedi et al, 2010], TASK-1 proves extremely sensitive to extracellular pH within the physiological range [Enyedi et al, 2010/Harleton, *et al,* 2015/Hajdú, *et al,* 2003/Bohnen, *et al,* 2017], and can be inhibited by extracellular acidification with a pK value of 7.3 and a Hill coefficient of 1.6 [Enyedi et al, 2010]. This extreme pH sensitivity is repercussive of protonation of a Histidine at position 98 (H98) at acid external pH, whilst H72 and K210 also aid this effect [Lesage, *et al,* 2000], as shown in figure #, which highlights important regions within the TASK-1 amino acid sequence. However, it is stated that TASK-1 pH sensitivity can be reduced in the presence of a high external potassium concentration [Enyedi et al, 2010].

MKRQNVRTLALIVCTFTYLLVGAAVFDALESEPELIERQRLELRQQELRA
RYNLSQGGYEELERVVLRLKP**H**KAGVQWRFAGSFYFAITVIT**T**I**GYGH**AA
PSTDGGKVFCMFYALLG**I**PLT**L**VMFQSLGERINTLVRYLLHRAKKGLGMR
RADVSMANMVLIGFFSCISTLCIGAAAFSHYEHWTFFQAYYYCFITLT**T**I
GFGDYVALQ**K**DQALQTQPQYVAFSFVYILTGLTV**I**GAF**L**NLV**VLRFMT**MN
AEDEKRDAEHRALLTRNGQAGGGGGGGSAHTTDTASSTAAAGGGGFRNVY
AEVLHFQSMCSCLWYKSREKLQYSIPMIIPRDLSTSDTCVEQSHSSPGGG
GRYSDTPSRRCLCSGAPRSAISSVSTGLHSLS*T*FRGLM**KRRSSV**

Highlight	Region	Amino acids
	Cytoplasmic topological domain (N-terminus)	1-8
	Helical transmabrane section (TM1)	9-29
	Intermembrane pore forming region (P1)	78-101
	Helical transmabrane section (TM2)	108-128
	Cytoplasmic topological domain	129-158
	Helical transmabrane section (TM3)	159-179
	Intermembrane pore forming region (P2)	184-207
	Helical transmabrane section (TM4)	223-243
	Cytoplasmic topological domain (C-terminus)	244-394

Binding Region	Amino acid(S)	Description
KSSRRV	289-394	2 Protein kinase A (PKA) binding sites (+ Proposed P11 and 14-3-3 binding)
L122	122	Cavity facing aliphatic Leucine residue contributing drug binding (TM2)
L239	239	Cavity facing aliphatic Leucine residue contributing drug binding (TM4)
I118	118	Cavity facing lipophilic Isoleucine contributing drug binding (TM2)
I235	235	Cavity facing Lipophilic Isoleucine contributing drug binding (TM4)
VLRFMT	243-248	Halothane response element (HRE)
H72	72	Histidine acid sensing residue
K210	210	Lysine acid sensing residue
GYGH	104-107	Pore 1 selectivity motif
GFGD	210-213	Pore 2 selectivity motif
H98	98	Primary Histidine acid sensing residue (By protonation)
T93	93	Threonine contributing drug binding (P1)
T199	199	Threonine contributing drug binding (P2)

Figure 1.5.3.2: Figure to display: top, the 394 amino acid sequence of TASK-1, with highlighted sequences relating to the transmembrane and pore regions as described in the table positioned bottom left; bottom left, key for highlighted region of the TASK-1 amino acid sequence with brief description of domains and its amino acid numbers; bottom right, table of amino acids highlighted as important concerning the function of TASK-1.

This verifies pH as an essential factor concerning $K_{2P}3.1$ current, and considering TASK-1 function, enables changes in extracellular environment to affect K^+ flux and APD [Gierten, *et al*, 2010].

TASK-1 is a key regulator of many physiological processes within cells of the cardiovascular system [Streit, *et al,* 2011], and within the human heart, is expressed in the para-nodal region and AV node [Liang, *et al,* 2014], but predominant expression occurs within the atria, as presented in figure 1.5.3.3 [Gierten, et al, 2010/ Liang, *et al,* 2014]. Here, $K_{2P}3.1$ function is proven to contribute to 15 % current within the right auricular cardiomyocytes [Wiedmann et al, 2018], and 40% of the resting potential current in atrial myocytes, where it is open across all voltages. This deems TASK-1 active in all repolarizing stages of the cardiac action potential. This is repercussive of constant potassium efflux, reversing the depolarization created by the influx of Na^+ and Ca^{++} ions; returning to the atrial cardiomyocytes to their -90mV resting membrane potential [Gierten, et al, 2010/Harleton, *et al,* 2015/Arakel, *et al,* 2014]. This defines the channels ability to promote the plateau current of the cardiac AP; thus, inducing ability to both prolong and suppress the cardiac APD and consequently, the duration of myocardial contraction; encourage electrical dysrhythmia and AF [Goldstein, *et al,* 2001/Gierten, et al, 2010/Bohnen, *et al,* 2017]. Hence initiating an expanding body of research proving the channels importance in the cardiovascular electrical system, and highlighting TASK-1 as a suitable and specific drug target in antiarrhythmic therapy [Wiedmann et al, 2018].

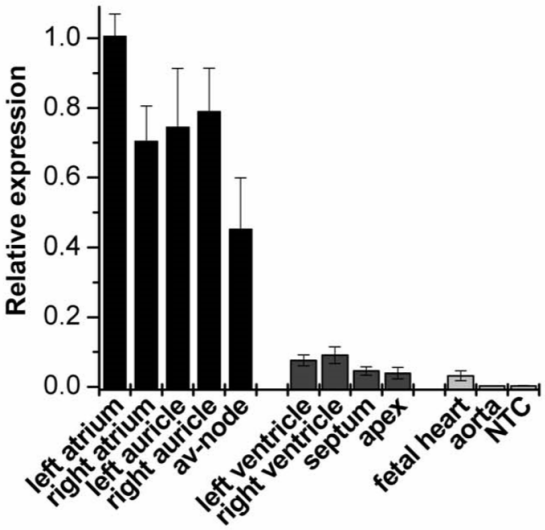

Figure 1.5.3.3: Figure to show the expression levels of TASK-1 concerning different regions of the heart; providing the channels predominant expression in the atria [Gierten, et al, 2010].

However, the unique molecular topology of K_{2P} channels allows KCNK3 to dimerize forming either as a homomeric concatemer (homodimer) by the association of two TASK-1 monomers; or as a heterodimeric concatemer (heterodimer) by binding of a TASK-1 monomer with another K_{2P} analogue of the same family; usually TASK-3 [Cunningham, *et al,* 2018/Bohnen, *et al,* 2017].

1.5.4 TWIK-related acid-sensitive K^+ channel 3 (TASK-3 ($K_{2P}9.1$))

The TWIK-related acid sensitive K^+ channel 3 (TASK-3 or $K_{2P}9.1$), as seen in figure 1.5.4.1, is a pH gated member of the K_{2P} super family [Enyedi et al, 2010], and is 374 amino acid encoded by the KCNK9 gene of chromosome 8 [Enyedi et al, 2010].

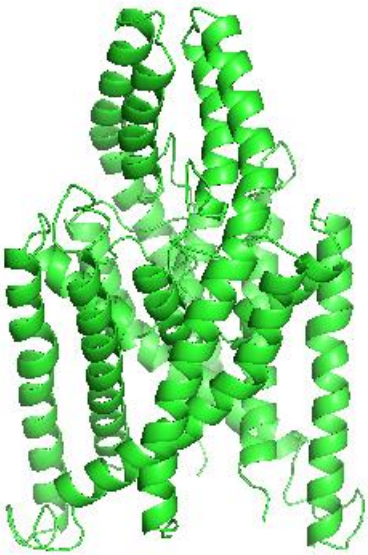

Figure 1.5.4.1: Model to demonstrate the TASK-3 protein dimer morphology from a side view, as constructed by PyMol, based on a model donated from Dr Kevin Cunningham.

TASK-3 is highly expressed with motoneurons through the body [Enyedi et al, 2010], and its presence has been noted in human right arterioles on the membrane of the cardiomyocytes, however, only in heterodimer formation [Rinné, *et al*, 2015].

As the fellow member of the acid sensitive $K_{2P}S$, TASK-3 still functions in a voltage independent manner to demonstrate outward rectification yet shows a greater open potential at higher voltages and proves less sensitive to changes in extracellular pH changes. TASK-3 induces maximum function at pH 7.4 and despite pH measure by protonation of the same H98 as TASK-1; TASK-3 demonstrates acidic inhibition with a pK value of 6.7 and Hill coefficient of 1.8-2 [Enyedi et al, 2010]. However, TASK-3 fails to present H72 and K210, which additionally aid acid sensitivity in TASK-1 [Enyedi et al, 2010].

TASK-3, similarly to TASK-1 does contain an ability to obtain pathological morphology; effecting electrical neurons, which are expressed as dominant negative KCNK9 mutations, due to the exclusive expression of TASK-3 on the maternal allele. These mutations usually result in mental retardation and character dysmorphisms [Enyedi et al, 2010].

1.5.5 TASK-1 and TASK-3 heterodimer concatemers

As mentioned, KCNK3 forms dimers by joining another KCNK3 α-subunit, or a α-subunit of the closely related, acid-sensitive KCNK9 channel, creating a homodimer or heterodimer respectively [Bohnen, *et al,* 2017].

Heterodimer formation is permitted between TASK-1 and TASK-3 as both prove each other's closest molecular relation, exhibiting 60% similarity with highly conserved transmembrane segments, pore regions, and extracellular loops; yet the COOH termini show less similarity. This induces equal expression of both homo- and heterodimers in native tissues, where if the ratio of expression is appropriate, TASK-1 and TASK-3 heterodimers are assembled in equal efficiently to the homomeric channels [Enyedi et al, 2010].

Further, assembly of heterodimers channels increases the diversity of potassium channels that cells present [Enyedi et al, 2010]; and it is predicted that expression would consist of 25% TASK-1 homodimers, 25% TASK-3 homodimers and 50% heterodimers, which would be further split to demonstrate different concatemers: 50% TASK-1/ TASK-3 and 50% TASK-3/TASK-1. This suggests that net potassium current is a result of 3 populations of channels [Bohnen, *et al,* 2017].

TASK-1/TASK-3 heterodimers have been reported to account for 52% of the background potassium current in motoneurons, 44% of the outward potassium current in cerebellar granule neurons and 75% of the pH sensitive background potassium current presented in rat carotid body glomus cells. More so, Enyedi et al, 2010 observed the expression of TASK-1/TASK-3 heterodimers on cardiomyocyte membranes of the human right arterioles [Enyedi et al, 2010/Bohnen, et al, 2017].

Functionally, heterodimer formation between TASK-1 and TASK-3, results in an inheritance of disproportional distinct biophysical, regulatory and pharmacological features of the parent monomers. For example, heterodimer construction induces differential pH sensitivity, proving an intermediate pK value that sits between the pK values of the homodimers, yet increased potassium current is seen at pH 7.4, when compared to TASK-1 homodimers channels [Bohnen, *et al,* 2017]. Further, the heterodimer can be distinguished from the TASK-1 homodimer, as the single-channel conductance equals that of a TASK-3 homodimer where extracellular magnesium is presented [Enyedi et al, 2010].

Yet, in other respects, the heterodimer displays traits similar to TASK-1; Zinc and polycationic dye ruthenium red, specifically inhibit TASK-3 homodimer, whereas the heterodimer, like the TASK-1 homodimer, are unaffected. Additionally, $K_{2P}3.1$ demonstrates inhibition by guanine nucleotide binding proteins (G_q, G-protiens) but TASK-3 is less effected, however heterodimers prove intermediate inhibition, yet this is closer to that of TASK-1 [Enyedi et al, 2010].

1.6 KCNK3 Mutation and cardiac pathophysiology

Once mutated, TASK-1 has the ability to induce many cardiac malfunctions. Pulmonary arterial hypertension is one of these and within patients suffering hereditary PAH, 6 distinct mutations in the $K_{2P}3.1$ channel have been identified, all of which exhibited loss of function at physiological pH, inducing life-threatening symptoms [Bohnen, *et al,* 2017]. However, it is also known that TASK-1 mutations, strongly influence the onset of atrial fibrillation (AF), and this can be caused by the loss or gain of KCNK3 activity.

Over the years it has been proven that genetic factors significantly contribute to the pathogenesis of AF, and the uncoordinated atrial depolarizations it associates [Liang, *et al,* 2014/ Schmidt, *et al,* 2015]. Concerning TASK-1 channelopathies as AF initiators; there are various mechanisms of dysfunction induced by mutation. These include incorrect protein trafficking, meaning KCNK3 expression is limited or surplus; defective $K_{2P}3.1$ channel assembly, so they are unable to operate; and TASK-1 electrophysiological dysfunction, due to electrical remodeling and gating mechanisms. The mutation-specific severity of a TASK-1 alteration depends on the location of the alteration leading to channelopathy and electrical remodel [Bohnen, *et al,* 2017].

$K_{2P}3.1$ is predominately expressed in the heart where it promotes repolarization of the cardiomyocytes [Schmidt, *et al,* 2014b]; and it has been proven that patients with chronic atrial fibrillation (cAF) experience sever electrical remodeling [Wiedmann et al, 2018] due to enhanced TASK-1 activity. This has been demonstrated in the atrial myocytes of patients suffering cAF, as characterized by short APD and increased atrial $K_{2P}3.1$ level [Schmidt, *et al,* 2015/Wiedmann et al, 2018]. Further, the upregulation of $K_{2P}3.1$ has additionally proven to contribute atrial ADP shortening in persistent and permanent AF patients [Schmidt, *et al,* 2014b].

Theoretically, this is induced as increased TASK-1 expression will induce a great background potassium leak, thus will return the cardiomyocytes to the -90mV resting membrane potential faster, meaning that the APD is shortened.

Experimentally, western blot analysis has shown TASK-1 protein levels to be increased in AF, and patch clamp recordings have indicated varied shape and duration of action potentials in atrial cells presenting increased TASK-1 [Harleton, *et al,* 2015]. This proves up-regulation of TASK-1 to be causative of shortening the ADP as previously described in AF. Additionally, Further studies have found TASK-1 transcription to be 2-fold up-regulated in atrial fibrillation [Gierten, et al, 2010], and a study by Sven Limber et al, has proven that by imitating a double in native TASK-1 expression; APD90 is significant shortened by -16%, and APD50 by -13% [Gierten, et al, 2010].

By contrast, mutation has further show pathogenic presentation of TASK-1 by its under expression or dysfunction, reducing the current that is available thought the $K_{2P}3.1$ channel. Theoretically, increasing the time taken for the plateau current of the AP to correct (the refractory period), and for the cell to return to a potential below the firing threshold for the initiation of AP.

Therefore, inhibition of TASK-1 current in the atria, is causative of AF by an increased APD and effective refractory period [Wiedmann et al, 2018/Schmidt, *et al,* 2014b/ Liang, *et al,* 2014]. This is supported by Liang, *et al,* 2014 proving a subtraction of TASK-1 current prolonged ADP90 to 317ms, from 296ms within the wildtype. These factors are additionally observed in the atrial myocytes of heart failure patients due to down regulation of KCNK3 [Wiedmann et al, 2018/ Schmidt, *et al,* 2014b]. Further, TASK-1 inhibition has shown to increase the atrial and ventricular ADP in mice, and reduce heart rate variability; whilst knockout zebra fish prove bradycardia and atrial dilation [Liang, *et al,* 2014]. To add, reduced KCNK3 expression has proven pro-arrhythmic in post-operative canine models, as supported by Harleton, *et al,* 2015, who found TASK-1 inhibition to initiate perioperative AF in humans. More so, in rodents $K_{2P}3.1$ inhibition has also demonstrated an increased ADP, and AF has been presented in porcine with a reduced KCNK3 expression of 81.5% in the right atria and 77% in the left; strongly suggesting this would carry the same effect in humans [Schmidt, *et al,* 2014a].

1.6.1 V123L mutation of TASK-1

Valine 123 is a residue located within the second transmembrane helix (TM2) of TASK-1, which proves highly conserved across animal species. V123 localizes within the side of the channel pore and allows for interaction with alkyl molecules. Further, during pore formation, a stable attractive van-der-Waals attraction is demonstrated between V123 and Leu11 of the TM1, adding structural stability to the TASK-1 pore. However, this stability is lost concerning substitutional mutation of V123 to a Leucine (V123L), preventing bond formation and effect local protein stability [Liang, *et al,* 2014].

Mutation V123L occurs by base mutation of Guanine at position 367, in which it is exchanged for a pyrimidine base, Cytosine, encoding a Leucine at this amino acid position as opposed to a Valine [Liang, *et al,* 2014].

This mutation has been found in a male patient presenting persistent AF with normal atrial diameter but reduced heart variability, as seen in TASK-1 knock out mice. Further, V123L mutated TASK-1 (TASK-1_V123L) was found to induce cardiac abnormalities in 71% of zebra fish, and based on functional expression data in CHO-K1 cells, V123L is estimated to reduce current density by 40% in heterozygous, and 60% in homozygous human patients [Liang, *et al,* 2014].

Additionally, TASK-1_V123L has proven typical of a TASK channels and demonstrates a high sensitivity to pH, however at +20mV, proves a pH of inhibition of a small but significant difference to that of wildtype, demonstrating inhibition at 7.45 and 7.35 respectively [Liang, *et al,* 2014]

Further, functional TASK-1_V123L impact has been measure by whole cell patch clamp, demonstrating a reduced current and depolarized membrane potential compared to wildtype at +20mV [Liang, *et al,* 2014].

1.6.2 Kozak mutation of TASK-1

The Kozak sequence is a section of mRNA that is presented in all eukaryotic cells, this follows optimal sequence of ACCATGG; acting as a consensus sequence and initiating translation processes by ribosomes [Kozak, 1984].

Within TASK-1 encoding mRNA, -3A and -4G are two residues which are important in the protein's translation initiation. These surround the AUG start codon, located 3 and bases upstream respectively; with position -3 proving great dominance concerning ribosomal reignition [Kozak, 1984], and a loss of Alanine or Guanine at this position in other proteins has been known to impair translation leading to some cancers [Signori, *et al,* 2001].

Concerning TASK-1 translation, dual Kozak mutations -3A>U (in which Alanine is replaced with a Uracil), and -4G>A (in which a Guanine is replaced with a Alanine), have proven a reduction of 40% activity concerning luciferase assays, and thus these sequence variants are predicted to reduce TASK-1 expression by 50% [Liang, *et al,* 2014]. This reduction of TASK-1 expression has demonstrated pathophysiological effects in both zebra fish, which prove bradycardia and atrial dilation; and mice which proved a prolonged QT interval, a wide QRS complex, increased ventricular APD and reduce heart rate variability (HRV) [Liang, *et al,* 2014].

However, both Kozak mutations have not been tested individually, yet evidence suggests that -3A>U could greatly induce a reduced TASK-1 expression and cardiac repercussions.

2 Purpose

2.1 Aims

The aim of this investigation is to further characterize the role of the TWIK-related acid-sensitive K^+ channel 1 (TASK-1), in the propagation of atrial fibrillation (AF) within the human heart. Further, this project aims to study the morphology of mutated TASK-1 channels, and TASK-1 interactions with other two pore domain potassium (K_{2P}) channels, as expressed in native tissues. Whilst additionally building a comparison of TASK-1 channels across different species and investigating the equine orthologue.

2.2 Objectives

The main objectives of this investigation are to identify the amino acid sequences of human, equine and rat KCNK3 identifying the channels similarity across species. Then by suitable primer design and QuickChange Site directed mutagenesis, insert modifications into the genetic sequence of the KCNK3 mimicking native pathophysiological AF variations. The mutated genetic constructs will then be suitably transfected, individually and as co-expressions, into cultured tsA-201 cells. These will then be analyzed by use of whole cell patch clamp electrophysiology to obtain relevant current amplitudes and current-voltage relationships concerning the channel type, approximating channel activity and predicting the possible effect of the channel on the action potential duration (APD), thus its ability to induce AF. Whilst characterizing a value for the current produced by the wildtype equine orthologue. Further, cells will be analyzed by use of confocal microscopy to identify any difference in expression or localization of the mutants and co-expressions, compared to wildtype.

3 Materials and methods

Successful conduction of this investigation is based heavily on employment of five main scientific techniques: Cell culture, DNA mutagenesis, cDNA transfection, whole-cell patch clamp electrophysiology and confocal microscopy. These are methods that permit effective production of viable tsA-201 cells; the creation of specifically desired KCNK3 sequences; the insertion of TASK DNA into host cells; the measurement of the ionic current through the expressed channels, and the imaging of DNA containing cells. All work was conducted by obeying health and safety, and aseptic rules.

3.1 Bioinformatics

3.1.1 DNA and amino acid sequence alignments

Amino acid sequences of human, equine and rat KCNK3 were obtained from NCIB as found in appendices 1a, b and c respectively, and further NCIB was utilized to align these sequences; giving percentage homology between orthologues.

Additionally, a coloured Clustal Omega alignment identified amino acids of differential properties within the alignment (appendices, 2i). Whilst Uniprot alignment highlighted the different intermembrane and pore regions (appendices, 2h).

Genetic browser, Ensembl, was then used to identify the location and corresponding KCNK3 nucleotide sequences (upon which primer design was based).

The equine nucleotide sequence was further processed through IDT databases, optimizing the codon sequence and ensuring that the most efficient protein would be created later in the project.

3.1.2 Protein modelling

TASK models were constructed by use of Swiss model or PyMol and were based on TASK-1 and TASK-3 models donated by Dr. Kevin Cunningham.

3.1.3 Primer designs for truncation, optimization and mutagenesis

Primers, as seen in appendices 4, were designed to encourage point mutations exchanging one amino acid with another. This in turn, edited the morphology or function of the general protein by changing bonding strategies or cleaving protein segments.

Forward and reverse complement primers were designed upon the nucleotide sequence obtained from Ensembl Genetic browser, with a target length of approximately 31 nucleotides, as to flank the mutation site by 15 either side – producing specificity of the primer to bind the desired protein region. The length of most primers differed however, in order to maintain lower GC contents; again, increasing specificity whilst preventing hair pin formation and primer dimers, and preventing high melting/annealing temperatures. Making primers of optimum

function, but where higher GC contents were dictated, quick solution was added throughout the PCR process to prevent high GC repercussion.

Once primer sequences of relevant length, annealing temperature and GC content were obtained; primers were created by Eurofins MWG Operon, Huntsville, Ebersberg, Germany.

3.1.3.1 Optimization (TASK-1_K2N/R3Q)

Primers were designed to introduce two high current mutations, K2N/R3Q, into the N-terminus of Wildtype TASK-1. These were created to provide a larger current, exaggerating any effect that mutation might create compared to wildtype currents.

Primer for this double mutation were donated from Dr. Emma Veale.

3.1.3.2 Truncation (TASK-1_Δ250)

As suggested by the amino acid alignment between human and equine orthologues, a truncation of wildtype TASK-1_K2N/R3Q was carried out in order to increase similarity. Additionally, truncation was carried out to identify if truncation of the C-terminus effected Wildtype current, by encouraging differences in the processing and trafficking of the protein, by removal of phosphorylation and 14.3.3 binding sites involved in TASK-1 membrane expression. However, the protein was cleaved leaving the VLRFLT, halothane response element as needed for signal transduction and gate control [Mathie and Veale, 2010].

To cleave the C-terminus, primers were designed to introduce a STOP at position 250, preventing translation of the subsequent amino acids. This was achieved by primers encoding the mutation N250(stop), which involved exchanging nucleotide sequence from AAC (Asparagine) to TGA (stop) at nucleotide position 748-750.

3.1.3.3 Pathological mutations

To further characterize the effects of TASK-1 mutation in AF, primers were designed to mimic the pathophysiogical mutations described by Liang, *et al,* 2010. This would allow for the current values to be obtained, identifying any mutational loss of function; reversal potentials to be calculated, evaluating mutational effects on APD; and finally, for co-expression with wildtype channels, predicting if mutational effect could be reduced based on heterozygous expression.

3.1.3.3.1 Atrial fibrillation (TASK-1_V123L)

Loss of function mutation V123L was induced by exchange of a Guanine to a Cytosine base at nucleotide 367; substituting Valine for Leucine at amino acid 123 upon translation.

Primers for this mutation were donated form Dr. Emma Veale.

3.1.3.3.2 Kozak mutation

Primers were designed to induce both Kozak mutations -3A>U and -4G>A individually. Both bases -3 and -4 both proceed the AUG start codon of TASK-1 so could affect translation of the proteins encoding DNA. Building the mutations separately allows investigation of difference that the individual mutations would pose and explore if one was more potent.

Primers where designed to replace Uracil with Adenine at position -3; and replace Adenine with Guanine at position -4.

3.1.3.4 Equine orthologue

Primers were designed to induce the genetic changes necessary to convert the TASK-1_Δ250 into is corresponding equine orthologue. The changes induced are as listed in table 4.1.2.4.1. Primers were designed to build these mutations the TASK-1_Δ250, reducing the number of mutations needed to build a functional orthologue; and the optimized N-terminus would allow for a difference in current to be identified. A model of the proposed equine orthologue is illustrated in figure 4.1.2.4.1.

Table 3.1.3.4.1: Table to show the mutations needed, and the bases substitution by which they occur; to create a truncated equine TASK-1 protein, from the TASK-1_250.

Amino acid location	Human		Horse		Base mutation	Amino acid change
	Amino acid	Codon	Amino acid	Codon		
35	L	CTG	M	ATG	C103A	L35M
135	L	TTG	F	TTC	G405C	L135F
137	R	AGG	K	AAG	G410A	R137K
145	K	AAG	R	AGG	A434G	K145R
180	H	CAC	Y	TAC	C538T	H180Y

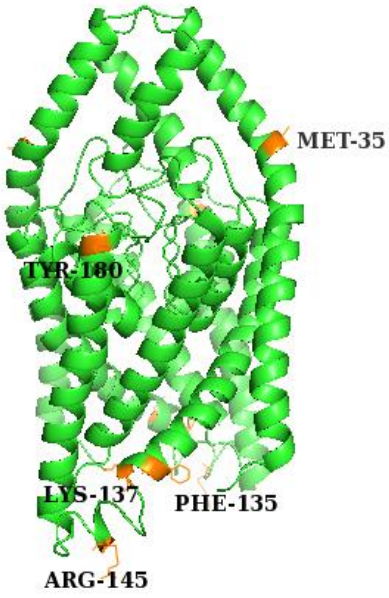

Figure 3.1.3.4.1: Model of the proposed truncated equine TASK-1 protein, from a side view, as build by the insertion of 5 mutations into TASK-1_Δ250. Model build using PyMol based on a wildtype model donated by Dr. Kevin Cunningham.

3.1.4 Sequencing

Mutated TASK-1 Constructs were fully sequenced by Eurofins MWG Operon, Huntsville, Ebersberg, Germany; ensuring correct mutated base sequence had been incorporated.

3.2 Molecular biology

A genetic mutation is any change within a gene that differs to wildtype. This occurs through inherited or environmental factors that induce a change in nucleotide bases and therefore change the codon and amino acid that the gene represents. Most pathological genetic mutations result in the progression of a disease, by the amino acid modification preventing normal protein construction and function, due to differences in bonding patterns.

There are four type of mutation: missense point mutation or substitution; where one base is exchanged for another creating a codon of a different amino acid; deletion or insertions mutations, where a nucleotide or few base pairs are inserted or removed from the sequence – creating frameshift; and duplication mutations, where a piece of DNA is copied multiple times altering protein function. All of these mutations are induced during transcription within the first mRNA creating stage of protein synthesis.

However, in the lab the use of specially designed primers, can alter genetic material, usually by substitution point mutations, creating a desired protein conformation or activity.

Primers aid this motion, by design complementary to the desired mutation site. These adhere by simple electrostatic bonds between single stranded DNA (ssDNA) and the complementary primer sequence; with Adenine binding Thymine or Uracil, and Cytosine binding Guanine. The primers additionally contain an edited base or codon, inducing the desired mutant into the newly synthesized DNA. This is created as the enzyme, Ribonucleic acid polymerase (RNA polymerase) binds the primer at the 5 prime end and transcribes the strand of template DNA until a terminator codon is reach. Resulting in the creation of a mutant RNA which is further translocated into the cytosol, where ribosomes create the mutated protein as encoded.

In order to produce edited KCNK3 sequences, the QuikChange II site-directed mutagenesis method was employed, editing the highlighted regions of difference, and truncating the C-terminus from the protein. However, truncation of the C-terminus was designed leaving the VLRFLT region attached to the cytosolic side of the TM4; ensuring that the truncated proteins were created in a functional structure.

Site directed mutagenesis is an in vitro technique that allows manipulation of protein structure and function. In this investigation, as with projects such as Bohnen, *et al,* 2017, Mathie and Veale, 2010, Cunningham, *et al, 2018*; a QuikChange II Site-Directed Mutagenesis Kit was used. This is a successfully designed kit allowing site-specific mutation in double stranded DNA plasmids without need for specialized vectors. This permits the replacement, insertion or

deletion of amino acids - generating mutants with 80% efficiencies concerning a single reaction.

Mutagenesis by QuikChange II Site-Directed Mutagenesis Kit, occurs in three steps illustrated in figure 3.2.1, and eliminates the need for sub-cloning to produce single-stranded DNA (ssDNA).

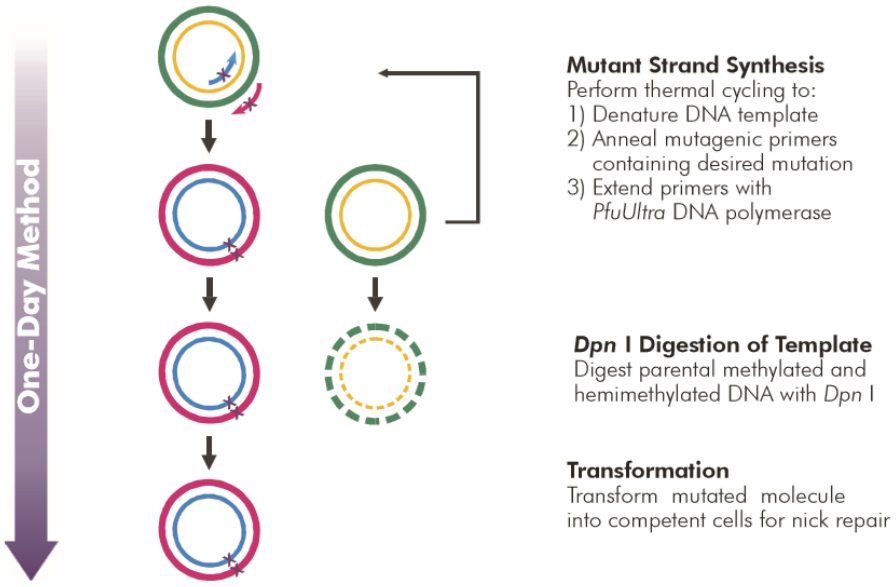

Figure 3.2.1: Figure to illustrate the three steps of the QuikChange II Site-Directed Mutagenesis protocol, and schematic of the DNAs progress throughout the procedure.

The first step of the QuickChange II protocol, is the synthesis of the mutant strand. This occurs in a thermocycler and involves the denaturation of the double-stranded DNA template (either plasmid DNA or DNA) and annealing of desired mutagenic oligonucleotide primers. These primers are designed to complement opposite side of the vector at the mutation site and are further extended during the thermocycler stage of the protocol - producing mutated plasmids with staggered ends. This extension is aided by the use of PfuUltra high-fidelity (HF) DNA polymerase inducing replication of both strands with the highest fidelity. This high fidelity additionally eliminates the occurrence of second-site errors, as does the small amount of parental DNA, and the low thermal cycle number – adding to the process's high efficiency.

Next, the whole sample is treated with Dpn I Endonuclease (Dpn I), this is a specific digestion enzyme that functions on both methylated and hemimethylated DNA. Dnp I uses this trait to be selective for mutation containing plasmids, digesting only parental DNA – where the desired mutation is absent. This stage then filters the genetic material digesting DNA that fails to carry the desired modifications.

Finally, the desired modified material is transformed/transfected into super competent Escherichia coli (E.coli cells). Before being cultured, growing DNA which can be extracted and transfected into tsA-201 cells.

3.2.1 QuikChange II site-directed mutagenesis

Truncation, optimization and mutagenesis of TASK-1 cDNA was carried out by QuickChange site directed mutagenesis protocol, producing the DNA constructs desired to encode mutant channels for analysis by both whole cell patch clamp electrophysiology and confocal microscopy.

The QuikChange site directed mutagenesis kit is a is a protocol which mutates desired genetic sequences by use of polymerase chain reactions (PCR) of the plasmid template which additionally carried an antibiotic resistance to Kanamycin (aiding later in the growth of mutant cells).

To begin primers made by Eurofins, as designed in section 3.1.3, were constituted by dilution was ddH_2O, producing a 1:50 stock, which would go forward into the PCR reaction.

Next a PCR mix was created by combining: 5µl reaction buffer, 1µl plasmid DNA, 1.25µl forward oligonucleotide primer, 1.25µl reverse oligonucleotide primer, 1µl dNTP mix, 1µl PfuUltra HF DNA polymerase; and ddH_2O in quantity to equal a 50µl total reaction volume. However, dependent on primer designs, 3µl Quick solution was factored in where primers proved GC contents >60 %. Quick solution functioned to combat the effects of high GC contents; preventing primer dimers and hair pin structures and increasing the selectivity of the primers.

PCR was then run for 30 cycles allowing the mutagenic primers to anneal to the denatured plasmid, before initiating the extension of mutated DNA as aided by the dNTPs and polymerase. This resulted in the presence of both mutated and parental wildtype double stranded DNA (dsDNA).

Parental wildtype DNA was then digested by DPN-1 enzymes, which prove selective for DAM-methylated DNA. For this 1µl of DNP-1 was added to the PCR product, before placing on a heat block at 37°C for 1 hour.

Mutant DNA was unaffected throughout the digest due to its in vitro production, which does not result in DAM- methylated DNA. However, wildtype DNA originating from Escherichia coli (E.coli), existed in a DAM-methylated state, so was severed by the DNP-1 enzymes. This left only mutated DNA to be transformed into E.coli, as described in section 3.3.5, for continued reproduction of the DNA by use of the bacteria's bio-machinery.

3.2.2 Miniprep plasmid elution

DNA was extracted from transformant E.coli cells by use of a Sigma Aldrich GenElute plasmid mini prep kit; before the DNA was quantified, sequenced and further used to transfect cells.

Cells cultured in broth at 37°C overnight were spun down creating a pellet before pouring off the excess. 200µl resuspension fluid was added to the cell pellet, pipetting up and down to resuspend the sample before vortexing; completely dispersing the sample in solution, as poor resuspension would induce a poor yield. Next, the resuspended cells were treated with 200µl lysis solution to disrupt the cell membranes and release the intracellular materials. Samples were inverted gently and left until the solution turned clear. The lysis solution was not applied for time exceeding 5mins and the samples were not agitated at this stage - preventing contamination and plasmid damage. When the solution had turned clear, 350µl of neutralization solution was added and the solution gently inverted. The samples were then centrifuged at 12,000rpm for 10 minutes.

A column was prepared by adding a GenElute miniprep binding column to a micro-centrifuge tube. 500µl of preparation solution was then added to the miniprep column and spun at 12,000rmp for 1min, before discarding flow through; this maximized the DNA yield that adhered to the column membrane.

After the 10min centrifuge, the clear lysate was then pipetted off with care not to obtain the membrane debris adhered to the surface of the tube. The clear lysate was transferred to the prepared column and spun at 12,000rpm for 1min to dry the sample. The flow through liquid was discarded, and 750µl wash solution added to the column. This was then again spun at 12,000rpm for 1min - removing residual salts and other contaminants. The flow through was removed and the sample again spun to eliminate excess ethanol.

The spin column was then added to a fresh collection tube and 50µl of Elution solution added to the column. This was once more spun at 12,000rpm for 1min, eluting the DNA into the collection tube; where it was available for quantifying. DNA concentration were determined using a Nanodrop spectrophotometer (Implen, Germany), and suitable samples provided 260/280 absorbance ratios of between 1.7-1.9 and a >250µg.ml^{-1} concentration. These were then sent for sequencing or for storage at -20°C.

3.3 Cell tissue culture

The tsA201 cells used in this investigation were obtained from the European Collection of Cell Cultures through Sigma-Aldrich; and all cell culture was carried out following strict aseptic technique as to prevent contamination of the cell lines or media used.

The tsA -201 cell line is produced from human embryonic kidney cells (HEK 293) and are stably transfected with the SV40 large T antigen. These express an epithelial morphology with a pyramidal or rhombic shape and were utilized throughout this investigation as a vehicle to carry and express TASK channels of different species; based on their cellular properties befitting later used procedures. These properties include the cell lines efficiency to grow in culture, and the potent transfectability that the cells present allowing full analysis of the inserted ion channel [Cunningham, *et al,* 2018].

HEK-293 cells are proven to be good hosts for gene expression and allow great numbers of specific protein to be expressed and analyzed [Cunningham, *et al*, 2018/ Thomas, *et al*, 2005]. Despite the HEK-293 cell line failing to provide the same complexity of cellular architecture and sub-cellular biochemistry presented in native neurons [Thomas, *et al*, 2005]. They remain a valuable tool in the reconstruction and expression of many types of protein; allowing for protein and ion channel activities to be measured. Whilst removing the biochemical and topographical interferences of other endogenous proteins [Thomas, *et al*, 2005].

Further, the ability to produce desired HEK cell phenotypes by introduction of exogenous DNA; is permitted by the cells ability to withstand various transfection methods. The efficiencies of these have proven variable and sensitive to the quality of preparation reagents, yet HEK-293 cells have been known to provide efficiencies ≤ 100%; even concerning punitive transfection methods such as calcium phosphate [Thomas, *et al*, 2005],

For optimal experimental results to be obtained it is suggested that cellular samples are maintained at approximately 70% confluence [Thomas *et al*, 2005]. For this to be achieved it is important that stock densities, as preserved in incubated flasks, are kept low upon passage of the cells. Meaning that that the desired % confluence is reached within a suitable time frame for transfection methods to be applied.

Seeding quantities of 70% confluence have additionally confirmed optimal for transfection specifically via Calcium phosphate methods. This allows an ideal sample of around $5x10^3$ cells to be transfected on a 22mm coverslip, ready to undergo electrophysiology 24 hours post transfection [Thomas *et al*, 2005].

However, tsA-201 cells do present endogenous currents from voltage gated potassium channels, which are essential for the cell's survival. From this reason a suitable electrophysiological protocol was employed to eliminate the contamination of these during current recordings.

3.3.1 Cell passage

Cells were regularly passaged in order to produce and maintain viable tsA-201 cells lines to use as experimental hosts. This involved the movement of the cell line from one flask to another permitting a change of media (Sigma-Aldrich, Dorset, UK) to preserve cell health; whilst additionally, diluting the cell line - controlling confluence of the population. This again sustaining cell health and maintaining stocks at suitable confluences to undergo further cell culture and experimental techniques. Cell stocks incubated at $37^oC/5\%$ CO_2 in T25 and T75 flasks, yet most regularly passaged stocks were maintained in T25 flasks.

Passage began with removal of T25/T75 flasks from the incubator and cell viewing under a microscope, ensuring cells were 70-80% confluent, healthy and free from contamination.

Next, working in a fume hood (HeraSafe, Heraeus), supernatant media was poured into a waste beaker and Trypsin added (2ml for T75, 1ml for T25). Trypsin is used

as the dissection factor to free cells from the flask surface, as aided by gentle agitation of the flask. Following this 5ml media was added to the flask, also assisting in washing cells from the flask surface and repeated pipetting ensuring thorough mixing of solution. 5ml solution was then moved to a 15ml falcon tube and centrifuged at 800rpm for 3 minutes at room temperature.

The spun sample moved back to the fume hood and again the supernatant was poured off - leaving just the cell pellet in the tube. Tapping the falcon tube on work surface resuspended cells and the addition of 5ml media (whilst pipetting up and down) thoroughly resuspend cell pellet in solution.

Next in order to continue cell stocks; new T25/T75 flasks had to be prepared. New flasks must be labelled with cell type, passage number and date before the addition of 20ml new media to T75 and 5ml new media to T25 flasks. Then 0.5ml resuspended cell stock solution was added to each flask before incubating at 37^{o}C/5% CO_2. 70—80% confluence is reached in 2-3 days (T25) or 4-5 days (T75).

3.3.2 Cell plaiting

Splitting plates were created from confluent T25/T75 cell stocks during the cell passage process. These produced cells mounted on PDL-coated cover slips in suitable quantities to undergo transfection.

This proceeded by further dilution of resuspended cell stock (as created in cell passage to make new flasks), by moving 0.5ml cell stock solution to a new falcon tube containing 8.5ml of fresh media, again pipetting up and down to ensure consistent cell distribution throughout the mix. 0.5ml was then added to each well of the labelled splitting plate. Pressing the glass coverslip to the bottom of the well in sequence; preventing cells growing underneath. Plates were incubated at 37^{o}C/5% CO_2 for 24-48 hours before transfecting. Ensuring 70-80% confluence was reached for calcium phosphate transfection, and 80-90% confluence for TurboFect transection.

3.3.3 Calcium phosphate DNA transfection

3.3.3.1 Principle

Transfection is the process by which genetic material in the form of deoxyribonucleic acid (DNA) or ribonucleic acid (RNA), are introduced into eukaryotic cells. There are many protocols published for this, yet all achieve the same objective: to transport genetic material (usually in the form of complementary DNA, cDNA) to the inside of the cellular membrane of the host, where it can incorporated into the native DNA, and the encoded proteins expressed by use of the host cells bio machinery.

Calcium phosphate is a quick, simple, efficient and inexpensive method of DNA transfection first developed by Graham and Van der Eb, 1973 [Graham *et al*, 1973/Chen, 2012]. The procedure allows introduction of a desired recombinant DNA sequence into eukaryotic cells via the use of a calcium phosphate-DNA precipitation. The protocol is less labor intensive than other transfection methods such as electroporation and is applicable to large scale production of transfectant cells [Graham *et al*, 1973]. Where, due to the absence for need of specialist

equipment, it is commonly used for co-expression of plasmids and packaging viruses [Chen, 2012].

During the process, the insoluble calcium phosphate precipitate binds cDNA creating a positively charged complex assisting its electrostatic adherence to the cellular membrane, before entering the cell via endocytosis [Chen, 2012]. Resulting in transient cDNA expression in target cells producing stable transformants. The calcium phosphate-DNA precipitate remains dormant, allowing healthy survival of the transfected cell [Chen, 2012].

As a method, calcium phosphate transfection has proven efficiencies close to 100% depending on the cell lines used [Chen, 2012], however these can vary based on pH due to the maturity of the culture media [Thomas *et al*, 2005].

Further, the efficiency of the procedure can be hindered by the density of the initially seeded cells, as if low, success rate can be unpredictable [Graham *et al*, 1973], due to the process of endocytosis and engulfing the charged DNA complexes rupturing the plasma membrane, leading to cell death. For optimal success it is proposed that plates are of 70% confluence and covered by approximately $5x10^3$ cells [Thomas *et al*, 2005]. Additionally, it is advised that the cDNA intended for transcription, is produced in an endotoxin free buffer, and added to the cells in quantities of 10µl DNA per 500µl of suspended cells [Thomas *et al*, 2005]. With 25% of the final DNA volume complying a genetic flag, such as a Green Florence Protein (GFP) plasmid [Thomas *et al*, 2005], allowing identification of the effectively transfected cells [Chen, 2012].
The calcium phosphate transfection method allowed endocytosis of cDNA into tsA-201 cells; inducing membrane expression of both wildtype and mutant TASK channels for analysis by whole cell patch clamp electrophysiology.

3.3.3.2 Method

To begin tubes A and B were constructed. To transfect a 4 well plate, tube A contained: 500ng cDNA, 500ng GFP, 22.5µl $CaCl_2$, with ddH_2O used to alter the tube A reaction volume to 100µl; and tube B contained: 100µl heaps buffer solution (HBS) and 1.8µl phosphate buffer (Na_2HPO_4).

Both tubes were vortexed and mini centrifuged before the contents of tube B was transferred dropwise into tube A, allowing a fine precipitate to form, as clumped DNA cannot be endocytosed. The mixture was left at room temperature for an optimum time of 15mins, allowing the $CaPO_4$/DNA precipitate to form. If the mixture is not left long enough then insufficient precipitate will form, reducing transfection rate; yet if left too long, large cytotoxic aggregates will form, also reducing transfection efficiency.

Next, the tube was mixed by pipetting before transferring 50µl of the solution into each well of the splitting plate. Ensuring the mixture is equally dispersed around the well. Then, labeled plates were incubated at $37^oC/5\%$ CO_2 for 4hours.

After 4 hours, cells were washed by aspirating excess media and replacing with 1ml PBS; aspirating the PBS, then again adding 1ml fresh PBS, before removing

the PBS and adding 0.5ml new media. Plates were then incubated at 37°C/5% CO_2 for 24hours before electrophysiology.

3.3.4 TurboFect DNA transfection

3.3.4.1 Principle

TurboFect transfection is a fast and highly efficient transfection method allowing DNA plasmids to be expressed within eukaryotic cells. The process involves the use of the use of Thermo Scientific TurboFect Transfection Reagent which proves easy to use with no required reconstitution or optimization for most cell lines [Thermo Scientific, 2018].

TurboFect Transfection Reagent consists of sterile solution and a cationic polymer, which interacts with negatively charged cDNA, forming small complexes that are highly diffusible and easily endocytosed, based upon the electrostatic attraction of the positive complex and the cells negative nucleus [Thermo Scientific, 2018].

Once within intercellular space, the reagent buffers endosomal pH, acting as a proton-sponge; accumulating protons and allowing passive chloride influx. This induces osmotic swelling of the endocytosed complexes, leading to their rupture, releasing the cDNA which is then translocated to the nucleus [Thermo Scientific, 2018].

Overall, TurboFect provides high transfection efficiencies in both the presence and absence of serum media; with protocols permitting minimal cytotoxicity and allowing cDNA uptake in a softer manner resulting in better quality and tact membranes compared to other transfection methods. Whilst still allowing for the stable creation of single and co-transformants, inducing suitability for many cell lines and further proving useful in cell imaging assays involving GFP or luciferase reporters, such as confocal microscopy [Thermo Scientific, 2018].

3.3.4.2 Method

The TurboFect transfection method induced membrane expression of both wildtype and mutant TASK channels by allowing endocytosis of cDNA into tsA-201 cells. This is a kinder transfection method then the calcium phosphate protocol; providing cells with better tact membranes, permitting quality staining and imaging of cells via confocal microscopy.

To begin, tubes containing 100µl serum free media, 1.5µl TurboFect reagent, and 500ng GFP labeled PAC vector plasmid were constructed; one tube must be created for each well to be transfected. TurboFect reagent should be vortexed before each addition to a tube to ensure its thorough mixing.

Leave this to stand for 20mins approximately, but do not exceed this time as the TurboFect reagent and aggerates prove cytotoxic – reducing cell yield.

After 20mins, evenly disperse 100µl from each tube into each well, label, and incubate at 37°C/5% CO_2 for 24 hours before staining for confocal microscopy.

3.3.5 Transformation

During mutagenesis, successful PCR product was then transformed into super competent E.coli cells before being grown on Kanamycin selective agar plates. Super competent E.coli were used as the cells prove sensitive to uptake small quantities of DNA, such as samples produced by PCR.

To begin transformation, 40µl super competent cells were removed from -80°C storage and allowed to defrost on ice, before 3µl of PCR product was added to the cells. This when then left on ice for 15mins, before being heat shocked at 42°C for 50 seconds, inducing the E.coli to uptake of external DNA. The sample was returned to ice for 2mins, before 350µl of broth was added, and samples placed on a shaker at 37°C for 1 hour.

3.3.6 Selective Kanamycin resistant agar plates

Antibiotic Kanamycin agar plates were created to allow the selective growth of transformed E.coli colonies. This was utilized as part of the mutagenesis process, as cells were transformed with plasmids containing the desired TASK construct plus a resistance to Kanamycin. This allowed only E.coli containing the desired cDNA constructs to proliferate, as untransfected cells by failing to carry the Kanamycin resistance gene, were therefore killed off.

Resistant agar was constructed by the addition of 1µl Kanamycin per ml of agar, with 100-200ml agar made at one time; producing 4 or 8 plates respectively.

3.3.7 Kanamycin resistant cell culture

Selected transformant E.coli cell cultures, as grown on Kanamycin agar plates, were then transferred to a falcon tube and cultured in broth, permitting the further growth of successfully transfected E.coli colonies suitable to undergo mini-prep DNA extraction, as seen in section 3.2.2.

To begin, near a Bunsen flame 5ml broth was added to a labeled and sterile falcon tube, along with 5µl Kanamycin, this again made the growth of the transformed E.coli selective, as only the cells containing the desired mutant and Kanamycin resistant plasmid would grow. Next, using a pipette tip a single colony from the incubated plates was selected, and the pipette tip dropped into the falcon tube containing broth. The falcon tube was then moved to the shaker where it remained at 37°C overnight.

3.4 Whole-cell patch clamp electrophysiology

Task channel currents was measured from transfected tsA-201 cells in a whole-cell configuration in voltage clamp mode; permitting the measurement of ion movement over the whole surface of the cell at different voltages.

Whole cell patch clamp electrophysiology is a protocol that allows for the recording of currents through multiple channels simultaneously, providing a cumulative current value for the channels expressed over the whole cell membrane. Further, in whole cell configuration, the pipette interior and cell cytosol are provided contact, allowing for current recording to be conducted in

real time, proving useful when analyzing the channel effects of drugs and external stimulus [Thomas, *et al,* 2005].

Whole cell configuration is achieved by use of a glass micropipette, that upon application of pulsating negative pressure, is used to break through and form continuity of the cell membrane, thus allowing for the internal solution of the micropipette to contact the intracellular medium. The internal solution within the pipette is constructed to mimic the ionic conformation of the cytosol and so carries any cellular difference in charge to the wire electrode where it is measured.

The theoretical basis behind the whole cell patch clamp technique, and the pivotal concept that allows for the calculation of cellular current, is Ohms law. This was developed in 1825 by Gorg Ohm and is a law that states:

The ampere (I) in a circuit is proportional to the voltage (V) and inversely proportional to the resistance (R).

This described the relationship between I, V and R in a circuit, and concerning electrophysiology allows a cells current to be calculated by balancing of this law. Ohms law can be manipulated to find any of the I, V or R, as seen in figure 3.4.1.

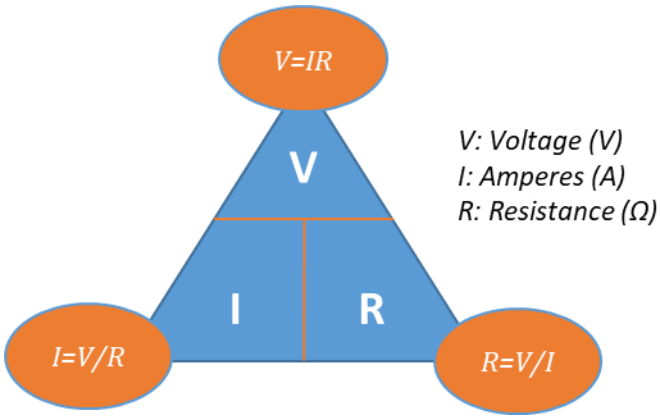

Figure 3.4.1: Triangular presentation of Ohms law; allowing for voltage (V), Amperes (A) or resistance (R) to be calculated within a circuit.

However, for Ohms law to apply, the parameters manipulated must concern a circuit formation. Concerning whole cell electrophysiology, circuit formation is constructed by use of cells in a bath; a micropipette that contacts the cells; a wire electrode within the glass pipette, and a head stage which is connects the wire electrode to a ground electrode within the bath. This is displayed in figure 3.4.2, which further illustrated the composition of the amplifier, digitizer and PC which are involved in the conversion of the current into an examinable recording.

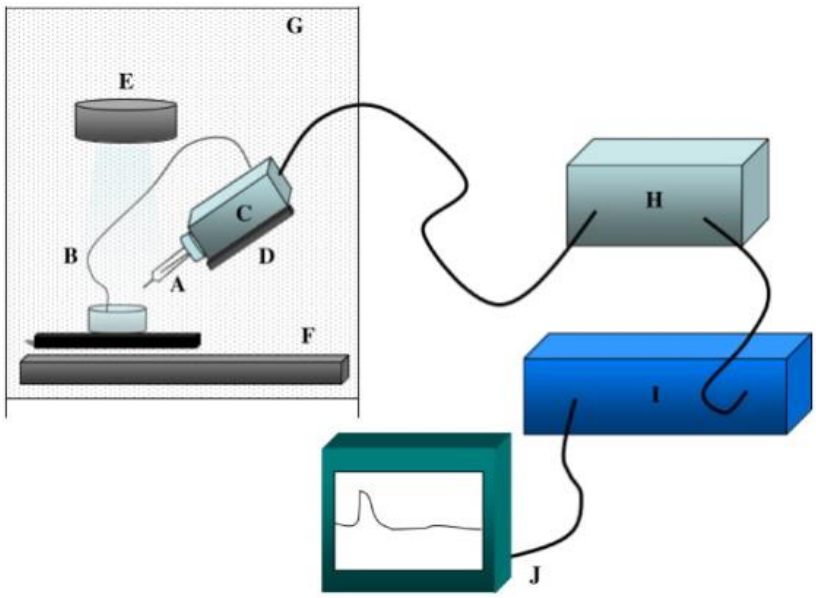

Figure 3.4.2: Figure to show the circuit formation in preparation for whole cell patch clap electrophysiology, where A, Ag silver wire electrode; B, ground electrode; C, head stage; D, micromanipulator; E, inverted microscope; F, air table; G, Faraday cage; H, digitizer; I, amplifier and J, PC.

Within this project, channel currents were measured in a whole-cell, voltage clamp configuration using a step-ramp protocol. This allowed the quantification of the current differences at -40 mV and -80 mV, allowing for the measure of current where the hosts cells endogenous current will be least. Whilst further, allowing the measurement of current over a range of voltages - identifying at which voltage there was no current; in respect to identifying the resting membrane potential, as posed by that specific channel or mutant channel.

The step ramp protocol as further explained in methods section …, permitted the calculation of the current by the known voltage and the measured resistance at each phases of the protocol; as to represent channel activity, dysfunction or alteration.

Additionally, current acquisition is aided by the reversible reaction presented by the silver chloride coating of the silver wire electrode:

$$Ag + Cl^- \rightleftharpoons AgCl + e^-$$

This enables the flow of potassium ions to be converted into a flow of electrons within the silver wire, which can then be measured [Cunningham, *et al*, 2018].

3.4.1 Electrical circuit composition

The whole cell current was measured by creation of a circuit, as seen in figure 3.4.2, linking the glass pipette that filled with internal solution and housing the high conductance wire electrode (composed of silver and silver chloride (Ag/AgCl)); to another AgCl electrode in the second well, used both to ground the solution within the bath chamber and to close the circuit. Additionally, the whole circuit was contained within a Faraday cage to decrease external interference.

This circuit formation allowed for a range of voltage to be applied and the corresponding current measured. These circuit parameters were controlled by Computer software (Clampex 10.2), which dictated voltage stimulations and their timings to fulfill the specific protocol.

A digitizer (Digidata 1440A) created a link between the computer software and the rig circuit system. This functioned to convert the computers stimulus into voltages articulated through the wire electrode and glass pipette (as maneuvered by a Patch-star micromanipulator (Scientifica)), setting the voltage of the circuit. And in reverse, converting electrical signals from the circuit to digital signal to be read and recorded by the computer. This was aided by using an amplifier (Axopatch 220B), filtering the extracellular current in the external bath, as measured by the ground electrode, eliminating interference and converting this to a current reading.

3.4.2 Solutions

External solution

The external solution that was designed to mimic extracellular medium and filled the perspex recording chamber was composed of (in mM) 145 NaCl, 2.5 KCL, 3 MgCl2, 1 CaCl2 and 10 Hepes (pH to 7.4 using NaOH).

Internal solution

The internal solution that was designed to mimic intracellular medium and filled the glass pipettes contained (in mM) 150 KCL, 3 MgCl2, 5 EGTA and 10 Hepes (pH adjusted to 7.4 with KOH).

3.4.3 Glass pipettes

Glass capillaries 1.5mm were vertically pulled from thin walled borosilicate glass on a Narishige PC-10 microelectrode puller; producing pipettes with tip diameters of 1-2µm and resistances between 3-7MΩ when filled.

3.4.4 Protocol

Cover slips of 70% confluent transfected tsA-201 cells were submerged into the first well of a two well Perspex bath chamber filled with external solution at pH 7.4, as to mimic extracellular medium; and weighted down with a small application of Vaseline to the underside of the slide. The bath chamber was positioned on the fixed stage of an inverted microscope (Diaphot; Nikon, Tokyo, Japan), with epifluorescence, positioned on an air table and situated within a Faraday cage, preventing vibrations and limiting electrical interference to recordings.

Further in interest of reducing interference, the two wells of the bath chamber are connected via a narrow channel, allowing for the second well to be used in grounding the bath solution by use of a silver chloride pellet and grand electrode. Additionally, the flow transducer used to remove excess solution whilst perfusing cells, is also located in the second well of the bath chamber, separating both suction and recording pipettes.

Once the bath chamber is positioned under the microscope with the ground electrode, perfusion, and flow transducer attached; a suitable cell for patching was

then identified. Green florescence evidenced cells of successful DNA/GFP transfection; and only these cells were selected for electrophysiological recording. More so, isolated cells of typical morphology were desired.

A glass micropipette was then 33% filled with internal solution of pH 7.4, as to mimic intracellular medium, and placed into a Patch-star micromanipulator where it encases the Ag/AgCl wire electrode. The micromanipulator was then used to position the pipette within the microscopes field of vision and lower the pipette into the external solution of the bath chamber. The pipette resistance was electronically calculated by use of Ohms law; where the pipette resistance was equal to the voltage applied/the current of the circuit. Pipette resistances of 3-7MΩ were optimum for the protocol, and this resistance was manually off set on the amplifier, bringing total resistance to 0.

The micromanipulator was then used to lower the pipette tip towards the selected cell, and the pipette resistance increased as the small glass pipette tip (1-2um diameter) was approached the cell membrane. As the pipette tip and cell membrane made contact, the current able to pass though the pipette and cell membrane was reduced, and with a small application of negative pressure an increased seal resistance of +1Giga-Ohm (>1GΩ) was formed, with higher resistances indicating better seals. This eliminated any leakage between the glass pipette and the cell membrane, as the sides of the pipette form continuity of the cell membrane; additionally, allowing contact between the pipette content and the intracellular medium.

At this point the pipette was acting as a capacitor by separating and maintaining the charge differences between the internal and external solutions. However, additional pulses of negative pressure, aided by external perfusion at a rate of 4–5 mL min^{-1}, broke the cell open, forming whole cell configuration and allowing a low resistance entrance of the pipette content to the whole interior of the cell. The voltage was then transferred through the cytoplasm and cell membrane to the external bath solution completing the circuit. However, the cell membrane was now acting as a capacitor, yet this proved biological significance as membrane conductance represented channel activity of all open channels; and further allowing the normalization of recorded currents, and a prediction of cell size. This prediction was based upon the fact that:

$$Cm = \frac{(\text{Ɛo} * A)}{d}$$

Where Ɛo = lipid property of the membrane; A = cell surface area; d = membrane thickness; and, Ɛo and d remain fairly consistent. Yet, controversially the capacitor action of the membrane induced distortion in changes of voltage; and produced extension between protocol steps if the cells being patched were joined as a pair or attached to a colony, hence isolated cells were desired.

Once a whole cell configuration was achieved, Clampex 10.2 was then used to run the specific K_{2P} protocol, whilst recording channel currents at the varying voltages. However, only cells with holding potential currents of ≥0pA, and -40mV

currents of ≥ -200pA were included, as to exclude recordings with poor access. A minimum of 5 sweeps were then recorded of each cell, and the manual cell capacitance (Cm, pF), membrane resistance (Rm, MΩ), access resistance (Ra, MΩ) and series resistance (MΩ) were recorded for each cell.

3.4.5 K_{2P} voltage protocol

A step ramp protocol allowed for the K_{2P} currents generated, to be differentiated from that of the endogenous voltage gated potassium channels that tsA-201 cells express. All data were collected at physiological pH (7.4) at room temperature (22^{o}C approx.) and involved four voltage steps constructing a sweep. Each sweep lasted 1.5 seconds(s) and sweeps were conducted every 5s.

As illustrated in figure 3.4.5.1, the step ramp protocol measured the whole cell currents at the holding potential of -60mV, before hyperpolarizing the cell to -80mV for 100ms. Next cells were repolarized to -40mV for 500ms before undergoing additional depolarization to -120mV for 100ms, preceding a 500ms voltage ramp from -120mV to +20mV. At +20mV a depolarization to -80mV was endorsed for 100ms, before returning to the holding potential of -60mV, concluding the sweep.

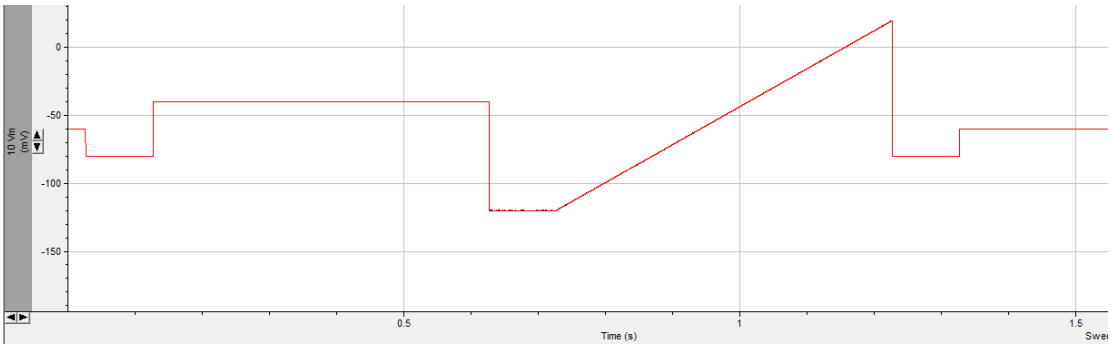

Figure 3.4.5.1: Figure to demonstrate the shape, timing and voltages involved in the K2P step-ramp protocol, with the voltage of each step of the protocol (plotted on the x-axis (mV)) plotted against the duration of the step (time on the y-axis (S)).

The step component of this protocol allows for the quantification of difference in current at -40 mV and at -80 mV. These voltages were chosen as -80mV allows current readings close to the equilibrium potential of potassium (-90mV); and -40mV allows current analysis though the K_{2P} channel in a less polarized conditions, whilst permitting the recording of current where endogenous current is lowest; avoiding contamination from the tsA-201 endogenous voltage gated K^{+} channels.

The ramp component, however, allows the measurement of current over a range of voltages, permitting a measure of the voltage (Vrev) at which the current was 0pA; allowing a prediction as to how the channel has manipulated the resting membrane potential, and may affect the cardiac APD, as higher Vrev potentials will induce a shorter APD.

3.4.6 Data analysis

Analysis of data commenced by averaging the recordings for each cell and measuring the outward current amplitudes from the -80mV to −40 mV step by use of pCLAMP, version 10.2 (Molecular Devices). Further, cell densities were calculated using these average currents by:

$$\text{Cell capacitance } (C_m) \text{ / Current (pA)} = \text{Current density (pA/pF)}$$

Finally, pClamp was used to calculate the reversal potential (Vrev) of the voltage-current relationship, as illustrated within the ramp step of the recording, before all data was teste for significance.

Statistical analysis involved the use of both unpaired T-tests and Tukey analysis of variance (ANOVA), identifying statistical differences between the means of data sets, as calculated

Unpaired T-tests were conducted when comparing two variables, with P-values below 0.05 considered to be statically significant. Tukey ANOVA was employed for multiple comparison tests, rating statistical significance by * where: $P<0.05$ (*), $P<0.01$ (**), $P<0.001$ (***) and $P< 0.0001$ (****).

Graphs as designed by Prism (GraphPad software) represent mean data ± standard error of mean (SEM), and 'n' represents the number of individual cells.

3.5 Confocal microscopy

Confocal microscopy was used to investigate potential differences within the localization and trafficking of the wildtype and mutant TASK channels, as examined by whole cell patch clamp electrophysiology. This was permitted by the creation of high-resolution images of tsA-201 cells that had undergone staining with selective fluorescent markers - allowing the visual identification of the quantity of channel expression.

The cells used to complete these confocal imaging studies were of the same tsA-201 cell line; cultured in the manner prior to transfection, and were transfected with the same genetic sequences as used within the electrophysiological studies. However, in interest of obtaining quality images, transfection of these cells commenced via the TurboFect method identified in section 3.3.4**,** as opposed to the calcium phosphate method used in the electrophysiological studies, allowing cells with better quality membrane moving forward into the staining and fixation processes. And, DNA constructs were placed in a pAcGFP1-N1 vector (Clontech, USA), tagged tags a green fluorescent protein (GFP) to the TASK channel, inducing a green fluorescence of transfected cells, and of each task protein within the cell.

3.5.1 Principle

Confocal microscopy is a technique that allows the location and quantity of protein to be examined within cells. This enables the production of high-resolution images, permitting the visual analysis of transfected channels and their mutants, comparing

the expression and localization of the channels that were put forward to electrophysiology tests.

For confocal to prove successful, desired protein sequences need to be encoded on a pAcGFP1-N1 vector (Clontech-Takara Bio Europe), which tags a green fluorescent protein to the C-terminus of the channel protein; and ffurther, cellular parts must also be labelled with selective fluorescent markers, to provide contrast between the different components.

This contrast is produced by the use of precise wavelengths of light that cause specific material, or stained cell components to fluoresce, based on the emission spectrum of the stains used. However, confocal microscopy builds upon this by utilizing pinhole filtration of the laser beams that excite the electrons of the stains within the viewable sample section. This reduces background fluorescence from outside the field of the lens, and produces a clearer and sharper image [Foldes-Papp, *et al,* 2003].

Thus, visual comparison of the investigated protein in relation to cellular components is conducted. But interest of obtain valid results, blank and part stained samples are additionally imaged, ensuring that the interaction of the stains with the cells and protein in question prevent modification, giving false positive or inaccurate results.

3.5.2 Cell membrane staining and fixation

Cells transfected in 4 well splitting plates via Turbofect, were carefully washed 3 times with 1ml PBS, preventing a reduced cell yield, before replacing the PBS on third wash with 1ml pre-prepared Cell Mask Deep Red (CMR) (Thermofisher Scientific) plasma membrane stain (1:1000 CMR in pre-warmed PBS). Cells were then incubated for 7-10 minutes at 37^{o}C/5% CO_2.

Cells were then prepared for fixation. These were washed 3 times with 1ml PBS, before replacing the third wash of PBS with 1ml 2% paraformaldehyde, before incubating at room temperature in darkness for 18-20mins, but not exceeding 20mins. Cells were then again washed in PBS 3 times.

Next a 1:500 dilution of Hoechst 33258 (Sigma Aldrich) in PBS was created, producing a nucleus stain, of which 1ml replaced the third wash of PBS following fixation, before incubating for 10mins at 37^{o}C/5% CO_2. Following incubation, cells were again washed 3 times in PBS.

Finally, using Vectashield anti-fade mounting medium, cover slips were mounted face down, onto glass slides that had been pre-washed in pure ethanol and allowed to dry.

3.5.3 Protocol

When dry, the created slides were imaged on a Zeiss™ Laser Scanning 880 (Carl Zeiss, Jena, Germany) confocal microscope, situated on an air table to prevent vibrations. The microscope was then connected to a PC allowing for Zeiss Efficient

Navigation (ZEN) (Version: Black) software to be used for orthogonal projections (XY), and additionally for Adobe Photoshop to allowing image editing (All scale bars were calibrated to 5uM).

Cells were then unidirectionally frame scanned with a 63X oil objective lens with a 1.4 numerical aperture, with pin holes set to 1 airy unit (AU) and x2 zoom; producing 12-bit images in a frame of 764 x 764, X*Y respectively. Averaging x8 collected in line mode.

Cellular components and GFP labelled protein were then identified by use of different lasers. Nuclear Hoechst-33258 staining - identifying the cell's nucleus, was imaged with the 405nm diode (354nm Ex/461nm Em); GFP – identifying the transfected protein, was imaged using an argon 488nm laser line (495nm Ex/519nm Em); and membrane staining was imaged using the Helium-neon laser (650nm Ex/655nm EM).

Control images were additionally obtained ensuring that pixels within the sample quadrants were not created arbitrarily and excluding false positive results induced by the stains and labels used. These included the imaging of all samples in presence and absences of CMR membrane stains, untranfected cells, and GFP and CMR only cells.

3.5.4 Analysis

Images were visually analyzed - comparing the localization and expression of the channel constructs. Protein localization at the membrane was analyzed by the crossover of both CMR and GFP florescence, whilst intracellular localization would be identified by GFP florescence from the cytosol. Protein expression was further evaluated by the rate of florescence presented, as this a correlated representation of expression level.

4 Results

4.1 Bioinformatics

4.1.1 DNA and amino acid sequences and alignments

Amino acid sequences of human, equine and rat KCNK3 were obtained from The National Center for Biotechnology Information (NCIB), as found in appendices 1a, b and c respectively. Proving a 394 amino acid sequence for humans; a 403 amino acid sequence for equines, and a 411 amino acid protein for rat.

Furthermore, with intent to co-express KCNK3 with KCNK9; human and equine KCNK9 sequences were also gathered from NCIB as found in appendices 1d and 1e respectively.

Additionally, NCIB was utilized to align sequences providing a percentage of identical homology between orthologues. The NCIB alignments of KCNK3 amino acid sequences for human and equine; human and rat; and equine and rat, provided homology values as described in table A. Human and equine sequences proved 96% identical, while human and rat species (as commonly used in human cardiac research) provided less similarity with 88%.

The alignments also identified that most variances between species occur within the C- terminus; as further confirmed by Uniprot alignment (appendices 2h) where topological, intramembrane and transmembrane regions are highlighted. This shows all transmembrane and pore regions similar, yet shows the C-terminus regions differential.

More so, when creating the equine KCNK3 via mutagenesis; considering time restraints and fact that KCNK3 orthologue alignments suggested less variation between species concerning amino acids 1-250. We decided to produce a C-terminus truncation of KCNK3 was granted. Truncation of the C-terminus reduced the number of differences between human and equine orthologues from 18 to 5, proposing five point mutations were adequate to produce a viable truncated equine TASK-1 orthologue. While truncation additionally increased the identical percentage similarity from 96 to 98%, as also shown in table 4.1.1.1. Further, coloured Clustal Omega alignment as seen in appendices 2i, proves the differences between orthologues to occur individually where single amino acids of similar properties are exchanged.

However, this does not concern amino acids 46, 56 and 183 when comparing human and rat samples; where L E R are presented in place of Q Q H respectively; where amino acids are replaced by those with varying qualities.

Table 4.1.1.1: Table to show the % homology provided by alignment KCNK3 of different species

Alignment between KCNK3 Species		Identities (%)	Appendices number
Human	Equine	96%	2a
Human	Rat	88%	2b
Equine	Rat	90%	2c
Truncated human	Truncated equine	98%	2d

Moving forward, alignment between human and equine KCNK9 orthologues were also conducted, again proving 96% identical similarity, as seen in appendices 2e and demonstrated in table B.

Table 4.1.1.2 also concludes results for both human KCNK3 vs human KCNK9; and equine KCNK3 vs equine KCNK9. This is of interest concerning the binding of heterodimers which will form during the co-expression of TASK-1 with TASK-3 and TASK-1 mutants.

Table 4.1.1.2: Table to show the % homology provided by alignment of human KCNK3 and human KCNK9; and equine KCNK3 and equine KCNK9.

Alignment between …		Identities (%)	Appendices number
Human KCNK9	Horse KCNK9	96%	2e
Human KCNK3	Human KCNK9	59%	2f
Equine KCNK3	Equine KCNK9	56%	2g

Next, genomic browser, Ensembl, was employed conducting a species-specific Basic Local Alignment Search Tool (blast) of the human and equine KCNK3 orthologue sequences against the relevant genome. This identified the location and corresponding KCNK3 nucleotide sequences, upon which primer design was based; designing primers suitable to create accurate and specific mutants of wild type TASK-1, as documented in section 3.1.3.

Blast results proved human KCNK3 to be encoded by chromosome 15, and equine KCNK3 to be encoded by chromosome 2. Despite proving different genomic locus, both orthologues were proven to span two exons; with the first 94.3 codons encrypted at the end of the one exon, and the remaining 1087.6 human, and 1114.6 equine codons at the beginning of the following exon. This suggests that the protein is translated in two parts and processed intercellularly.

In interest obtaining data of maximal validity the equine nucleotide sequence was further processed through IDT databases, optimizing the codon sequence and ensuring that the most effectual sequence would be transfected later in the project. As shown in appendices 3a, optimized and native equine KCNK3 sequences were then aligned to identify were the optimization had occurred. However, this identified no significant differences and so native sequence was employed when designing primers to create equine TASK-1.

4.1.2 Predicted phosphorylation sites within the C-terminus

Due to investigation of the C-terminus truncation, both human and equine C-terminus regions were run through NetPhos 3.1; an in-silico phosphorylation site prediction server. NetPhos3.1 predicts all Serine, Threonine and Tyrosine phosphorylation sites in eukaryotic proteins, identifying the number of sites available to influence the processing, trafficking and membrane expression of TASK-1 and its constructs.

The N250stop cleaved C-terminus of the human orthologue proved to be of 143 amino acids, and as seen in figure 4.1.2.1, contains 27 sites available for phosphorylation. Providing 20 Serine, 4 Threonine and 3 Tyrosine phosphorylation sites – for all of which confidence levels above threshold, as seen in figure 4.1.2.2.

```
    NAEDEKRDAEHRALLTRNGQAGGGGGGGSAHTTDTASSTAAAGGGGFRNV   #     50
    YAEVLHFQSMCSCLWYKSREKLQYSIPMIIPRDLSTSDTCVEQSHSSPGG   #    100
    GGRYSDTPSRRCLCSGAPRSAISSVSTGLHSLSTFRGLMKRRS          #    150
%1  ............................S.....T.SS.............   #     50
%1  Y.......S..S...........YS.........S.S.T....S..S...   #    100
%1  ...YS.T.S.....S....S..SS.S....S.ST........S
```

Figure 4.1.2.1: Figure to display the NetPhos 3.1 in-silico phosphorylation site prediction, concerning the 143 amino acids of the cleaved human TASK-1 C-terminus; identifying 27 potential phosphorylation sites.

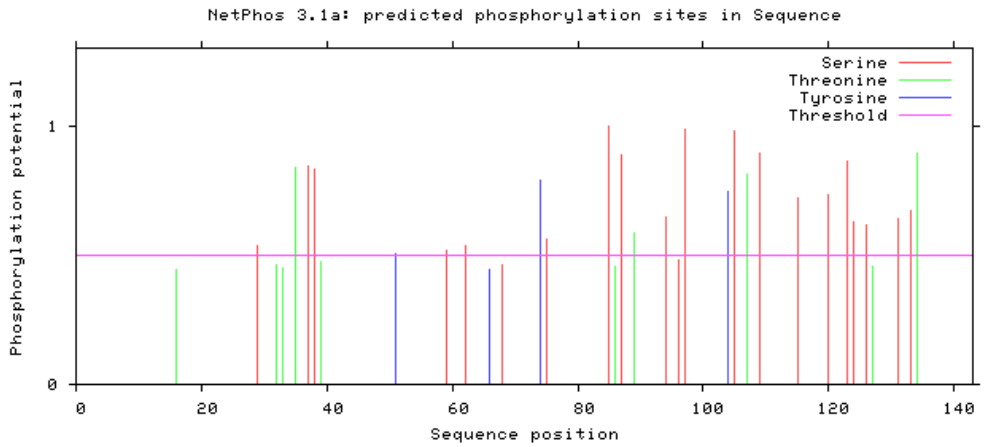

Figure 4.1.2.2: Figure to show the position and probability of the 27 identified potential phosphorylation sites within the 143 amino acids cleaved human TASK-1 C-terminus; as produced by NetPhos 3.1 in-silico phosphorylation site prediction.

The cleaved C-terminus of the equine orthologue evidenced a 154 amino acid sequence, but despite being 11 amino acids longer then the human orthologue, only provided 2 additional phosphorylation sites. As seen in figure 4.1.2.3, the equine C-terminus provided 29 available phosphorylation sites above confidence threshold, illustrated by figure 4.1.2.4. These conclude 21 Serine, 5 Threonine and 3 tyrosine sites for binding.

```
    NAEDEKRDAEHRALLTRNGQAGGACGGGGGGGAGGSAHTTDTASSTVAAG   #
    GGGGGFRNVYAEVLHFQSMCSCLWYKSREKLQYSIPMIIPRDLSTSDTCV   #
    EQSHSSPGGGGRYSDTPSHRCLCSGAQRSAISSVSTGLHSLSTFRGLMKR   #
    RSSV                                                 #
%1  ....................................S.....T.SST....   #
%1  .........Y.......S..S...........YS.........S.S.T..   #
%1  ..S..S......YS.T.S.....S....S..SS.S....S.ST.......   #
%1  .SS.
```

Figure 4.1.2.3: Figure to display the NetPhos 3.1 in-silico phosphorylation site prediction, concerning the 154 amino acids of the cleaved equine TASK-1 C-terminus; identifying 29 potential phosphorylation sites.

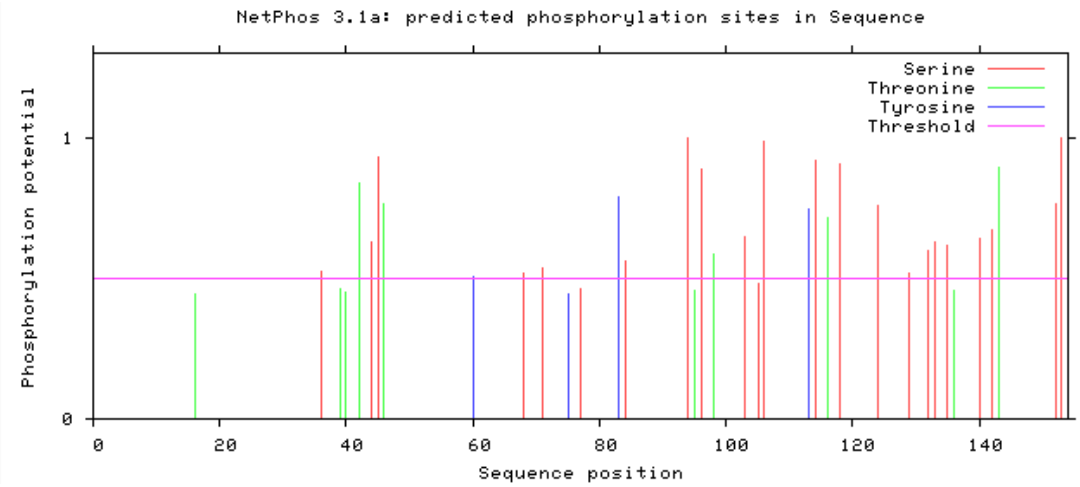

Figure 4.1.2.4: Figure to show the position and probability of the 29 identified potential phosphorylation sites within the 154 amino acids cleaved equine TASK-1 C-terminus; as produced by NetPhos 3.1 in-silico phosphorylation site prediction.

4.2 QuikChange II site-directed DNA mutagenesis

Successful QuickChange site directed mutagenesis allowed for the production of cDNA suitable to transfect: TASK-1_Δ250, C-terminally truncated wildtype; TASK-1_K2N/R3Q high current mutation as modeled in figure 4.2.1; TASK-1_V123L a pathogenic AF mutation as modeled in figure 4.2.2; and TASK-1_-3A>U Kozak mutation in the wildtype TASK-1, effecting protein translation and trafficking.

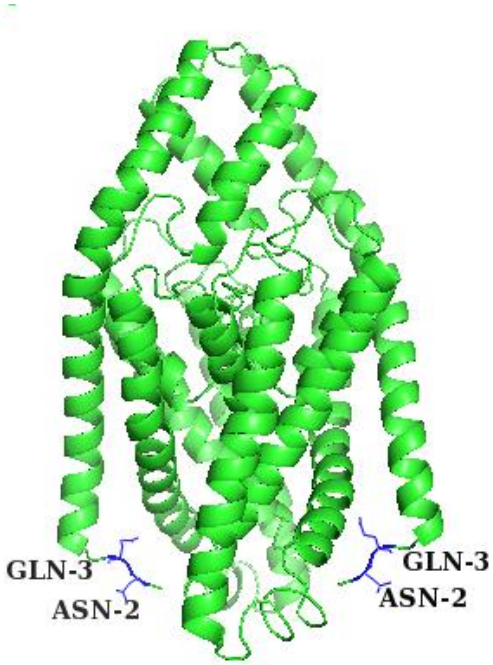

Figure 4.2.1: Model of the enhanced TASK-1_K2N/R3Q protein mutated by inducing a double mutation of the N-terminus, permitting higher currents. Modeled with side view, by use of PyMol; based on a wildtype model donated by Dr. Kevin Cunningham.

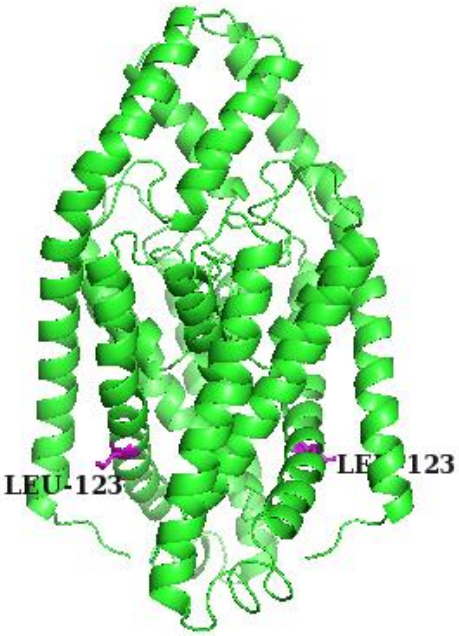

Figure 4.2.2: Model of the proposed loss-of-current protein TASK-1_V123L, as mutated at residue 123 within transmembrane domain 2, disrupting pore formation. Modeled with side view, by use of PyMol; based on a wildtype model donated by Dr. Kevin Cunningham.

4.3 Whole cell patch clamp electrophysiology

Electrophysiological analysis of WT TASK-1 and TASK-3 channels along with TASK-1 mutants was carried out to investigate the effects of mutation on channel function. Further co-expression, allowed examination of any protective ability that heterozygous expression of mutant channels could provide. A whole cell patch clamp technique was employed in conjunction with a step ramp protocol, as described in section 3.4.5. The step component allowed quantification of the difference current between that at -40 mV and that at -80 mV while the ramp component allowed measurement of current over a range of voltages and a measure of the voltage (Vrev) at which the current was 0 pA. All data were collected at physiological pH (7.4) at room temperature.

Both current (pA) and manual cellular capacitance (pF) were noted for each recorded patch and average pA, current density (pA/pF) and reversal potential (Vrev from the current voltage relationship (I/V)) calculated for each data set. Average pA and Vrev were then compared between data groups.

4.3.1 Untransfected controls (ᔓ)

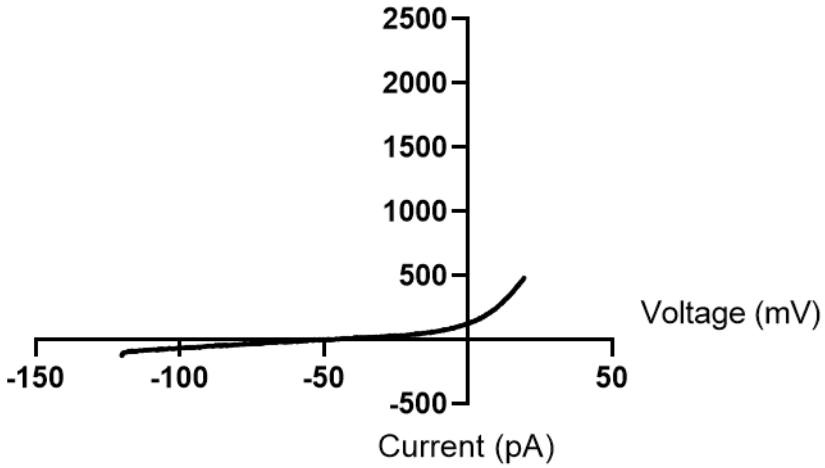

Figure 4.3.1.1: Figure to show the representative current-voltage relationship recorded in untransfected cells. Notice the presence of endogenous outward potassium current at voltages above around -20 mV, but not below.

Untransfected controls were analyzed under full protocol, allowing for the identification of the endogenous currents produced by tsA cells. This can be used to illustrate contamination by the endogenous potassium currents at depolarized voltages, above around -20 mV; but there is little or no endogenous current at voltages between -20 mV and -100 mV, as seen in figure 4.3.1.1.

Because of the presence of endogenous potassium current; currents through recombinant channels were measured between -40 and -80 mV, as this would present a readable difference in the current present. These voltages are close to the resting membrane potential of cells expressing TASK channels, and so are the voltages at which any changes in channel current due to mutation would have most effect on the electrical properties of the cell.

4.3.2 Characterization of Wild type TASK-1 (WT TASK-1) current by use of whole cell patch clamp electrophysiology

Figure 4.3.2.1 shows the representative current voltage relationships for cells expressing WT TASK-1 channels. Whilst, figure 4.3.2.1 shows the current amplitude and reversal potential for untransfected cells compared to cells expressing WT TASK-1 channels.

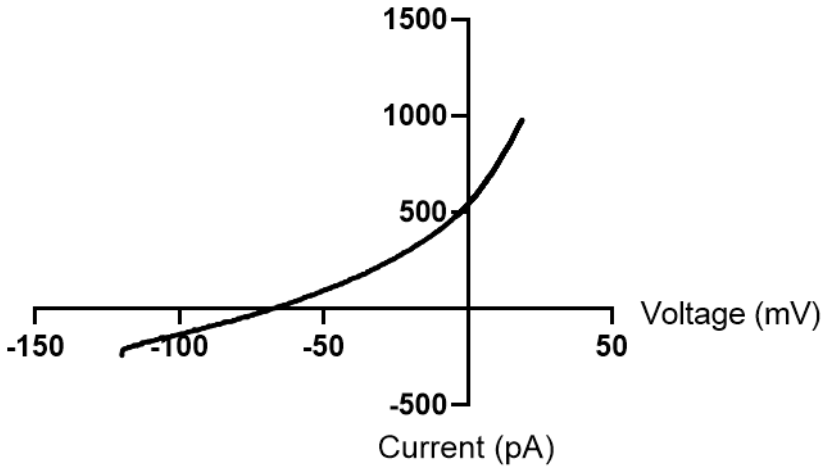

Figure 4.3.2.1: Figure to demonstrate the current voltage relationship produced by WT TASK-1 channels, with voltage (x-axis) plotted against current (y-axis), identifying the voltage reversal potential (Vrev) at which current = 0 and estimating a value of cellular resting membrane potential. Proving WT TASK-1 to have a Vrev of -65mV.

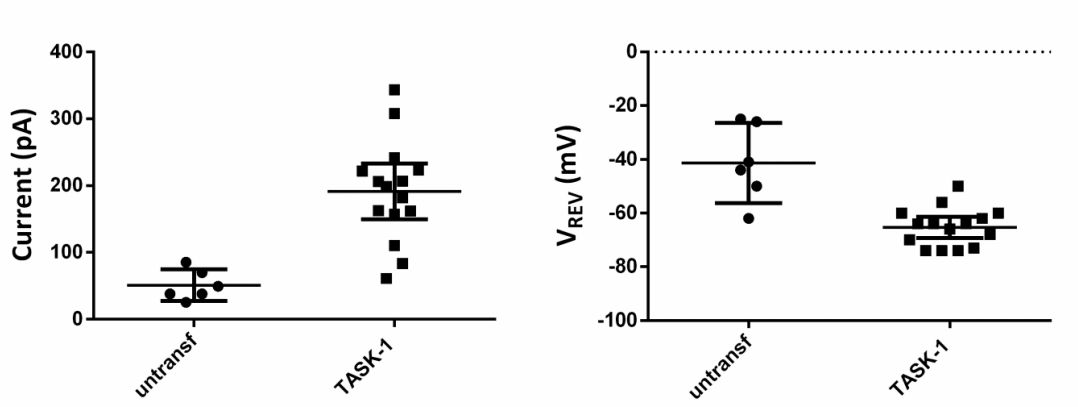

Figure 4.3.2.2: Figure to demonstrate the comparison of currents (left), and reversal potentials (right) obtained for untransfected cells (n=6) and cells expressing WT TASK-1 channels (n=15). Left, identifies data points, ranges and means for current (pA); Right, identifies data points, ranges and means for Vrev (mV).

Current between -40 and -80 mV in cells expressing TASK-1 channels was 191pA [*95% CI: 150 to 233, n=15*] which was significantly larger (*P = 0.0003, [95% CI of difference: -74 to -207*], unpaired t-test) than current in untransfected cells 51pA [*95% CI: 28 to 75, n=6*]. The resting membrane potential in cells expressing TASK-1 channels was -65mV [*95% CI: -61 to -69, n=15*] which was significantly more hyperpolarised (*P = 0.0001, [95% CI of difference: -14 to -34*], unpaired t-test) compared to the resting membrane potential in untransfected cells of -41mV [*95% CI: -26 to -56, n=6*].

4.3.3 Characterization of V123L mutation on TASK-1 ($T1_{V123L}$) current by use of whole cell patch clamp electrophysiology

Substitution of Valine to Leucine at position 123, produced a functional channel, but with a current that was smaller than that seen through WT channels, as seen in figure 4.3.3.1,A-C.

Current between -40 and -80 mV in cells expressing TASK-1_V123L channels was 115pA [*95% CI: 52 to 177, n=6*] which was significantly smaller (*P = 0.04, [95% CI of difference: -4 to -149*], unpaired t-test) than current in WT TASK-1 cells 191pA [*95% CI: 150 to 233, n=15*]. The resting membrane potential in cells expressing TASK-1 channels was -65mV [*95% CI: -61 to -69, n=15*] which was significantly more hyperpolarized (*P = 0.02, [95% CI of difference: 1.7 to 15.5*], unpaired t-test) compared to the resting membrane potential in TASK-1_V123L cells -57mV [*95% CI: -51 to -63, n=6*].

On the other hand, figure 4.3.3.1,D shows that current at +20 mV was not significantly different between the WT and mutated channels; perhaps due to the contaminating presence of endogenous potassium current that the tsA-201 cells present at this potential (Figure 4.3.1.1).

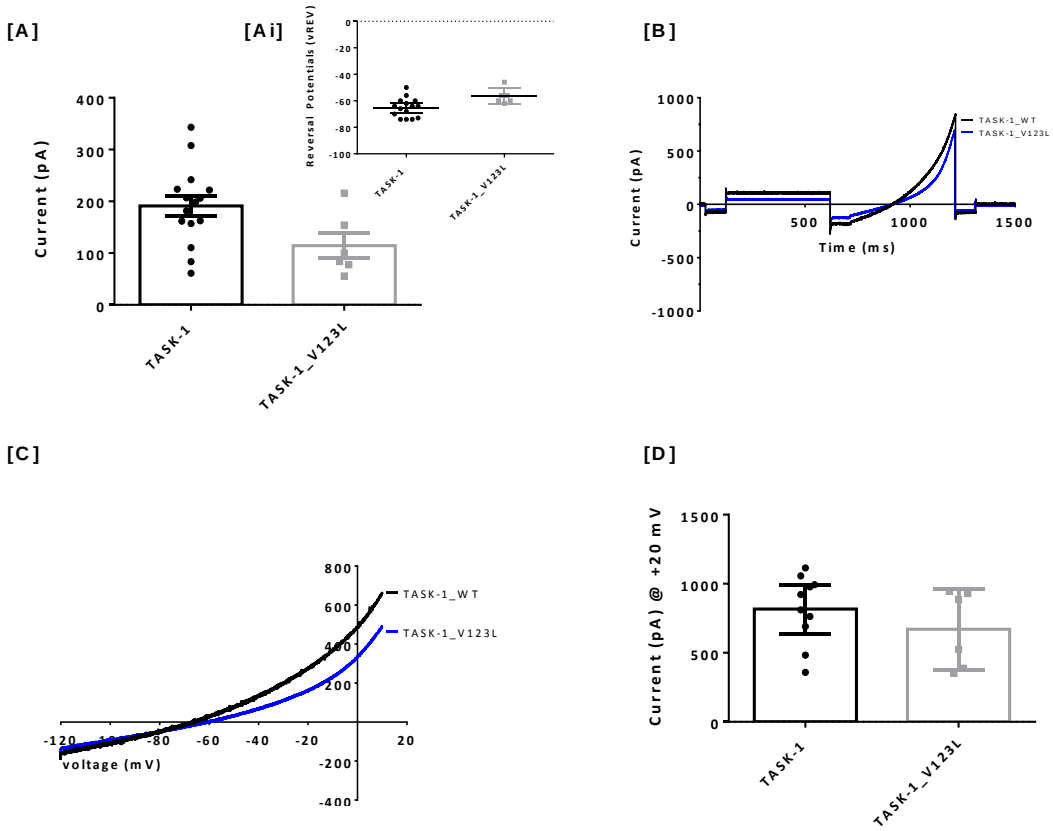

Figure 4.3.3.1: Figure to represent the comparison between WT TASK-1 and TASK-1_V123L channels. A, shows a significantly decreased current from -40 to -80mV concerning WT TASK-1 and TASK-1_V123L, with Ai representing a significantly greater reversal potential concerning TASK-1_V123L; B, illustrates TASK-1_V123L to have a lower peak current and more polarized Vrev as additionally show in C; D, demonstrates no significant difference between WT and mutant currents at +20mV.

4.3.4 Examination of TASK-1 high current mutation K2N/R3Q (TASK-1_K2N/R3Q) by use of whole cell patch clamp electrophysiology

Introduction of the double mutation K2N/R3Q into the N-terminus of TASK-1 - a mutation proposed to facilitate trafficking of TASK-1 channels to the membrane; resulted in a functional channel, as seen in figure 4.3.4.1; yet the amplitude of current through these channels was not significantly different from WT TASK1-1 channels.

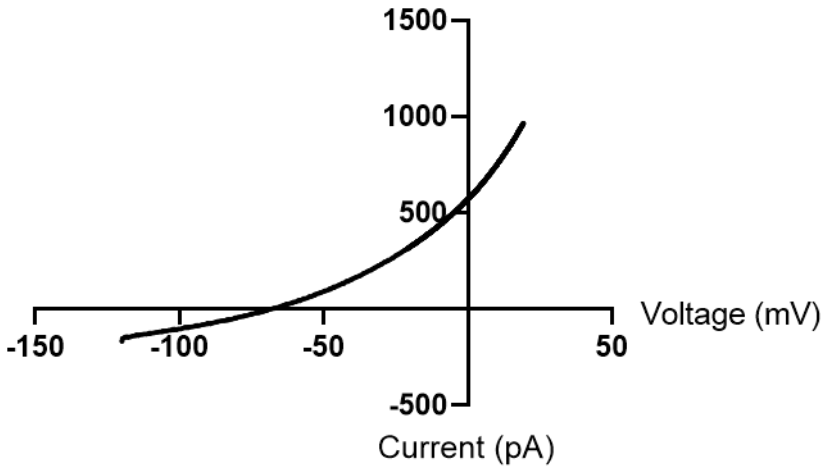

Figure 4.3.4.1: Figure to represent the functional voltage current relationship expressed through K2N/R3Q mutated TASK-1 channels.

4.3.5 Examination of C-terminally truncating TASK-1_K2N/R3Q (TASK-1_Δ250) by use of whole cell patch clamp electrophysiology

The C terminus of TASK-1 was removed at the 250th amino acids residue. This proved increased current amplitude but has no effect on the resting membrane potential (Figures 4.3.5.1 and 4.3.5.2).

Current between -40 and -80 mV in cells expressing TASK-1_K2N/R3Q channels was 197pA [*95% CI: 136 to 259, n=15*] which was significantly smaller (*P = 0.047, [95% CI of difference: 1.2 to 214*], unpaired t-test) than current in TASK-1_K2N/R3Q_ Δ250 cells 305 pA [*95% CI: 200 to 410, n=10*]. The resting membrane potential in cells expressing TASK-1_K2N/R3Q_ Δ250 channels was -63mV [*95% CI: -59 to -67, n=10*] which was not significantly different (*P = 0.433, [95% CI of difference: -3.0 to 6.8*], unpaired t-test) compared to the resting membrane potential in TASK-1_K2N/R3Q cells -65mV [*95% CI: -61 to -68, n=15*].

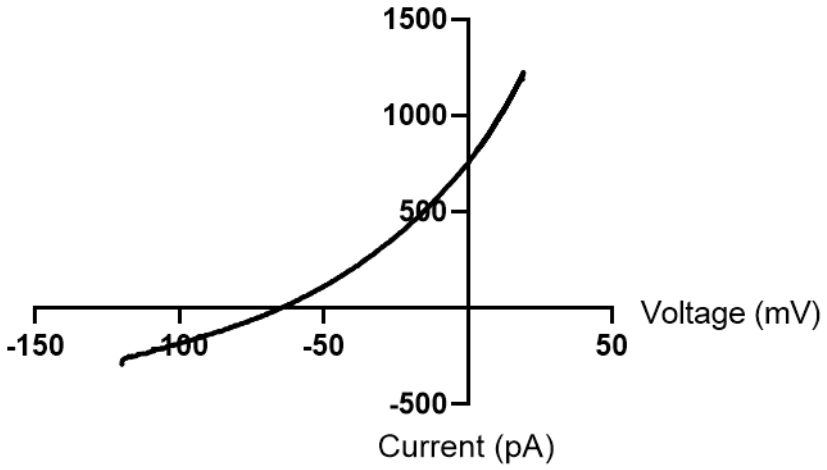

Figure 4.3.5.1: Figure to represent the current against voltage through TASK-1_K2N/R3Q_ Δ250 channels.

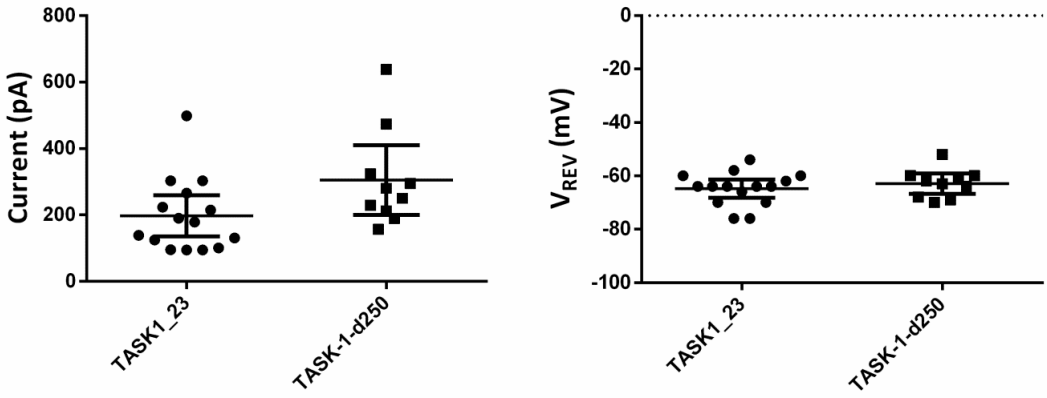

Figure 4.3.5.2: Left, figure to present the significant difference in current through TASK-1_K2N/R3Q (TASK-1_23) and TASK-1_Δ250 (TASK-1_d250). Right, figure to illustrate that no difference in reversal potential was observed concerning TASK-1_K2N/R3Q (TASK-1_23) and TASK-1_Δ250 (TASK-1_d250).

4.3.6 Characterization of Kozak mutation -3A>U on TASK-1_K2N/R3Q (TASK-1_-3A) by use of whole cell patch clamp electrophysiology

Editing of the Kozak region proceeding TASK-1_K2N/R3Q by mutating nucleotide -3 from an Adenine to a Uracil, was proven to edit protein translation, this is demonstrated in figures 4.3.6.1 and 4.3.6.2.

Current between -40 and -80 mV in cells expressing TASK-1_K2N/R3Q channels was 197pA [*95% CI: 136 to 259, n=15*] which was significantly smaller (*P = 0.04, [95% CI of difference: 8 to 236*], unpaired t-test) than current in TASK-1_-3A cells 319pA [*95% CI: 205 to 434, n=11*]. The resting membrane potential in cells expressing TASK-1_-3A channels was -66mV [*95% CI: -63 to -69, n=11*] which was not significantly different (*P = 0.568, [95% CI of difference: -5.9 to 3.3*], unpaired t-

test) compared to the resting membrane potential in TASK-1_K2N/R3Q cells -65mV [*95% CI: -61 to -68, n=15*].

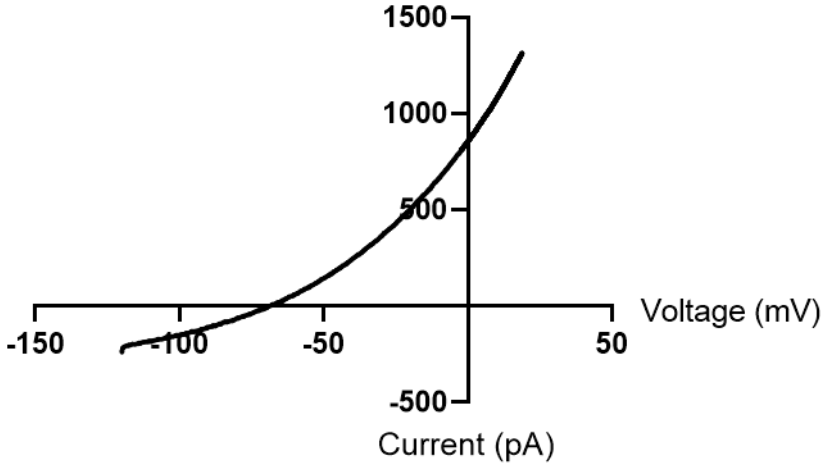

Figure 4.3.6.1: Figure to present the current voltage relationship expressed through TASK-1_K2N/R3Q_ -3A channels.

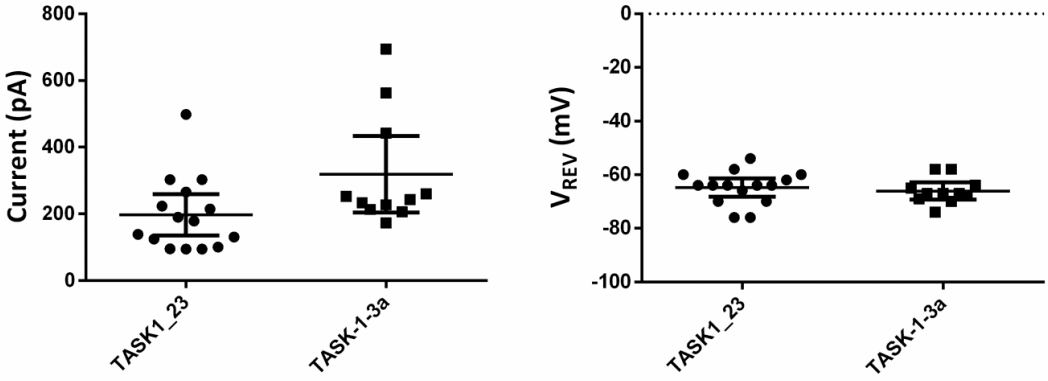

Figure 4.3.6.2: Figures to present the statistical difference between current (left), and similarity concerning Vrev (right) concerning TASK-1_K2N/R3Q (TASK-1_23) and TASK-1_-3A.

4.3.7 Examination of TASK-1 and TASK-1_V123L co-expression by use of whole cell patch clamp electrophysiology

Co-expression of WT TASK-1 channels with TASK-1_V123L channels would be expected to result in a mixed population of homomeric WT, homomeric mutant and heteromeric channels because K_{2P} channels form dimers. The result of this co-expression for current amplitude is seen in figure 4.3.7.1. Interestingly, the current following co-expression is not different to that seen for WT TASK-1 channels. The same profile was seen for the reversal potential (figure 4.3.7.2) This suggests that the properties of the mutant channel are overcome in heteromeric channels.

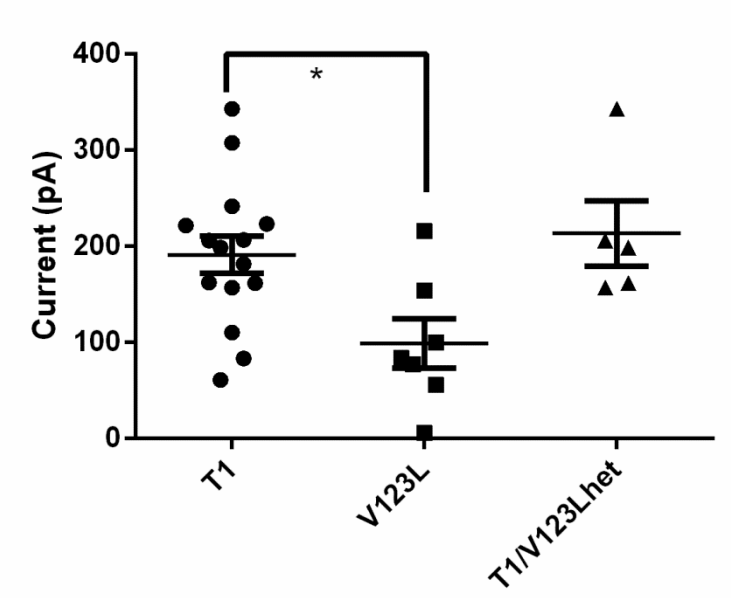

Figure 4.3.7.1: Figure to present the current amplitude following co-expression of TASK-1 plus TASK-1_V123L, with co-expression current showing similar to wildtype. P<0.05 (*), P<0.01 (**), P<0.001 (***) and P< 0.0001 (****).

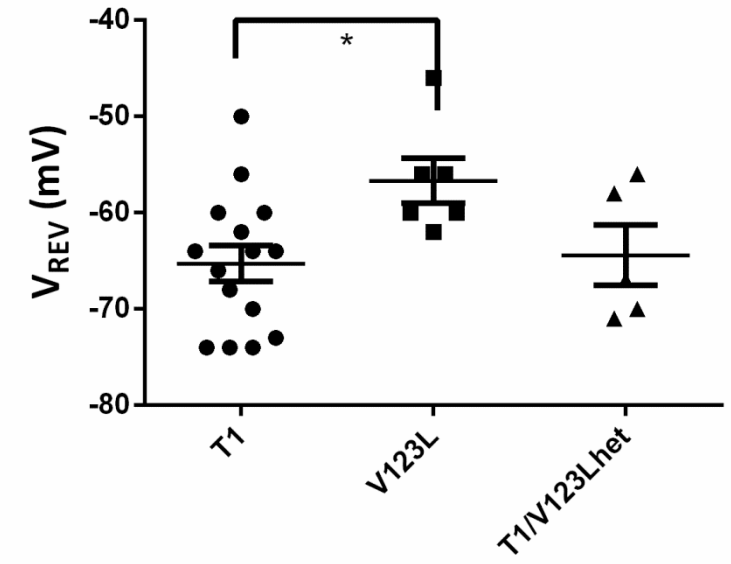

Figure 4.3.7.2: Figure demonstrating the similarity in Vrev of wildtype TASK-1 compared to that obtained after co-expression of TASK-1 plus TASK-1_V123L. P<0.05 (*), P<0.01 (**), P<0.001 (***) and P< 0.0001 (****).

4.3.8 Characterization of Wild type Human TASK-3 (WT TASK-3) current by use of whole cell patch clamp electrophysiology

It was of interest to determine the effect of the mutant channel TASK-1_V123L on TASK-3 channel activity (figure 4.3.8.1) since it is known that TASK-1 and TASK3-channels form heteromers [Bohnen, *et al,* 2017]. Firstly, the properties of WT TASK-3 channels and WT heteromers of TASK-3 and TASK-1 were measured.

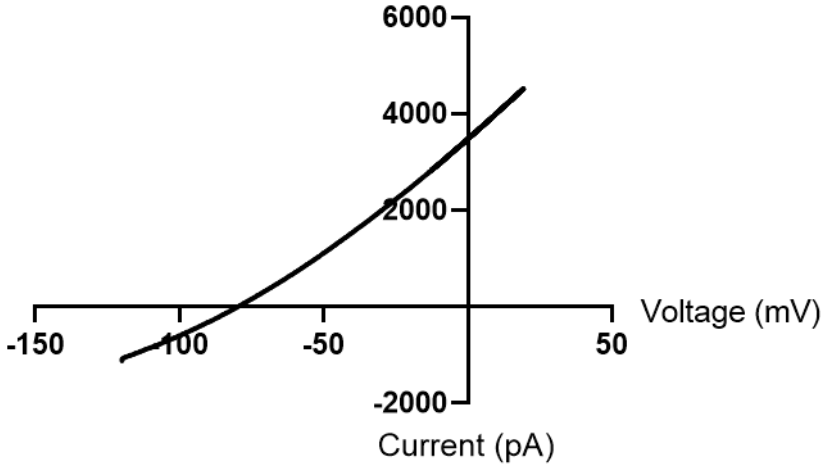

Figure 4.3.8.1: Figure to show the current voltage relationship expressed through WT TASK-3.

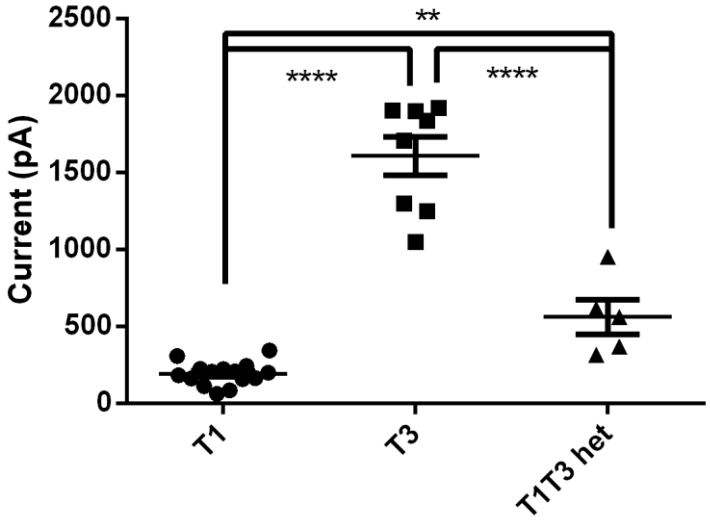

Figure 4.3.8.2: Figure to show the average current amplitudes following co-expression of WT TASK-1 and TASK-3 compared to their homomeric formations. P<0.05 (*), P<0.01 (**), P<0.001 (***) and P< 0.0001 (****).

Current between -40 and -80 mV in cells expressing WT TASK-1 channels was 191pA [*95% CI: 149 to 233, n=15*]. For WT TASK-3 channels this was 1,607pA [*95% CI: 1313 to 1900, n=8*] and for co-expression of both WT TASK-1 and TASK-3 channels this was 562pA [*95% CI: 250 to 874, n=5*]. Each of these values was significantly different from each other, as seen in figure 4.3.8.2, as based on a one-way ANOVA followed by Tukey test. The value obtained for the amplitude of co-expressed channels (562pA) was closer to that of WT TASK-1 channels than WT TASK-3 channels, and lower than what would be calculated for a 50/50 mix of channels (899pA). Indeed, even the upper 95% confidence limit of 874pA is lower than that expected from a 50/50 mix. This suggested that WT TASK-1 channels dominate the amplitude of heteromeric TASK-1 and TASK-3 channels.

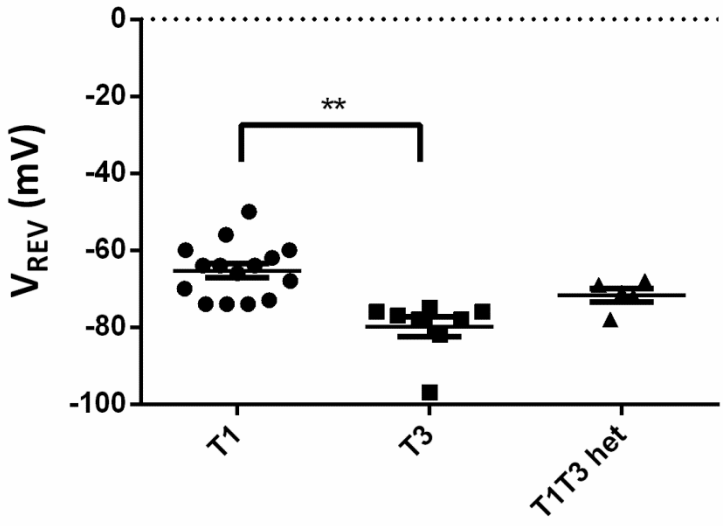

Figure 4.3.8.3: Figure to represent the statistically decreased Vrev of WT TASK-3 compared to TASK-1, and the similarity presented between the Vrev of WT TASK-1and the Vrev following co-expression of WT TASK-1 and TASK-3. P<0.05 (*), P<0.01 (**), P<0.001 (***) and P< 0.0001 (****).

Vrev in cells expressing WT TASK-1 channels was -65mV [*95% CI: -61 to -69, n=15*]. For WT TASK-3 channels this was -80mV [*95% CI: -74 to -86, n=8*], and for co-expression of both WT TASK-1 and TASK-3 channels this was -72mV [*95% CI: -67 to -76, n=5*]. Whilst TASK-1 Vrev was significantly more depolarized that TASK-3, co-expression gave a Vrev not significantly different from either, as shown in figure 4.3.8.3, based on a one-way ANOVA followed by Tukey test.

4.3.9 Examination of TASK-3 and TASK-1_V123L co-expression by use of whole cell patch clamp electrophysiology

Next the properties of WT TASK-3 and TASK-1_V123L channels were measured.

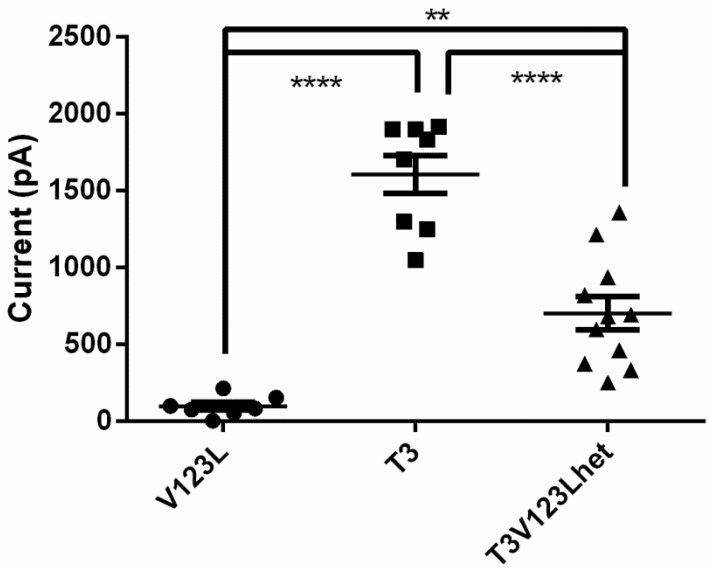

Figure 4.3.9.1: Figure to illustrate the average current amplitudes achieved following co-expression of TASK-1_V123L and WT TASK-3, compared to homodimers. P<0.05 (*), P<0.01 (**), P<0.001 (***) and P< 0.0001 (****).

Current between -40 and -80 mV in cells expressing TASK-1_V123L channels was 99pA [*95% CI: 36 to 162, n=7*]. For WT TASK-3 channels this was 1,607pA [*95% CI: 1313 to 1900, n=8*]. and for co-expression of both TASK-1_V123L and TASK-3 channels this was 704pA [*95% CI: 463 to 943, n=11*]. Each of these values was significantly different from each other (see figure 4.3.9.1, one-way ANOVA followed by Tukey test). In contrast to the data for WT TASK-1 in figure 4.3.8.3, the value obtained for the amplitude of co-expressed channels was about half way between that of TASK-1_V123L channels and WT TASK-3 channels and the range of 95% confidence intervals (463-943) encompassed the value that would be calculated for a 50/50 mix of channels (853pA). This suggested that TASK-1_V123L channels do not dominate the amplitude of heteromeric TASK-1 and TASK-3 channels.

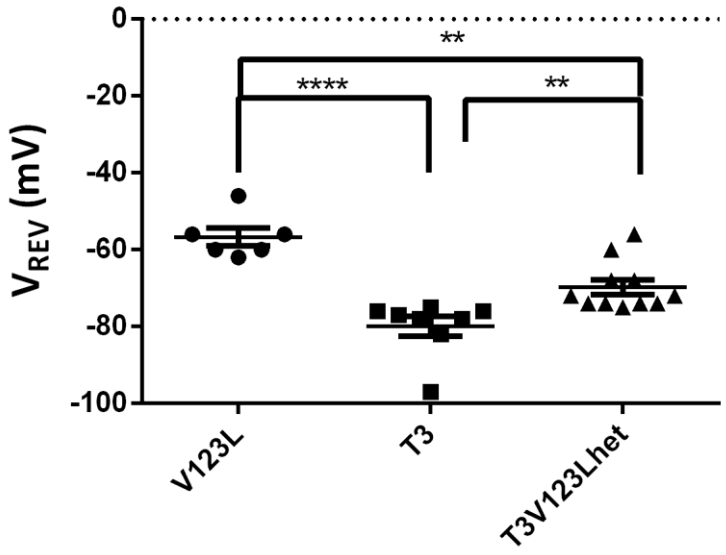

Figure 4.3.9.2: Figure to show the statistically different Vrev's created following co-expression of TASK-1_V123L and WT TASK-3, compared to homodimers. P<0.05 (*), P<0.01 (**), P<0.001 (***) and P< 0.0001 (****).

Vrev in cells expressing TASK-1_V123L channels was -57mV [95% CI: -51 to -63, n=6]. For WT TASK-3 channels this was -80mV [95% CI: -74 to -86, n=8] and for co-expression of both TASK-1_V123L and TASK-3 channels this was -70mV [95% CI: -65 to -74, n=11]. Each of these values was significantly different from each other, as shown in 4.3.9.2, based on a one-way ANOVA followed by Tukey test.

4.4 Confocal Microscopy

In interest of visually assessing whether the TASK-1 constructs had influenced the trafficking or expression of TASK-1; confocal microscopy was utilized to identify differences in membrane expression and protein localization from wildtype.

Slide were made for TASK-1_K2N/R3Q and TASK-1_-3A, due as these were built in the pAcGFP1-N1 vectors, necessary to attach a GFP the C-terminus of the channel monomers. Permitting for higher expression levels to be represented by greater green florescence; and the spread of florescence to represent channel localization.

4.4.1 Controls

To begin, as seen in figure 4.4.1.1, controls images were taken from cells to eliminate visual contamination, and identify any possible modifying interacts between the stains and proteins used. Results are illustrated in grids where rows demonstrate different channel types; and columns represent different laser types and wavelengths, where; a, imaged using the diode-pumped solid state (DPSS) laser (650nm Ex/655nm EM) to locate CMR membrane stains; b, imaged using an argon 488nm laser line (495nm Ex/519nm Em) to locate GFP protein tags; and c, provided the use of both lasers, creating an overlapped image; identifying expression in correspondences to the membrane.

Controls shows that when expressed alone GFP has no selected localization site or trafficking process, as illustrated by the florescence of the whole cellular cytosol in figures 4.4.1.1; Ab and Ac, so will have no effect on the protein to which it is attached.

Figure 4.4.3.1; Ba additionally proves that the CMR membrane stain is fully membrane selective and associates at no other region with in the cell. Figures 4.4.1.1; Bb and Bc, further show that CMR has no interaction with GFP, with GFP expression proving concurrent with figure 4.4.1.1; Ac (where CMR is not utilized) and additionally, CMR is only present in the membrane region, figure 4.4.1.1; Bc.

Figure 4.4.1.1 rows C and D, then present the TASK-1 mutations in an absence of CMR, with fluorescence only present at the membrane. When compared to results figure 4.4.2.1; rows B and C (where the constructs are expressed in the presence of CMR), no difference in localization is presented, concluding that CMR has no functional interaction with the proteins expressed and does not affect the trafficking or localization of these.

Finally, untransfected controls were run, as seen in results figure 4.4.2.1; a, b and c, which when compared to all transfected cells (all mother figures) proves that the TurboFect transfection reagent has no effect on the membrane structure, and fails to impair the function of the CMR stain.

Successful, conduction of all control images therefore showed that no stain, label or reagent has any effect, or influence on any other stain or label. Whilst further the absence of any overlap in fluorescence between any image in column a and column b; suggests that the differential wavelengths used to excite the stains and

labels crates no overlap in fluorescence that might create interference; preventing the collection of false or contaminated images.

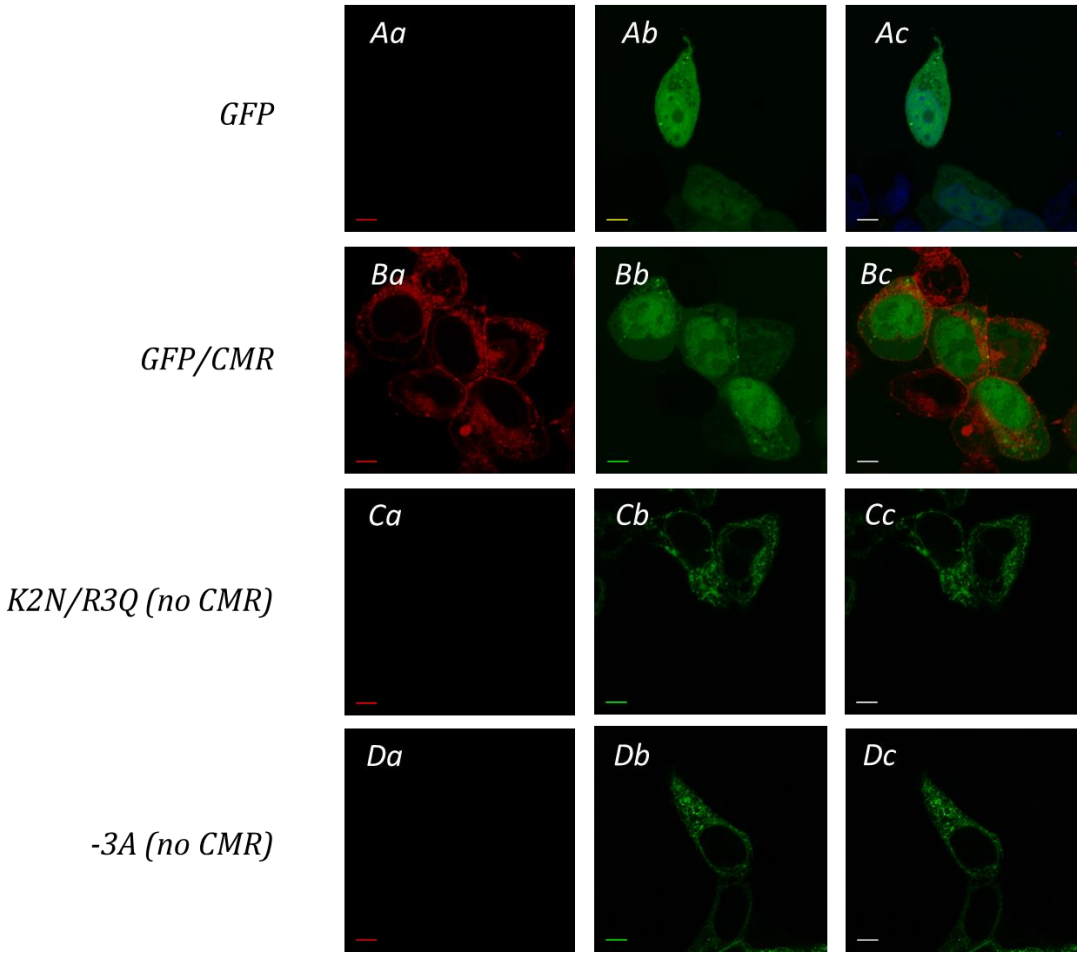

Figure 4.4.1.1: Figure to demonstrate the control slides produced, where row A, GFP; B, GFP/CMR; C, TASK-1_K2N/R3Q in the absence of CMR; D, TASK-1_-3A in the absence of CMR. Whilst column a, imaged using the Helium-neon laser (650nm Ex/655nm EM) to locate CMR membrane stains; b, imaged using an argon 488nm laser line (495nm Ex/519nm Em) to locate GFP protein tags; and c, provided the use of both lasers, creating an overlapped image; identifying expression in correspondences to the membrane.

4.4.2 Results

Following controls, and based upon the increased TASK-1_-3A current produced and the unexpected similarity of TASK-1_K2N/R3Q current to wildtype. It was necessary to run confocal microscopy, to identify if the TASK-1_-3A currents were larger due to increased expression; and if the lack of difference between TASK-1_K2N/R3Q and wildtype was due to increase channel action but less expression, or equal expression but no variation in channel function.

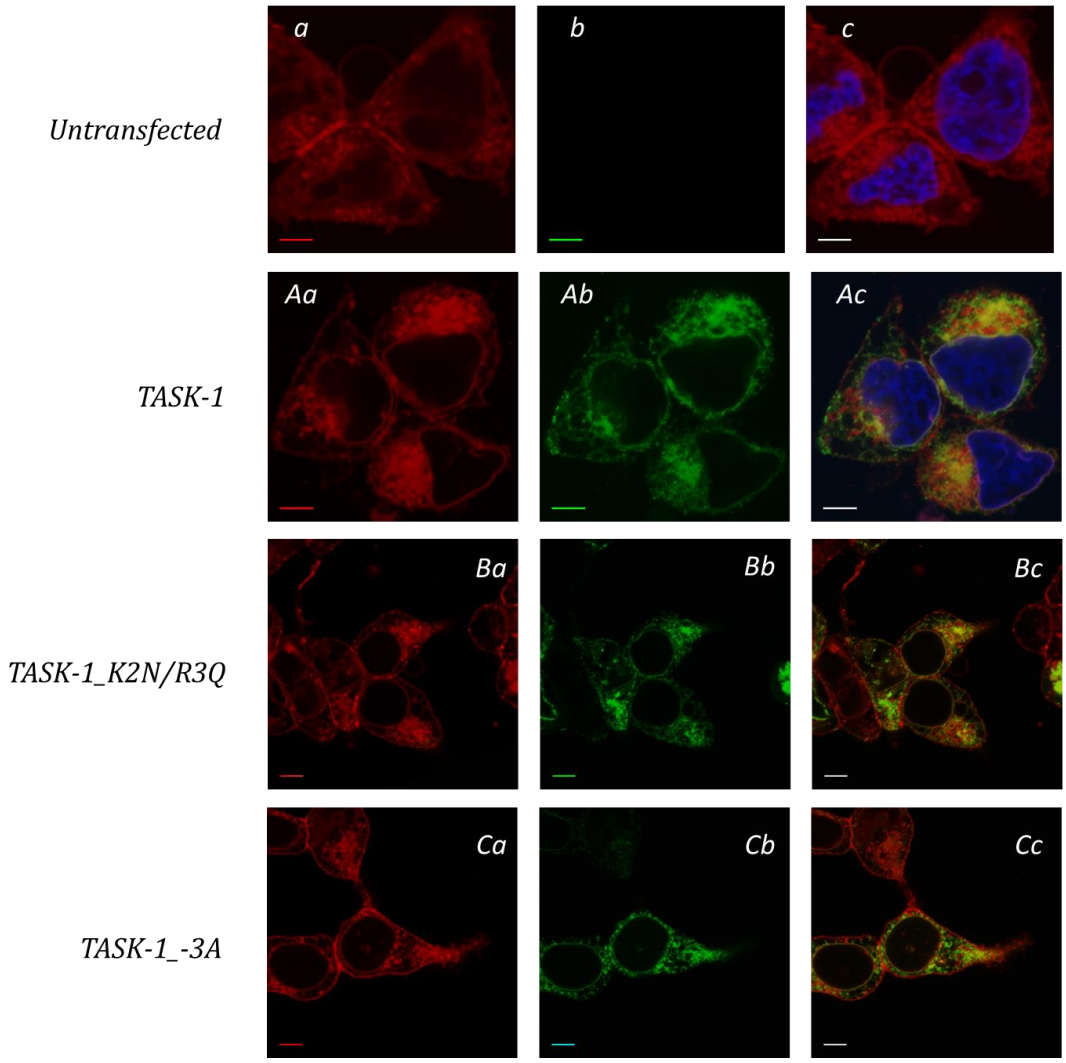

Figure 4.4.2.1: Figure to demonstrate the result slides obtained, where row a, untranfected cells; A, TASK-1 wildtype; B, TASK-1_K2N/R3Q; C, TASK-1_-3A. Whilst column a, imaged using the Helium-neon laser (650nm Ex/655nm EM) to locate CMR membrane stains; b, imaged using an argon 488nm laser line (495nm Ex/519nm Em) to locate GFP protein tags; and c, provided the use of both lasers, creating an overlapped image; identifying expression in correspondences to the membrane.

By visual comparison of figures 4.4.2.1; Ac, Bc and Cc, it is evident that WT TASK-1, TASK-1_K2N/R3Q and TASK-1_-3A all localize on the cell membrane with an even distribution, as illustrated by the clear overlap (yellow) presented in each image. This shows that both K2N/R3Q and -3A mutations fail to adapt the cellular region of channel localization.

Further, comparison of figures 4.4.2.1; Ab, Bb and Cb, demonstrates that the expression of protein is proportionally consistent throughout the TASK-1 constructs, with the degree of fluorescence within these images failing to produce any difference concerning expression levels; as do images 4.4.2.1; Ac, Bc and Cc. This suggests that the expression of the K2N/R3Q and -3A mutants is equal to that of wildtype, however further tests to quantify the fluoresce presented would need to be conducted in order to confirm this.

5 Discussion

To fulfill the purpose of this investigation and further characterize human TASK-1 channels in atrial fibrillation (AF), TASK-1 channels underwent mutational manipulation editing the structure of the encoding gene, building the desired variants for analysis. These were transfected into tsA-201 cells, which translated and expressed the protein on the membrane surface. The channels were then exposed to whole cell patch clamp electrophysiology, analyzing the channel currents produced; and confocal microscopy, identifying differences in channel expression and localization.

TASK-1 is encoded by the KCNK3 gene [Gierten, et al, 2010], and analogues of this gene are found within the human and equine genomes at chromosomes 2 and 15, respectively. A protein of 394 amino acids is produced in human cells (appendices 1a), and a longer 403 amino acid protein is translated in equines (appendices 1b). These two analogues provide 96% identical homology (appendices 2a), the similarity between human and equine KCNK3 increases to 98% concerning a C-terminus truncation; whilst full human and rat KCNK3 (as commonly used in the AF research) only comply 88% identical homology, table 4.1.1.1.

However, mutagenesis proved difficult when inducing the equine orthologue and second Kozak mutations, due to the primer designs that were dictated by the native TASK-1 sequence. These provided high GC contents and resulted in a dysfunctional PCR or digestion, additionally preventing viable cultures from establishing on the selective Kanamycin Plates. In order to optimize PCR, Taq-polymerases and quick solution were changed for new batches and PCR reagents were reconstituted. Further, the annealing temperatures (Tm) of the reactions were adjusted either way of the Tm's recommended by Eurofins, yet PCR still proved dysfunctional. This left only the high GC content primers to be fault, as selected mutations with lower GC content primers were functional and obtained quality sequencing results, also proving the chosen plasmid utilized in mutagenesis was of functional quality.

Concerning the electrophysiological analysis of channel currents an enhanced wildtype (TASK-1_K2N/R3Q) was additionally made. Primers were designed to introduce two high current mutations, K2N and R3Q, into the N-terminus of Wildtype TASK-1 (as seen in figure 4.2.1). These were created to provide a larger current, exaggerating any effect that further mutations might have in current amplitude compared to the wildtype. Primers for this were kindly donated by Dr. Emma Veale and functioned to mutate the KR retention signal of the TASK-1 N-terminus, to NQ. This in turn, prevented the binding of a protein called COP1, which is located within the intracellular endoplasmic reticulum (ER). During protein processing, COP1 binds to the TASK-1 C- terminus, or to the N-terminus at positions 2 and 3 which induces protein retention within the ER. This decreases protein surface expression hence reducing current. However, after K2N/R3Q mutation, COP1 is unable to bind and the TASK-1 protein can be translocated to the membrane where it free to dimerize and function – increasing current due to greater surface expression [Lee, 2018].

The current voltage relationship for TASK-1_K2N/R3Q can be seen in figure 4.3.4.1, however when a statistical comparison between WT TASK-1 and TASK-1_ K2N/R3Q was conducted by unpaired t-test, no significance difference was presented. Additionally, confocal microscopy showed protein localized at the membrane with even distribution, however visually the florescence of this cannot be quantified by eye, yet no obvious difference is presented between WT TASK-1 and TASK-1_K2N/R3Q, as illustrated in figure 4.4.2.1.

More so, to investigate the influence of phosphorylation on the C-terminus of TASK-1 a C-terminal truncation (TASK-1_Δ250) was created. This would identify any differences in protein processing or trafficking compared to wildtype, and like the high current mutation, C-terminus cleavage was predicted to increase protein expression by preventing ER retention. However, the effect of a C-terminus truncation was proposed to be larger due to the TASK-1 C-terminus containing 27 phosphorylation sites which can affect the proteins processing and expression, as seen in figure 4.1.4.2.

For example, Phosphorylation of Thr383, is proven to inhibit TASK-1 function inducing atrial fibrillation [Harleton, *et al,* 2015/ Arakel, *et al,* 2014], due to an inhibition by COP1 mediated retention within the ER, as mentioned concerning mutation K2N/R3Q. This prevents the channels transport to the cell membrane where it can be employed.

This effect is further aided by the last three amino acids of the TASK-1 C-terminus - the SSV complex. These amino acids prove critical in TASK-1 expression by providing binding sites for protein 14.3.3, which phosphorylates the protein preventing COP1 interactions. Moreover, C-terminal 14.3.3 phosphorylation additionally inhibits COP1 binding to the TASK-1 N-terminus and so is considered to forward protein expression.

P11 is another protein that functions in the same manner as 14.3.3, however needs 14.3.3 to aid its interaction with the terminus [Enyedi et al, 2010], yet a C-terminus truncation of the TASK-1_K2N/R3Q would remove all 27 phosphorylation sites including those of 14.3.3; potentially allowing for other ER retention sites with the main body of the protein to then function with greater effect.

Truncation of the C-terminus was designed leaving the VLRFLT region attached to the cytosolic side of the TM4; insuring that proteins were created in a functional structure, as this halothane response element plays a function role as a signal transducer to the gate [Mathie and Veale, 2010].

As seen figures, 4.3.5.1 and 4.3.5.2; the removal of the C-terminus resulted in a larger current amplitude (305pA) compared that of the TASK-1_K2N/R3Q wildtype (197pA), but presented no significant difference in reversal potential ((Vrev) the voltage at which current = 0), with a Vrev of -63mV for the truncation (TASK-1_K2N/R3Q_ Δ250) and -65mV for the wildtype (TASK-1_K2N/R3Q).

This suggests that the removal of the COP1 binding sites prevents TASK-1 retention in the ER, allowing greater TASK-1 membrane expression, as

represented by an increase in current. However, this comparison provided P value of 0.46, with p<0.5 being considered significant. Proving that the current observed where significantly different, but the current increase was not massive.

TASK-1 is predominately expressed within the atria of the heart, where it plays a role in the repolarization of the cardiomyocytes following the creation of an action potential. TASK-1 is active in this role by conducting continuous potassium efflux across all voltages and so reduces the electrical potential of the cardiomyocyte. This contributes to the resting membrane potential of -90mV - dictated by TASK-1 function and the equilibrium constant of potassium (-90mV). However, based upon the activity and membrane expression of the TASK-1 channel this resting membrane potential can differ and lead to chronological effects on the action potential duration (APD) experienced in cardiac cells. Differencing the action potential duration then allows for the occurrence of pathophysiological effects, such as early afterdepolarization which contribute to the loss of electrical synchronization of the heart and induce atrial fibrillation.

Based on the idea that the current amplitude of channels could be increased due to expression levels, and the fact that TASK_1 is predominately expressed in the atria; Kozak mutation -3A>U was created. As described in section 1.6.2, this TASK-1 Kozak mutation, had been identified as part of a dual mutation within a patient with AF, but had not been investigated individually. The mutation occurs 3 bases upstream of the AUG start codon of KCNK3 and is sat in prime position to dominate the ribosomal translation of the KCNK3 gene. As a dual mutant, the difference in Kozak region had presented a 40% reduced luciferase fluoresces, indicating a lack of protein expression on the membrane, and predicting a reduced TASK-1 density of 50% [Liang, *et al,* 2014].

Editing the Kozak region proceeding the TASK-1_K2N/R3Q (by mutating nucleotide -3 from an Adenine to a Uracil) significantly increased current to 319pA (TASK-1_-3A), compared to wildtype 197pA (TASK-1_K2N/R3Q), proving mutation -3A<U to edit protein translation, but not to effect Vrev - with TASK-1_K2N/R3Q and TASK-1_-3A producing Vrev values of -65mV and -66mV, respectively.

This current increase gave significant p value of 0.04, proving the difference in current amplitudes observed was distinct, and that the functional increase of TASK-1_-3A is constant. This contradicted the perception of the mutant's action, and inversely increased current, hence indicating increased translation. This could be repercussive of the mutation changing the -3 nucleotide from an Adenine to a Uracil; matching the -3 base in the optimal Kozak consensus sequence; CRCCAUGG (R = purine, A or G) [Acevedo, *et al,* 2018]. For this reason, TASK-1_3A underwent confocal microscopy to identify expression changes, as seen in figure 4.4.2.1.

However, confocal microscopy shows no obvious visual increase in protein expression despite there being a statistical increase in current concerning the -3A>U Kozak mutation. This could be due to the mutation inducing the proteins function in a different way, or could prove that the confocal machine is a technique

not sensitive enough to detect the small difference in expression level; based upon the fact there is a less than 2-fold increase in current (122pA) concerning the mutation when compared to TASK-1_K2N/R3Q. Further, it is possible that both TASK-1_K2N/R3Q and TASK-1_-3A were over expressed in this system, making the small difference hard to view based on the abundance of fluorescence that is presented. This suggests that further quantification of the experiment would be needed in order to conclude if the protein induced any greater expression, and in cell/on cell Weston's may be used to further identify the trafficking processes of the protein, or smaller DNA transfection quantities could be used; reducing the overall florescence, leave the small difference in florescence exaggerated.

Moving on V123L is another mutation said to create a loss of TASK-1 function. This replaces a Valine with a Leucine at position 123 within the second transmembrane domain of the TASK-1 monomer. Upon dimerization, V123L then prevents the formation of a stable pore structure based upon the different bonding properties of the two amino acid residues, eliminating a structural van-der-Waals attraction with Leucine 11 of transmembrane domain 1. This results in a significantly lower current amplitude of 115pA compared to that of a wildtype channel (191pA); in addition to a significantly hyperpolarized reversal potential (Vrev) of -57mV, compared to that of wildtype (-65mV), as seen in figures 4.3.3.1,A-C.

This concurs with the work of Liang, *et al,* 2014 (conducted by a different protocol), in the respect that a significantly reduced current was produced along with a significently increased Vrev for TASK-1_V123L. However, our works contrasted as Liang describes a total loss of current through the TASK-1_V123L channel, where as we found small yet present current (115pA), despite being 60.2% reduced compared to WT TASK-1.

In interest of rectifying this contrast, currents at +20mV, as used by Liang, were then calculated, and an unpaired t-test used to comapre +20mV currents for WT TASK-1 and TASK-1_V123L. However, as demonstrated in figure 4.3.3.1,D, this comaprison provided no significant difference, yet this could be due to the endogenous K_v currents presented by the tsA-102 cells used to host the channels. These endogenous tsA-201 currents are maximised at +20mV (figure 4.3.1.1) and so may have maksed the loss of $K_{2P}3.1$.

In regard to the hyperpolarized resting potential of TASK-1_V123L, this has been shown to increase by 12% (+8mV), in our tsA-201 cells, and 35% (20mV) in CHO-K1 cells [Liang, *et al,* 2014]. This translates to reduced number of potassium ions needed to be extracellularly expelled before the resting membrane potential is reached, and therefore results in a shortened APD. Within the cardiomyocytes of a perspective homozygous V123L mutated patient, this would lead to the induction of AF based upon the fact that the natural rate of SAN fire would be increased, and the dromotropy be amplified, decreasing APD <200ms [Franz, 2012].

However, within native atrial tissue of heterogynous patient's WT TASK-1 and TASK-1_V123L would be naturally co-expressed. Investigation of this co-expression results in the formation of 3 dimer channel types; WT TASK-1

homodimers, WT TASK-1/TASK-1_V123L heterodimers and TASK-1_V123L homodimers. Based on natural protein processing, it is assumed that formation of the dimers would prove 25%, 50% and 25% respectively.

Considering TASK-1_V123L provided significantly less current amplitude then WT TASK-1 with a more depolarized Vrev. As seen in figure 4.3.7.1, the current obtained by co-expression of WT TASK-1 and TASK-1_V123L proved no statistical difference to that seen for WT TASK-1 alone. The same profile was illustrated for the reversal potential, as in figure 4.3.7.2. This suggests that the properties of the V123L mutant are overcome by formation of heteromeric channels.

This heterodimeric recovery of function could be induced, by the WT TASK-1 α-subunit, acting as a scaffold to hold the mutated V123L α-subunit in place; forcing the second transmembrane domain into a conventional formation despite its lack of stability.

This is suggested, as another V>L KCNK3 mutation (V221L) which affects the second pore forming loop, has proven a loss of function in homomeric formation and additionally in WT/V221 heteromeric formation [Bohnen, et al, 2017]. However, the pore region cannot be restricted in position between the transmembrane domains. So, could induce a greater conformational change then V123L within the TM2.

Moreover, in native tissues TASK-1 additionally dimerizes with TASK-3, and expression of TASK-1/TASK-3 heterodimers has been observed on the cardiomyocyte membranes of the human right arterioles [Enyedi et al, 2010]. Heterodimer formation between TASK-1 and TASK-3 is aided by their molecular similarity (60% homologous), presenting highly related transmembrane segments, pore regions, and extracellular loops. This further, induces equal expression of both homo- and heterodimers in native tissues, where if the ratio of expression is appropriate, TASK-1 and TASK-3 heterodimers are assembled in equal efficiency to the homomeric channels [Enyedi et al, 2010].

To continue the investigation of TASK-1_V123L in native heteromers, I first had to study the amplitude and Vrev for TASK-3; and TASK-3 and WT TASK-1 co-expression.

As demonstrated in figure 4.3.8.2, WT TASK-3 channels gave an average current of 1,607pA, and the co-expression of both WT TASK-1 and TASK-3 channels gave current of 562pA. Compared to the WT TASK-1 current of 191pA, these currents all prove significantly different from each other based on a one-way ANOVA followed by Tukey test.

However, the current value obtained for the co-expressed channels (562pA) was closer to that of WT TASK-1 than WT TASK-3, and further was less than the 899pA value calculated for a 50/50 mix of channels. More so, even the upper 95% confidence limit of 874pA proved lower than the current expected from a 50/50 (899pA) mix. This suggested that WT TASK-1 channels dominate the amplitude of heteromeric TASK-1/TASK-3 channels.

Further, as seen if figure 4.3.8.3, the Vrev for co-expression of both WT TASK-1 and TASK-3 channels was -72mV. However, this failed to prove significant in difference compare to WT TASK-1 (-65mV), or WT TASK-3 channels (-80mV). Proving that TASK-1 may dominate the current amplitude but both channels effect Vrev equally.

However, concerning the co-expression of TASK-3 with TASK-1_V123L, as seen in figure 4.3.9.1. Co-expression of both TASK-1_V123L and TASK-3 channels induced current of 704pA, compared to the 99pA for TASK-1_V123L channels, and 1,607pA for WT TASK-3. Each of these values proved significantly different from each other (see figure 4.3.9.1). In contrast to the data for WT TASK-1 and WT TASK-3 co-expression (figure 4.8.3.2); the current amplitude of co-expressed WT TASK-3 and TASK-1_V123L channels proved midway between that of TASK-1_V123L homodimers and WT TASK-3 homodimers, with the range of 95% confidence intervals (463-943) encompassing the value calculated for a 50/50 mix of channels (853pA). This suggested that TASK-1_V123L channels do not dominate the amplitude of heteromeric TASK-1/TASK-3 channels.

Further, co-expression of both TASK-1_V123L and TASK-3 channels, as seen in figure 4.3.9.2, gave a Vrev value of -70mV, which after a one-way ANOVA followed by a Tukey test, proved significantly different from the Vrev values obtained for both WT TASK-3 (-80mV), and TASK-1_V123L (-57mV). This suggests the dominance concerning WT TASK-1 in a heteromer, is lost upon V123L mutation, as mutual expected values were obtained concerning TASK-3 and TASK-1_V123L co-expression, with no dominance shown from either channel.

Returning to the proposition of a heterozygous patient, based on the current data collected, the co-expression experiments have shown, that a TASK-1_V123L mutation could be carried by a patient yet the expression of WT TASK-1 or WT TASK-3, could counter act the loss of current that TASK-1_V123L demonstrated. Further, heteromers would form naturally and resuscitate the depolarized reversal potential of the TASK-1_V123L, returning the APD to a normal range (200-400ms), and reducing the potential of AF onset [Franz, 2012].

In addition, the retrieval of Vrev by TASK-3/TASK-1_V123L co-expression could further explain why V123L has not been identified in diseases relating to somatic cells. There is strong evidence to suggest that TASK-1 channels are involved in apoptosis roles and pathogenically influence oncological factors leading to cancer [Leithner, *et al,* 2016], yet this mutation has not been identified in any other pathological state apart from AF, where TASK-3 expression is limited.

However, even in the presence of WT task-1 and WT TASK-3, possible de novo events that could reduce TASK-1 protein expression, would still put the patient at risk if expression levels were to become unbalanced; and as with any genetic factor, all offspring would be at risk of acquiring the mutation which could prove pathogenic in homozygotes.

The data presented here is based upon the currents produced by each channel type and co-expression, yet possible shifts in trend may be shown if data was calculated in a normalized fashion, calculating the cell density. Comparison of this would allow for cell size to be taken into consideration concerning the current produced; and allow for a greater examination of the current through each channel on the membrane surface. However, for this to occur greater n numbers are desired concerning each channel type; as the small current differences between channel types, induces difficultly in quantifying if there is any significant difference or not. Controversially, the calculation of the reversal potentials concerning each channel type would be unchanged, and still present the same comparisons between Vrev.

Further, in pursuit of accurate data concerning the small currents; only the best quality data was included. Concerning the electrophysiological recordings, only patches with a good access resistance were included ensuring the cell membrane and the micropipette formed good unity and there was no interference from a weak seal. This was identified by a patch presenting currents above 0pA at the holding potential of the protocol (-60mV); and currents of >200pA upon application of -40mV. This was a very applicable factor, when carrying out the patch clamp electrophysiology of TASK-1 and TASK-1_V123L; as the cells proved to obtain weak membranes, producing fragile seals. This led to an adaption in patching technique varying the amount of negative pressure applied once a seal was obtained; and concerning TASK-1_V123L once a seal was formed, a small current shock was utilized to break the membrane as opposed to further negative pressure. Additionally, pipettes of varying resistances were pulled for different channels, as sharper electrodes help achieve better seals with TASK-1_V123L, whilst duller pipettes were used for TASK-3 and TASK-1 – which additionally proved better seals when pressed between the pipette and cover slip with more force then normal. The experienced weaknesses in membrane could be due to the TASK channel function in cellular apoptosis, in which potassium leak is significant [Yu, 2003]. The reduced Vrev of the TASK-1 and TASK-V123L could then explain reduced potassium concentrations within the tsA-201 cells cytosol – due to less potassium influx - triggering slow apoptosis and membrane damage.

To add, only recordings of low interference went forward to be analyzed and any anomalous results were discarded. This concerned one large cell in the TASK-1_V123L data set which presented values greater the 2.5 times outside the variance of the data set, so was excluded as an outlier.

6 Conclusion

The format of this investigation proved worthy and TASK-1 channels have shown to present themselves in various ways. Concerning mutation of the N-terminus COP1 binding sites, to increase protein expression; TASK-1_K2N/R3Q, verified no significant increase in current compared to wildtype. However, based on the same effect - truncation of the TASK-1_K2N/R3Q C-terminus (TASK-1_250) removed 27 perspective phosphorylation sites, including those of 14.3.3 and P11. This proved a significant increase in current (P=0.047) when compared to TASK-1_K2N/R3Q, yet no difference in reversal potential was observed. Moving on, translation of the TASK-1 channel was proven affected by Kozak mutation -3A>U, which provided a significant increase in current (P=0.04), compared to TASK-1_K2N/R3Q, used as wildtype, but this had no effect on the reversal potential. Next, AF inducing mutation V123L, presented a disruption of pore structure, providing significantly lower current at -40 and -80mV then TASK-1 wildtype (0.02), however no significant difference in current was observed as +20mv. Additionally, V123L was proven to increase reversal potential, presenting a shift in Vrev to -57mV, from -65mV as seen in wildtype.

More so, co-expression of TASK-1 and TASK-3 produced a current similar to that of TASK-1 homodimers, and less than the mid interval between the average current values for both homodimers; proving TASK-1 to dominate the current amplitude in this co-expression. However, the reversal potential sat midrange between the Vrev potentials for the channel homodimers. Co-expression of TASK-1 with TASK_1_V123L additionally proved current values similar to those of TASK-1, with no difference in reversal potential; proving the mutational effects of V1213L to be overcome by hetermeric formation. The co-expression of TASK-3 and TASK-1_V123L additionally proved a difference in current, however the spread of data for the co-expression sat over the mid-point between values for homodimer currents, as did the reversal potentials. Proving V123L to have no dominance.

Further, confocal microscopy provided clear images membrane localization concerning the K2N/R3Q and -3A mutations tested. Yet, optimization of the method is needed for a full quantification of protein expression to be calculated.

Overall the investigation went well, with C-terminus truncation and -3A mutations suggesting an increased expression; V123L proving to be potentially pathogenic, however its effects are rectified by heterodimerization; and TASK-1 proving to dominate heteromers with TASK-1.

7 Future work

Upon continuation of this research in the topic there are several factors that could be changed. To begin, more n numbers would be collected so a fairer statistical analysis could be concluded in relation the electrophysiology data obtained. Larger n numbers would reduce the variation within each data group, by there being greater reproductions of similar figures; this would then allow for data to be compared by use of cell density; better indicating the normalized current for each cell.

Further, in cell/on cell assays could be used in conjunction with the confocal study as to provide a better quantification value for the protein expression levels, as opposed to the visual obviousness that was desired to be quantified by eye in this experiment.

Additionally, concerning the insertion of mutation into cDNA, primers of lower GC contents would be designed as to prevent the failure of PCR; despite the use of quick solution, varying temperature cycles, different taq-polymerases, and different PCR reagents. This would allow for the successful production of an equine analogue to be characterized for the first time, and additionally permit the examination of the second Kozak mutation, which further could be better reviewed based upon the tweaks to the electrophysiology and confocal protocols.

More so, the quantification of TASK-1 expression in atrial tissue of the equine heart would prove useful when predicting how the electrophysiological responses from the channels may affect the heart in context.

To add the addition of further TASK-1 mutations concerning different regions of the protein structure would be of interest to determine how location may affect severity within a patient, as demonstrated by the reduced homodimer function of TASK_1_V123L, yet this is recovered in a heteromer, compared to the total loss of function in all conformations concerning V221L [Liang, *et al*, 2014].

8 References

Acevedo J, et al. (2018). Changes in global translation elongation or initiation rates shape the proteome via the Kozak sequence. *Nature* . 8 (1), 4018

Arakel E, Brandenburg S, Uchida K, . (2014). Tuning the electrical properties of the heart by differential trafficking of KATP ion channel complexes. *J Cell Sci*. 127 (9), 2106-19.

Bohnen, M., Roman-Campos, D., Terrenoire, C., Jnani, J., Sampson, K., Chung, W. and Kass, R. (2017). The Impact of Heterozygous KCNK3 Mutations Associated With Pulmonary Arterial Hypertension on Channel Function and Pharmacological Recovery. *Journal of the American Heart Association*, 6(9).

Bonagura, John & Reef, Virginia. (2003). Disorders of the Cardiovascular System. Equine Internal Medicine: Second Edition. 355-459. 10.1016/B0-72-169777-1/50010-X.

BROWN, C., KANEENE, J. and TAYLOR, R. (1988). Sudden and unexpected death in horses and ponies: an analysis of 200 cases. Equine Veterinary Journal, 20(2), pp.99-103.

Bui, A. L., Horwich, T. B., & Fonarow, G. C. (2011). Epidemiology and risk profile of heart failure. *Nature reviews. Cardiology*, *8*(1), 30–41. doi:10.1038/nrcardio.2010.165

Büttner, Dietmar & Hackbarth, Hansjoachim & Wollnik, Franziska & Borggreve, H.. (2014). Blood pressure in rats.

Campuzano O, et al. (2016). Genetic basis of atrial fibrillation. Genes and disease. 3 (4), 257-262.

Catalyst University. (2016). Ion Channel Selectivity: K+ Channel. Available: https://www.youtube.com/watch?v=4l_OeDYbNVE. Last accessed 13/07/2019.

Chadda K, Edling C, Haseeb V. (2018). Gene and Protein Expression Profile of Selected Molecular Targets Mediating Electrophysiological Function in Pgc-1α Deficient Murine Atria. *Int J Mol Sci*. 19 (11), 3450

Chambers D, Huang C, Matthews G. Basic Physiology for Anaesthetists. Cambridge University Press. 2015.

Chen, Y. (2012). Calcium Phosphate Transfection of Eukaryotic Cells. Bio-101: e86. DOI: 10.21769/BioProtoc.86.

Choudhury, M., Boyett, M. R., & Morris, G. M. (2015). Biology of the Sinus Node and its Disease. *Arrhythmia & electrophysiology review*, *4*(1), 28–34. doi:10.15420/aer.2015.4.1.28

Conrad. S.E. (2016). When the heart of a champion gives out. Available: http://ww.thehorse.com/articles/36980/when-the-heart-of-a-champion-gives-out. Last accessed 26.10.2018.

Dhein S. (2004). Pharmacology of gap junctions in the cardiovascular system. *Cardiovascular Research*,. 62 (2), 287–298.

Doyle D, Morais Cabral J, Pfuetzner RA, Kuo A, Gulbis JM, Cohen SL, Chait BT, MacKinnon R. (1998). The structure of the potassium channel: molecular basis of K+ conduction and selectivity. Science. 280 (5360), 69-77.

Durham M. (2008). The Equine Heart Part 2: Common Cardiac Disease. *Bay Area Equestrian*. 1 (2), 1-7.

Edward R. (2019). *Heart rate.* Available: https://www.mayoclinic.org/healthy-lifestyle/fitness/expert-answers/heart-rate/faq-20057979. Last accessed 2019

Enyedi P, et al. (2010). Molecular Background of Leak K Currents: Two-Pore Domain Potassium Channels. Physiol Rev . 90 (1), 559-605.

Eva Mlyneková et al. (2016). Impact of training load on the heart rate of horses. *Acta fytotechn zootechn,*. 19 (4), 167-170.
Foldes-Papp Z, Ulrike Demel, Gernot P. Tilz. (2003). Laser scanning confocal fluorescence icroscopy: an overview. *International Immunopharmacology*. 3 (1), 1715–1729.

Franz, R. (2012). The role of action potential alternans in the initiation of atrial fibrillation in humans: a review and future directions. *Europace.* . 14 (5), 58-64.

Gaurab K. (2018). Electrocardiogram (ECG): working principle, normal ECG wave, application of ECG. *Anatomy and Physiology*. 1 (1), 1-4.

Gierten J, Ficker E, Bloehs R. (2010). The human cardiac K2P3.1 (TASK-1) potassium leak channel is a molecular target for the class III antiarrhythmic drug amiodarone.. *Naunyn Schmiedebergs Arch Pharmacol.*. 381 (3), 261-70.

Goldstein, S, Bockenhauer, D., O'Kelly, I., & Zilberberg, N. (2001). Potassium leak channels and the KCNK family of two-p-domain subunits. Nature Reviews Neuroscience, 2(3), 175–184.

Graham, F. L. and van der Eb, A. J. (1973). A new technique for the assay of infectivity of human adenovirus 5 DNA. Virology 52(2): 456-67.

Hajdú P, Chris Ulens, György Panyı, Jan Tytgat, Drug- and mutagenesis-induced changes in the selectivity filter of a cardiac two-pore background K^+ channel, *Cardiovascular Research*, Volume 58, Issue 1, April 2003, Pages 46–54.

Harleton E, Besana A. (2015). TASK-1 current is inhibited by phosphorylation during human and canine chronic atrial fibrillation.. *American Physiological*. 308 (2), 126-134.

Healthy living . (2019). Understanding blood pressure . Available: https://www.heart.org/en/health-topics/high-blood-pressure/understanding-blood-pressure-readings. Last accessed 2019

Kozak M. (1984). Point mutations define a sequence flanking the AUG initiator codon that modulates translation by eukaryotic ribosomes. CellPress. 44 (2), 283-292.

Lambert M, et al. (2018). Ion Channels in Pulmonary Hypertension: A Therapeutic Interest?. *Int J Mol Sci*. 19 (10), 3162.

Lazzerini P, Capecchi P, El-Sherif N, . (2018). Emerging Arrhythmic Risk of Autoimmune and Inflammatory Cardiac Channelopathies. *Journal of the American Heart Association.*. 7 (22), 1-19.

Lee, Mun Ching (2018) Regulation of Voltage-gated Potassium (Kv) and Two-Pore Domain Potassium (K2P) Channels implicated in Pulmonary Hypertension. Doctor of Philosophy (PhD) thesis, University of Kent,

Leithner K, Hirschmugl B, Li Y, Tang B, Papp R, Nagaraj C, et al. (2016) TASK-1 Regulates Apoptosis and Proliferation in a Subset of Non-Small Cell Lung Cancers. PLoS ONE 11(6): e0157453.

Lesage F, et al. (2000). Molecular and functional properties of two-pore-domain. *Am J Physiol Renal Physiol*. 279 (1), 793-801

Liang B, Soka M, Christensen AH, Olesen MS, Larsen AP, Knop FK, Wang F, Nielsen JB, Andersen MN, and Humphreys D et al. (2014) Genetic variation in the two-pore domain potassium channel, TASK-1, may contribute to an atrial substrate for arrhythmogenesis. J Mol Cell Cardiol 67:69–76.

Limberg SH, Netter MF, Rolfes C, Rinné S, Schlichthörl G, Zuzarte M, Vassiliou T, Moosdorf R, Wulf H, and Daut J et al. (2011) TASK-1 channels may modulate action potential duration of human atrial cardiomyocytes. Cell Physiol Biochem 28:613–624.

Lubitz s, *et al*, (2010). Implications for Future Research Directions and Personalized Medicine. Circulation: Arrhythmia and Electrophysiology. 3 (3), 291–299.

Lyle C, etal. (2010). Sudden death in racing Thoroughbred horses: An international multicentre study of post mortem findings . *Equine Veternary Journal*. 43 (3), 324-331.

M. Olesen, B. Liang, M. Soka, A.P. Larsen, F.K. Knop, F. Wang, J.B. Nielsen, M.N. Andersen, D. Humphreys, S.A. Mann, J.I. Vandenberg, J.H. Svendsen, S. Haunsø, T. Preiss, G. Seebohm, S.-P.

Mader, D. (2010). Critical care techniques in small exotic mammals. International Veterinary Information Service. Retrieved March 2, 2011, from http://www.ivis.org/proceedings/sevc/2010/lectures/eng/Mader1.pdf

Marr, C. and Bowen, I. (2010). *Cardiology of the horse*. Edinburgh: Saunders/Elsevier.

Mathie and Veale. (2010). Gating of two pore domain potassium channels. *J Physiol.*. 588 (17), 3149–3156..

Matsuura W, Sugimachi M, Kawada T, Sato T, Shishido T, Miyano H, Nakahara T, Ikeda Y, Alexander J Jr, Sunagawa K. Vagal stimulation decreases left ventricular contractility mainly through negative chronotropic effect. Am J Physiol. 1997 Aug;273.

McGuirk SM, Muir W. (1985). Diagnosis and treatment of cardiac arrhythmias. Vet Clin North Am Equine Pract.. 1 (2), 353-70

McGurrin MKJ . (2015). The diagnosis and management of atrial fibrillation in the horse. *Veterinary Medicine: Research and Reports* . 6 (1), 83—90.

Meyer D, Gatto C, Artigas P. (2019). Na/K Pump Mutations Associated with Primary Hyperaldosteronism Cause Loss of Function. *Biochemistry*. 58 (13), 1774-1785.

Molina DK, et al. (2012). Normal organ weights in men: part I-the heart. *Am J Forensic Med Pathol. Am J Forensic Med Pathol.* . 33 (4), 362-7.

Molina DK, et al. (2015). Normal Organ Weights in Women: Part I-The Heart. *Am J Forensic Med Pathol. Am J Forensic Med Pathol.* . 36 (3), 176-81.

Niemyre L, et al. (2016). Gating, Regulation, and Structure in K2P K+ Channels: In Varietate Concordia?. *Molecular Pharmacology*. 90 (3), 309-317.

Noarton J. (2017). *The Equine Circulatory System.* Available: https://equimed.com/health-centers/general-care/articles/the-equine-circulatory-system. Last accessed 2019.

Olesen, M. S., Nielsen, M. W., Haunsø, S., & Svendsen, J. H. (2014). Atrial fibrillation: the role of common and rare genetic variants. *European journal of human genetics : EJHG*, *22*(3), 297–306. doi:10.1038/ejhg.2013.139

Olesen, N. Schmitt, D. Fatkin, TASK-1 potassium channel mutations in atrial fibrillation, *European Heart Journal*, Volume 34, Issue suppl_1, 1 August 2013, 3411,
Powersteam. (2019). *Convert Watts to Amps.* Available: https://www.powerstream.com/Amps-Watts.htm. Last accessed 13/07/2019.

Patteson, M (1996). *Equine cardiology*. blackwellSciencesLtd, Oxford, p-1-254

Rinné S, et al. (2015). TASK-1 and TASK-3 may form heterodimers in human atrial cardiomyocytes. *Journal of Molecular and Cellular Cardiology*. 81 (1), 71-80.

Roberts, J. D., & Gollob, M. H. (2014). A contemporary review on the genetic basis of atrial fibrillation. *Methodist DeBakey cardiovascular journal*, *10*(1), 18–24.

Roger L. Royster MD, Leanne Groban MD, Adair Q. Locke MD Benjamin N. (2018). Chapter 8 - Cardiovascular Pharmacology. *Elseveir*. 2 (1), 132-166.

Rohr S. (2004). Role of gap junctions in the propagation of the cardiac action potential. *Cardiovascular Research*. 62 (2), 309–322.

Roy, S., & McCrory, J. (2015). Validation of Maximal Heart Rate Prediction Equations Based on Sex and Physical Activity Status. International journal of exercise science, 8(4), 318–330.

Schmidt C, Felix Wiedmann, Patrick A. Schweizer, Hugo A. Katus, Dierk Thomas. (2014b). Inhibition of cardiac two-pore-domain K+ (K2P) channels – an emerging antiarrhythmic concept. *European Journal of Pharmacology*. 738 (5), 250-255.

Schmidt C, Wiedmann F, Langer C, Tristram F, Anand P, Wenzel W, Lugenbiel P, Schweizer PA, Katus HA, Thomas D. (2014a). Cloning, functional characterization, and remodeling of K2P3.1 (TASK-1) potassium channels in a porcine model of atrial fibrillation and heart failure. *Heart Rhythm*. 11 (10), 1798-805.

Schmidt C, Wiedmann F, Voigt . (2015). Upregulation of K(2P)3.1 K+ Current Causes Action Potential Shortening in Patients With Chronic Atrial Fibrillation. *Circulation*. 132 (2), 82-92.

Schmidt C, Wiedmann F, Zhou XB, Heijman J, Voigt N, Ratte A, Lang S, Kallenberger SM, (2017) Inverse remodelling of K2P3.1 K+channel xpression

Signori E, Bagni C, Sara Papa, Beatrice Primerano. (2001). A somatic mutation in the 5′UTR of BRCA1 gene in sporadic breast cancer causes down-modulation of translation efficiency. *Nature*. 1 (20), 4596–4600.

Streit, A. K., Netter, M. F., Kempf, F., Walecki, M., Rinné, S., Bollepalli, M. K., Decher, N. (2011). A specific two-pore domain potassium channel blocker defines the structure of the TASK-1 open pore. *The Journal of biological chemistry*, *286*(16), 13977–13984. doi:10.1074/jbc.M111.227884

Sweet, C., Emmert, S., Seymour, A., Stabilito, I. and Oppenheimer, L. (1987). Measurement of cardiac output in anesthetized rats by dye dilution using a fiberoptic catheter. Journal of Pharmacological Methods, 17(3), pp.189-203.

Thermo Scientific. (2018). *TurboFect™ Transfection Reagent.* Available: https://www.thermofisher.com/order/catalog/product/R0532?gclid=EAIaIQobChMI3JWL59DP4gIV0eJ3Ch2LggMSEAAYASAAEgIkW_D_BwE&s_kwcid=AL!3652!3!265279840752!p!!g!!turbofect&ef_id=EAIaIQobChMI3JWL59DP4gIV0eJ3. Last accessed 15/06/2019.

Thomas, Philip; et al. (2005). "HEK293 cell line: A vehicle for the expression of recombinant proteins". Journal of Pharmacological and Toxicological Methods. 51 (3): 187–200.

Verheyen, Tinne & Decloedt, Annelies & De Clercq, Dominique & deprez, Piet & Sys, S.U. & van Loon, Gunther. (2010). Electrocardiography in horses - Part 1: How to make a good recording. Vlaams Diergeneeskundig Tijdschrift. 79. 331-336.

Wiedmann, F., Schulte, J.S., Gomes, B. et al.. (2018). Atrial fibrillation and heart failure-associated remodeling. *Basic Res Cardiol* . 113 (27), 113-27.

Wiedmann, F., Schulte, J.S., Gomes, B. et al.. (2018). Atrial fibrillation and heart failure-associated remodeling. *Basic Res Cardiol* . 113 (27), 113-27.

Yangmi Kim, et al. (2000). TASK-3, a New Member of the Tandem Pore K+ Channel Family. *The Journal of Biological Chemistry*. 275 (1), 9340-9347.

Yu s,. (2003). Regulation and critical role of potassium homeostasis in apoptosis.. *Prog Neurobiol.*. 70 (4), 363-86..

Zúñiga L. (2016). Understanding the Cap Structure in K2P Channels. *Front. Physiol.,*. 1 (10), 38.

9 Appendixes

1

A - Human KCNK3 amino acid

Human:
MKRQNVRTLALIVCTFTYLLVGAAVFDALESEPELIERQRLELRQQELRARYNLSQ
GGYEELERVVLRLKPHKAGVQWRFAGSFYFAITVITTIGYGHAAPSTDGGKVFCMF
YALLGIPLTLVMFQSLGERINTLVRYLLHRAKKGLGMRRADVSMANMVLIGFFSCI
STLCIGAAAFSHYEHWTFFQAYYYCFITLTTIGFGDYVALQKDQALQTQPQYVAFS
FVYILTGLTVIGAFLNLVVLRFMTMNAEDEKRDAEHRALLTRNGQAGGGGGGGSA
HTTDTASSTAAAGGGGFRNVYAEVLHFQSMCSCLWYKSREKLQYSIPMIIPRDLST
SDTCVEQSHSSPGGGGRYSDTPSRRCLCSGAPRSAISSVSTGLHSLSTFRGLMKRRS

B – Equine KCNK3 amino acid sequence

Equine
MKRQNVRTLALIVCTFTYLLVGAAVFDALESEPEMIERQRLELRQQELRARYNLSQ
GGYEELERVVLRLKPHKAGVQWRFAGSFYFAITVITTIGYGHAAPSTDGGKVFCMF
YALLGIPLTLVMFQSLGERINTFVKYLLHRAKRGLGMRRADVSMANMVLIGFFSCI
STLCIGAAAFSYYEHWTFFQAYYYCFITLTTIGFGDYVALQKDQALQTQPQYVAFSF
VYILTGLTVIGAFLNLVVLRFMTMNAEDEKRDAEHRALLTRNGQAGGACGGGGGG
GAGGSAHTTDTASSTVAAGGGGGGFRNVYAEVLHFQSMCSCLWYKSREKLQYSIP
MIIPRDLSTSDTCVEQSHSSPGGGGRYSDTPSHRCLCSGAQRSAISSVSTGLHSLSTF
RGLMKRRSSV

C – Rat KCNK3 amino acid sequence

Rat
MKRQNVRTLALIVCTFTYLLVGAAVFDALESEPEMIERQRLELRQLELRARYNLSE
GGYEELERVVLRLKPHKAGVQWRFAGSFYFAITVITTIGYGHAAPSTDGGKVFCMF
YALLGIPLTLVMFQSLGERINTFVRYLLHRAKRGLGMRHAEVSMANMVLIGFVSCI
STLCIGAAAFSYYERWTFFQAYYYCFITLTTIGFGDYVALQKDQALQTQPQYVAFSF
VYILTGLTVIGAFLNLVVLRFMTMNAEDEKRDAEHRALLTHNGQAGGLGGLSCLS
GSLGDGVRPRDPVTCAAAAGGMGVGVGVGGSGFRNVYAEMLHFQSMCSCLWYKS
REKLQYSIPMIIPRDLSTSDTCVEHSHSSPGGGGRYSDTPSHPCLCSGTQRSAISSVS
TGLHSLATFRGLMKRRSSV

D – Human KCNK9 amino acid sequence

MKRQNVRTLSLIVCTFTYLLVGAAVFDALESDHEMREEEKLKAEEIRIKGKYNISSE
DYRQLELVILQSEPHRAGVQWKFAGSFYFAITVITTIGYGHAAPGTDAGKAFCMFY
AVLGIPLTLVMFQSLGERMNTFVRYLLKRIKKCCGMRNTDVSMENMVTVGFFSC
MGTLCIGAAAFSQCEEWSFFHAYYYCFITLTTIGFGDYVALQTKGALQKKPLYVAF
SFMYILVGLTVIGAFLNLVVLRFLTMNSEDERRDAEERASLAGNRRNSMVIHIPEEP
RPSRPRYKADVPDLQSVCSCTCYRSQDYGGRSVAPQNSFSAKLAPHYFHSISYKIEE
ISPSTLKNSLFPSPISSISPGLHSFTDHQRLMKRRKSV

E – Equine KCNK9 amino acid sequence

MKRQNVRTLSLIVCTFTYLLVGAAVFDALESDHEMREEEKLKAEEIRIKGKYNISSE
DYRQLELVILQSEPHRAGVQWKFAGSFYFAITVITTIGYGHAAPGTDAGKAFCMFY
AVLGIPLTLVMFQSLGERMNTFVRYLLKRIKKCCGMRNTEVSMENMVTVGFFSCM
GTLCIGAAAFSQCEEWSFFHAYYYCFITLTTIGFGDYVALQTKGALQKKPLYVAFSF
MYILVGLTVIGAFLNLVVLRFLTMNSEDERRDAEERASLAGNRRNSMVIHIPEEARQ
GRPRYKADVADLQSVCSCTCYRPQEYGGRSAAHQNSVSAKLAPQYFHSISYKIEEIS
PSTLKNSLFPSPISSISPGLHSFTDNHRLMRRRKSI

2

A – Human (subject) v equine KCNK3 amino acid alignment

Range 1: 1 to 394 Graphics ▼ Next Match ▲ Previous Match

Score	Expect	Method	Identities	Positives	Gaps
783 bits(2023)	0.0	Compositional matrix adjust.	385/403(96%)	389/403(96%)	9/403(2%)

```
Query  1    MKRQNVRTLALIVCTFTYLLVGAAVFDALESEPEMIERQRLELRQQELRARYNLSQGGYE  60
            MKRQNVRTLALIVCTFTYLLVGAAVFDALESEPE+IERQRLELRQQELRARYNLSQGGYE
Sbjct  1    MKRQNVRTLALIVCTFTYLLVGAAVFDALESEPELIERQRLELRQQELRARYNLSQGGYE  60

Query  61   ELERVVLRLKPHKAGVQWRFAGSFYFAITVITTIGYGHAAPSTDGGKVFCMFYALLGIPL  120
            ELERVVLRLKPHKAGVQWRFAGSFYFAITVITTIGYGHAAPSTDGGKVFCMFYALLGIPL
Sbjct  61   ELERVVLRLKPHKAGVQWRFAGSFYFAITVITTIGYGHAAPSTDGGKVFCMFYALLGIPL  120

Query  121  TLVMFQSLGERINTFVKYLLHRAKRGLGMRRADVSMANMVLIGFFSCISTLCIGAAAFSY  180
            TLVMFQSLGERINT V+YLLHRAK+GLGMRRADVSMANMVLIGFFSCISTLCIGAAAFS+
Sbjct  121  TLVMFQSLGERINTLVRYLLHRAKKGLGMRRADVSMANMVLIGFFSCISTLCIGAAAFSH  180

Query  181  YEHWTFFQAYYYCFITLTTIGFGDYVALQKDQALQTQPQYVAFSFVYILTGLTVIGAFLN  240
            YEHWTFFQAYYYCFITLTTIGFGDYVALQKDQALQTQPQYVAFSFVYILTGLTVIGAFLN
Sbjct  181  YEHWTFFQAYYYCFITLTTIGFGDYVALQKDQALQTQPQYVAFSFVYILTGLTVIGAFLN  240

Query  241  LVVLRFMTMNAEDEKRDAEHRALLTRNGQAGGACGGGGGGGAGGSAHTTDTASSTVAAGG  300
            LVVLRFMTMNAEDEKRDAEHRALLTRNGQA        GGGG GGSAHTTDTASST AA
Sbjct  241  LVVLRFMTMNAEDEKRDAEHRALLTRNGQA-------GGGGGGGSAHTTDTASSTAAA--  291

Query  301  GGGGFRNVYAEVLHFQSMCSCLWYKSREKLQYSIPMIIPRDLSTSDTCVEQSHSSPGGGG  360
            GGGGFRNVYAEVLHFQSMCSCLWYKSREKLQYSIPMIIPRDLSTSDTCVEQSHSSPGGGG
Sbjct  292  GGGGFRNVYAEVLHFQSMCSCLWYKSREKLQYSIPMIIPRDLSTSDTCVEQSHSSPGGGG  351

Query  361  RYSDTPSHRCLCSGAQRSAISSVSTGLHSLSTFRGLMKRRSSV  403
            RYSDTPS RCLCSGA RSAISSVSTGLHSLSTFRGLMKRRSSV
Sbjct  352  RYSDTPSRRCLCSGAPRSAISSVSTGLHSLSTFRGLMKRRSSV  394
```

B – Human v Rat KCNK3 amino acid alignment

Range 1: 1 to 394 Graphics ▼ Next Match ▲ Previous Match

Score	Expect	Method	Identities	Positives	Gaps
721 bits(1860)	0.0	Compositional matrix adjust.	360/411(88%)	368/411(89%)	17/411(4%)

```
Query  1    MKRQNVRTLALIVCTFTYLLVGAAVFDALESEPEMIERQRLELRQLELRARYNLSEGGYE  60
            MKRQNVRTLALIVCTFTYLLVGAAVFDALESEPE+IERQRLELRQ ELRARYNLS+GGYE
Sbjct  1    MKRQNVRTLALIVCTFTYLLVGAAVFDALESEPELIERQRLELRQQELRARYNLSQGGYE  60

Query  61   ELERVVLRLKPHKAGVQWRFAGSFYFAITVITTIGYGHAAPSTDGGKVFCMFYALLGIPL  120
            ELERVVLRLKPHKAGVQWRFAGSFYFAITVITTIGYGHAAPSTDGGKVFCMFYALLGIPL
Sbjct  61   ELERVVLRLKPHKAGVQWRFAGSFYFAITVITTIGYGHAAPSTDGGKVFCMFYALLGIPL  120

Query  121  TLVMFQSLGERINTFVRYLLHRAKRGLGMRHAEVSMANMVLIGFVSCISTLCIGAAAFSY  180
            TLVMFQSLGERINT VRYLLHRAK+GLGMR A+VSMANMVLIGF SCISTLCIGAAAFS+
Sbjct  121  TLVMFQSLGERINTLVRYLLHRAKKGLGMRRADVSMANMVLIGFFSCISTLCIGAAAFSH  180

Query  181  YERWTFFQAYYYCFITLTTIGFGDYVALQKDQALQTQPQYVAFSFVYILTGLTVIGAFLN  240
            YE WTFFQAYYYCFITLTTIGFGDYVALQKDQALQTQPQYVAFSFVYILTGLTVIGAFLN
Sbjct  181  YEHWTFFQAYYYCFITLTTIGFGDYVALQKDQALQTQPQYVAFSFVYILTGLTVIGAFLN  240

Query  241  LVVLRFMTMNAEDEKRDAEHRALLTHNGQAGGLGGLSCLSGSLGDGVRPRDPVTCAAAAG  300
            LVVLRFMTMNAEDEKRDAEHRALLT NGQA          G  G       D  +  AAA
Sbjct  241  LVVLRFMTMNAEDEKRDAEHRALLTRNGQA--------GGGGGGGSAHTTDTASSTAAA-  291

Query  301  GMGVGVGVGGSGFRNVYAEMLHFQSMCSCLWYKSREKLQYSIPMIIPRDLSTSDTCVEHS  360
                    GG GFRNVYAE+LHFQSMCSCLWYKSREKLQYSIPMIIPRDLSTSDTCVE S
Sbjct  292  --------GGGGFRNVYAEVLHFQSMCSCLWYKSREKLQYSIPMIIPRDLSTSDTCVEQS  343

Query  361  HSSPGGGGRYSDTPSHPCLCSGTQRSAISSVSTGLHSLATFRGLMKRRSSV  411
            HSSPGGGGRYSDTPS  CLCSG  RSAISSVSTGLHSL+TFRGLMKRRSSV
Sbjct  344  HSSPGGGGRYSDTPSRRCLCSGAPRSAISSVSTGLHSLSTFRGLMKRRSSV  394
```

C – Equine v rat KCNK3 amino acid alignment

Range 1: 1 to 403 Graphics ▼ Next Match ▲ Previous Match

Score	Expect	Method	Identities	Positives	Gaps
717 bits(1852)	0.0	Compositional matrix adjust.	368/411(90%)	375/411(91%)	8/411(1%)

```
Query  1    MKRQNVRTLALIVCTFTYLLVGAAVFDALESEPEMIERQRLELRQLELRARYNLSEGGYE  60
            MKRQNVRTLALIVCTFTYLLVGAAVFDALESEPEMIERQRLELRQ ELRARYNLS+GGYE
Sbjct  1    MKRQNVRTLALIVCTFTYLLVGAAVFDALESEPEMIERQRLELRQQELRARYNLSQGGYE  60

Query  61   ELERVVLRLKPHKAGVQWRFAGSFYFAITVITTIGYGHAAPSTDGGKVFCMFYALLGIPL  120
            ELERVVLRLKPHKAGVQWRFAGSFYFAITVITTIGYGHAAPSTDGGKVFCMFYALLGIPL
Sbjct  61   ELERVVLRLKPHKAGVQWRFAGSFYFAITVITTIGYGHAAPSTDGGKVFCMFYALLGIPL  120

Query  121  TLVMFQSLGERINTFVRYLLHRAKRGLGMRHAEVSMANMVLIGFVSCISTLCIGAAAFSY  180
            TLVMFQSLGERINTFV+YLLHRAKRGLGMR A+VSMANMVLIGF SCISTLCIGAAAFSY
Sbjct  121  TLVMFQSLGERINTFVKYLLHRAKRGLGMRRADVSMANMVLIGFFSCISTLCIGAAAFSY  180

Query  181  YERWTFFQAYYYCFITLTTIGFGDYVALQKDQALQTQPQYVAFSFVYILTGLTVIGAFLN  240
            YE WTFFQAYYYCFITLTTIGFGDYVALQKDQALQTQPQYVAFSFVYILTGLTVIGAFLN
Sbjct  181  YEHWTFFQAYYYCFITLTTIGFGDYVALQKDQALQTQPQYVAFSFVYILTGLTVIGAFLN  240

Query  241  LVVLRFMTMNAEDEKRDAEHRALLTHNGQAGGLGGLSCLSGSLGDGVRPRDPVTCAAAAG  300
            LVVLRFMTMNAEDEKRDAEHRALLT NGQAGG  G     G+ G      D  +   AAG
Sbjct  241  LVVLRFMTMNAEDEKRDAEHRALLTRNGQAGGACGGGGGGGAGGSA-HTTDTASSTVAAG  299

Query  301  GMGVGVGVGGSGFRNVYAEMLHFQSMCSCLWYKSREKLQYSIPMIIPRDLSTSDTCVEHS  360
            G          G GFRNVYAE+LHFQSMCSCLWYKSREKLQYSIPMIIPRDLSTSDTCVE S
Sbjct  300  GG-------GGGFRNVYAEVLHFQSMCSCLWYKSREKLQYSIPMIIPRDLSTSDTCVEQS  352

Query  361  HSSPGGGGRYSDTPSHPCLCSGTQRSAISSVSTGLHSLATFRGLMKRRSSV  411
            HSSPGGGGRYSDTPSH CLCSG QRSAISSVSTGLHSL+TFRGLMKRRSSV
Sbjct  353  HSSPGGGGRYSDTPSHRCLCSGAQRSAISSVSTGLHSLSTFRGLMKRRSSV  403
```

D – Human v equine (subject) C-terminus truncated KCNK3 amino acid alignment

Range 1: 1 to 250 Graphics ▼ Next Match ▲ Previous Match

Score	Expect	Method	Identities	Positives	Gaps
506 bits(1304)	0.0	Compositional matrix adjust.	245/250(98%)	249/250(99%)	0/250(0%)

```
Query  1    MKRQNVRTLALIVCTFTYLLVGAAVFDALESEPELIERQRLELRQQELRARYNLSQGGYE  60
            MKRQNVRTLALIVCTFTYLLVGAAVFDALESEPE+IERQRLELRQQELRARYNLSQGGYE
Sbjct  1    MKRQNVRTLALIVCTFTYLLVGAAVFDALESEPEMIERQRLELRQQELRARYNLSQGGYE  60

Query  61   ELERVVLRLKPHKAGVQWRFAGSFYFAITVITTIGYGHAAPSTDGGKVFCMFYALLGIPL  120
            ELERVVLRLKPHKAGVQWRFAGSFYFAITVITTIGYGHAAPSTDGGKVFCMFYALLGIPL
Sbjct  61   ELERVVLRLKPHKAGVQWRFAGSFYFAITVITTIGYGHAAPSTDGGKVFCMFYALLGIPL  120

Query  121  TLVMFQSLGERINTLVRYLLHRAKKGLGMRRADVSMANMVLIGFFSCISTLCIGAAAFSH  180
            TLVMFQSLGERINT V+YLLHRAK+GLGMRRADVSMANMVLIGFFSCISTLCIGAAAFS+
Sbjct  121  TLVMFQSLGERINTFVKYLLHRAKRGLGMRRADVSMANMVLIGFFSCISTLCIGAAAFSY  180

Query  181  YEHWTFFQAYYYCFITLTTIGFGDYVALQKDQALQTQPQYVAFSFVYILTGLTVIGAFLN  240
            YEHWTFFQAYYYCFITLTTIGFGDYVALQKDQALQTQPQYVAFSFVYILTGLTVIGAFLN
Sbjct  181  YEHWTFFQAYYYCFITLTTIGFGDYVALQKDQALQTQPQYVAFSFVYILTGLTVIGAFLN  240

Query  241  LVVLRFMTMN  250
            LVVLRFMTMN
Sbjct  241  LVVLRFMTMN  250
```

E – Human (subject) v equine KCNK9 amino acid alignment

Range 1: 1 to 374 GenPept Graphics ▼ Next Match ▲ Previous Match

Score	Expect	Method	Identities	Positives	Gaps
749 bits(1935)	0.0	Compositional matrix adjust.	359/374(96%)	364/374(97%)	0/374(0%)

```
Query  1    MKRQNVRTLSLIVCTFTYLLVGAAVFDALESDHEMREEEKLKAEEIRIKGKYNISSEDYR  60
            MKRQNVRTLSLIVCTFTYLLVGAAVFDALESDHEMREEEKLKAEEIRIKGKYNISSEDYR
Sbjct  1    MKRQNVRTLSLIVCTFTYLLVGAAVFDALESDHEMREEEKLKAEEIRIKGKYNISSEDYR  60

Query  61   QLELVILQSEPHRAGVQWKFAGSFYFAITVITTIGYGHAAPGTDAGKAFCMFYAVLGIPL  120
            QLELVILQSEPHRAGVQWKFAGSFYFAITVITTIGYGHAAPGTDAGKAFCMFYAVLGIPL
Sbjct  61   QLELVILQSEPHRAGVQWKFAGSFYFAITVITTIGYGHAAPGTDAGKAFCMFYAVLGIPL  120

Query  121  TLVMFQSLGERMNTFVRYLLKRIKKCCGMRNTEVSMENMVTVGFFSCMGTLCIGAAAFSQ  180
            TLVMFQSLGERMNTFVRYLLKRIKKCCGMRNT+VSMENMVTVGFFSCMGTLCIGAAAFSQ
Sbjct  121  TLVMFQSLGERMNTFVRYLLKRIKKCCGMRNTDVSMENMVTVGFFSCMGTLCIGAAAFSQ  180

Query  181  CEEWSFFHAYYYCFITLTTIGFGDYVALQTKGALQKKPLYVAFSFMYILVGLTVIGAFLN  240
            CEEWSFFHAYYYCFITLTTIGFGDYVALQTKGALQKKPLYVAFSFMYILVGLTVIGAFLN
Sbjct  181  CEEWSFFHAYYYCFITLTTIGFGDYVALQTKGALQKKPLYVAFSFMYILVGLTVIGAFLN  240

Query  241  LVVLRFLTMNSEDERRDAEERASLAGNRNSMVIHIPEEARQGRPRYKADVADLQSVCSCT  300
            LVVLRFLTMNSEDERRDAEERASLAGNRNSMVIHIPEE R  RPRYKADV DLQSVCSCT
Sbjct  241  LVVLRFLTMNSEDERRDAEERASLAGNRNSMVIHIPEEPRPSRPRYKADVPDLQSVCSCT  300

Query  301  CYRPQEYGGRSAAHQNSVSAKLAPQYFHSISYKIEEISPSTLKNSLFPSPISSISPGLHS  360
            CYR Q+YGGRS A QNS SAKLAP YFHSISYKIEEISPSTLKNSLFPSPISSISPGLHS
Sbjct  301  CYRSQDYGGRSVAPQNSFSAKLAPHYFHSISYKIEEISPSTLKNSLFPSPISSISPGLHS  360

Query  361  FTDNHRLMRRRKSI  374
            FTD+ RLM+RRKS+
Sbjct  361  FTDHQRLMKRRKSV  374
```

F – Human KCNK3 (subject) v human KCNK9 amino acid alignment

Range 1: 1 to 394 GenPept Graphics ▼ Next Match ▲ Previous Match

Score	Expect	Method	Identities	Positives	Gaps
443 bits(1140)	1e-154	Compositional matrix adjust.	233/395(59%)	278/395(70%)	22/395(5%)

```
Query  1    MKRQNVRTLSLIVCTFTYLLVGAAVFDALESDHEMREEEKLKAEEIRIKGKYNISSEDYR  60
            MKRQNVRTL+LIVCTFTYLLVGAAVFDALES+ E+ E ++L+  +  ++ +YN+S   Y
Sbjct  1    MKRQNVRTLALIVCTFTYLLVGAAVFDALESEPELIERQRLELRQQELRARYNLSQGGYE  60

Query  61   QLELVILQSEPHRAGVQWKFAGSFYFAITVITTIGYGHAAPGTDAGKAFCMFYAVLGIPL  120
            +LE V+L+ +PH+AGVQW+FAGSFYFAITVITTIGYGHAAP TD GK FCMFYA+LGIPL
Sbjct  61   ELERVVLRLKPHKAGVQWRFAGSFYFAITVITTIGYGHAAPSTDGGKVFCMFYALLGIPL  120

Query  121  TLVMFQSLGERMNTFVRYLLKRIKKCCGMRNTDVSMENMVTVGFFSCMGTLCIGAAAFSQ  180
            TLVMFQSLGER+NT VRYLL R KK  GMR  DVSM NMV +GFFSC+ TLCIGAAAFS
Sbjct  121  TLVMFQSLGERINTLVRYLLHRAKKGLGMRRADVSMANMVLIGFFSCISTLCIGAAAFSH  180

Query  181  CEEWSFFHAYYYCFITLTTIGFGDYVALQTKGALQKKPLYVAFSFMYILVGLTVIGAFLN  240
             E W+FF AYYYCFITLTTIGFGDYVALQ   ALQ +P YVAFSF+YIL GLTVIGAFLN
Sbjct  181  YEHWTFFQAYYYCFITLTTIGFGDYVALQKDQALQTQPQYVAFSFVYILTGLTVIGAFLN  240

Query  241  LVVLRFLTMNSEDERRDAEERASLAGNRNSMVI------HIPEEPRPS--------RPRY  286
            LVVLRF+TMN+EDE+RDAE RA L  N  +         H  +    +        R  Y
Sbjct  241  LVVLRFMTMNAEDEKRDAEHRALLTRNGQAGGGGGGGSAHTTDTASSTAAAGGGGFRNVY  300

Query  287  KADVPDLQSVCSCTCYRSQD---YGGRSVAPQNSFSAKLAPHYFHSISYKIEEISPSTLK  343
             A+V   QS+CSC  Y+S++   Y     + P++  ++       HS       S +  +
Sbjct  301  -AEVLHFQSMCSCLWYKSREKLQYSIPMIIPRDLSTSDTCVEQSHSSPGGGGRYSDTPSR  359

Query  344  NSLFP----SPISSISPGLHSFTDHQRLMKRRKSV  374
              L      S ISS+S GLHS +  + LMKRR SV
Sbjct  360  RCLCSGAPRSAISSVSTGLHSLSTFRGLMKRRSSV  394
```

G – Equine KCNK3 (subject) v equine KCNK9 amino acid alignment

Range 1: 1 to 403 GenPept Graphics ▼ Next Match ▲ Previous Match

Score	Expect	Method	Identities	Positives	Gaps
430 bits(1106)	4e-150	Compositional matrix adjust.	230/411(56%)	276/411(67%)	45/411(10%)

```
Query  1    MKRQNVRTLSLIVCTFTYLLVGAAVFDALESDHEMREEEKLKAEEIRIKGKYNISSEDYR  60
            MKRQNVRTL+LIVCTFTYLLVGAAVFDALES+ EM E ++L+  +  ++ +YN+S   Y
Sbjct  1    MKRQNVRTLALIVCTFTYLLVGAAVFDALESEPEMIERQRLELRQQELRARYNLSQGGYE  60

Query  61   QLELVILQSEPHRAGVQWKFAGSFYFAITVITTIGYGHAAPGTDAGKAFCMFYAVLGIPL  120
            +LE V+L+ +PH+AGVQW+FAGSFYFAITVITTIGYGHAAP TD GK FCMFYA+LGIPL
Sbjct  61   ELERVVLRLKPHKAGVQWRFAGSFYFAITVITTIGYGHAAPSTDGGKVFCMFYALLGIPL  120

Query  121  TLVMFQSLGERMNTFVRYLLKRIKKCCGMRNTEVSMENMVTVGFFSCMGTLCIGAAAFSQ  180
            TLVMFQSLGER+NTFV+YLL R K+  GMR  +VSM NMV +GFFSC+ TLCIGAAAFS
Sbjct  121  TLVMFQSLGERINTFVKYLLHRAKRGLGMRRADVSMANMVLIGFFSCISTLCIGAAAFSY  180

Query  181  CEEWSFFHAYYYCFITLTTIGFGDYVALQTKGALQKKPLYVAFSFMYILVGLTVIGAFLN  240
             E W+FF AYYYCFITLTTIGFGDYVALQ   ALQ +P YVAFSF+YIL GLTVIGAFLN
Sbjct  181  YEHWTFFQAYYYCFITLTTIGFGDYVALQKDQALQTQPQYVAFSFVYILTGLTVIGAFLN  240

Query  241  LVVLRFLTMNSEDERRDAEERASLAGNRNSMVI-------------HIPEEARQG-----  282
            LVVLRF+TMN+EDE+RDAE RA L  N  +                 H  + A
Sbjct  241  LVVLRFMTMNAEDEKRDAEHRALLTRNGQAGGACGGGGGGGAGGSAHTTDTASSTVAAGG  300

Query  283  -----RPRYKADVADLQSVCSCTCYRPQEY--------------GGRSAAHQNSVSAKLA  323
                 R  Y A+V   QS+CSC  Y+ +E                +   Q+  S
Sbjct  301  GGGGFRNVY-AEVLHFQSMCSCLWYKSREKLQYSIPMIIPRDLSTSDTCVEQSHSSPGGG  359

Query  324  PQYFHSISYKIEEISPSTLKNSLFPSPISSISPGLHSFTDNHRLMRRRKSI  374
             +Y  + S++        L +    S ISS+S GLHS +    LM+RR S+
Sbjct  360  GRYSDTPSHR-------CLCSGAQRSAISSVSTGLHSLSTFRGLMKRRSSV  403
```

H – Uniprot alignment of Human, equine and rat KCNK3 amino acid sequences identifying different protein domains

```
O14649 KCNK3_HUMAN    1   MKRQNVRTLALIVCTFTYLLVGAAVFDALESEPELIERQRLELRQQELRARYNLSQGGYE  60
O54912 KCNK3_RAT      1   MKRQNVRTLALIVCTFTYLLVGAAVFDALESEPEMIERQRLELRQLELRARYNLSEGGYE  60
KCNK3_HORSE           1   MKRQNVRTLALIVCTFTYLLVGAAVFDALESEPEMIERQRLELRQQELRARYNLSQGGYE  60
                          ********************************:********* *********:****

O14649 KCNK3_HUMAN   61   ELERVVLRLKPHKAGVQWRFAGSFYFAITVITTIGYGHAAPSTDGGKVFCMFYALLGIPL  120
O54912 KCNK3_RAT     61   ELERVVLRLKPHKAGVQWRFAGSFYFAITVITTIGYGHAAPSTDGGKVFCMFYALLGIPL  120
KCNK3_HORSE          61   ELERVVLRLKPHKAGVQWRFAGSFYFAITVITTIGYGHAAPSTDGGKVFCMFYALLGIPL  120
                          ************************************************************

O14649 KCNK3_HUMAN  121   TLVMFQSLGERINTLVRYLLHRAKKGLGMRRADVSMANMVLIGFFSCISTLCIGAAAFSH  180
O54912 KCNK3_RAT    121   TLVMFQSLGERINTFVRYLLHRAKRGLGMRHAEVSMANMVLIGFVSCISTLCIGAAAFSY  180
KCNK3_HORSE         121   TLVMFQSLGERINTFVKYLLHRAKRGLGMRRADVSMANMVLIGFFSCISTLCIGAAAFSY  180
                          **************:*:*******:*****:*:**********.**************:

O14649 KCNK3_HUMAN  181   YEHWTFFQAYYYCFITLTTIGFGDYVALQKDQALQTQPQYVAFSFVYILTGLTVIGAFLN  240
O54912 KCNK3_RAT    181   YERWTFFQAYYYCFITLTTIGFGDYVALQKDQALQTQPQYVAFSFVYILTGLTVIGAFLN  240
KCNK3_HORSE         181   YEHWTFFQAYYYCFITLTTIGFGDYVALQKDQALQTQPQYVAFSFVYILTGLTVIGAFLN  240
                          **:************************************************************

O14649 KCNK3_HUMAN  241   LVVLRFMTMNAEDEKRDAEHRALLTRNGQAGG-------GGGGGS-AHTTD-------TA  285
O54912 KCNK3_RAT    241   LVVLRFMTMNAEDEKRDAEHRALLTHNGQAGGLGGLSCLSGSLGDGVRPRDPVTCAAAAG  300
KCNK3_HORSE         241   LVVLRFMTMNAEDEKRDAEHRALLTRNGQAGGACGGGGGGGAGGS-AHTTD-------TA  292
                          ************************:******       .*. *. .:  *       :.

O14649 KCNK3_HUMAN  286   SSTAA--AGGGGFRNVYAEVLHFQSMCSCLWYKSREKLQYSIPMIIPRDLSTSDTCVEQS  343
O54912 KCNK3_RAT    301   GMGVGVGVGGGSGFRNVYAEMLHFQSMCSCLWYKSREKLQYSIPMIIPRDLSTSDTCVEHS  360
KCNK3_HORSE         293   SSTVAAGGGGGGFRNVYAEVLHFQSMCSCLWYKSREKLQYSIPMIIPRDLSTSDTCVEQS  352
                          .  ..    **.********:************************************:*

O14649 KCNK3_HUMAN  344   HSSPGGGGRYSDTPSRRCLCSGAPRSAISSVSTGLHSLSTFRGLMKRRSSV  394
O54912 KCNK3_RAT    361   HSSPGGGGRYSDTPSHPCLCSGTQRSAISSVSTGLHSLATFRGLMKRRSSV  411
KCNK3_HORSE         353   HSSPGGGGRYSDTPSHRCLCSGAQRSAISSVSTGLHSLSTFRGLMKRRSSV  403
                          **************: *****: **************:************
```

Annotation

- ☑ Topological domain
- ☐ Glycosylation
- ☐ Natural variant
- ☑ Transmembrane
- ☑ Intramembrane
- ☐ Chain
- ☐ Mutagenesis

I – Clustal omega alignment of Human, equine and rat KCNK3 amino acid sequences identifying residues of different properties

```
KCNK3_RAT       MKRQNVRTLALIVCTFTYLLVGAAVFDALESEPEMIERQRLELRQLELRARYNLSEGGYE   60
KCNK3_HUMAN     MKRQNVRTLALIVCTFTYLLVGAAVFDALESEPELIERQRLELRQQELRARYNLSQGGYE   60
KCNK3_HORSE     MKRQNVRTLALIVCTFTYLLVGAAVFDALESEPEMIERQRLELRQQELRARYNLSQGGYE   60
                ********************************:********* *********:****

KCNK3_RAT       ELERVVLRLKPHKAGVQWRFAGSFYFAITVITTIGYGHAAPSTDGGKVFCMFYALLGIPL   120
KCNK3_HUMAN     ELERVVLRLKPHKAGVQWRFAGSFYFAITVITTIGYGHAAPSTDGGKVFCMFYALLGIPL   120
KCNK3_HORSE     ELERVVLRLKPHKAGVQWRFAGSFYFAITVITTIGYGHAAPSTDGGKVFCMFYALLGIPL   120
                ************************************************************

KCNK3_RAT       TLVMFQSLGERINTFVRYLLHRAKRGLGMRHAEVSMANMVLIGFVSCISTLCIGAAAFSY   180
KCNK3_HUMAN     TLVMFQSLGERINTLVRYLLHRAKKGLGMRRADVSMANMVLIGFFSCISTLCIGAAAFSH   180
KCNK3_HORSE     TLVMFQSLGERINTFVKYLLHRAKRGLGMRRADVSMANMVLIGFFSCISTLCIGAAAFSY   180
                *************:*:*******:******:*:***********.**************:

KCNK3_RAT       YERWTFFQAYYYCFITLTTIGFGDYVALQKDQALQTQPQYVAFSFVYILTGLTVIGAFLN   240
KCNK3_HUMAN     YEHWTFFQAYYYCFITLTTIGFGDYVALQKDQALQTQPQYVAFSFVYILTGLTVIGAFLN   240
KCNK3_HORSE     YEHWTFFQAYYYCFITLTTIGFGDYVALQKDQALQTQPQYVAFSFVYILTGLTVIGAFLN   240
                **:************************************************************

KCNK3_RAT       LVVLRFMTMNAEDEKRDAEHRALLTHNGQAGGLGGLSCLSGSLGDGVRPRDPVTCAAAAG   300
KCNK3_HUMAN     LVVLRFMTMNAEDEKRDAEHRALLTRNGQAGG-------GGGGGS-AHTTD-------TA   285
KCNK3_HORSE     LVVLRFMTMNAEDEKRDAEHRALLTRNGQAGGACGGGGGGGAGGS-AHTTD-------TA   292
                *************************:******       .*. *. .:  *       :.

KCNK3_RAT       GMGVGVGVGGSGFRNVYAEMLHFQSMCSCLWYKSREKLQYSIPMIIPRDLSTSDTCVEHS   360
KCNK3_HUMAN     SSTAA--AGGGGFRNVYAEVLHFQSMCSCLWYKSREKLQYSIPMIIPRDLSTSDTCVEQS   343
KCNK3_HORSE     SSTVAAGGGGGGFRNVYAEVLHFQSMCSCLWYKSREKLQYSIPMIIPRDLSTSDTCVEQS   352
                .  ..    **.********:*************************************:*

KCNK3_RAT       HSSPGGGGRYSDTPSHPCLCSGTQRSAISSVSTGLHSLATFRGLMKRRSSV    411
KCNK3_HUMAN     HSSPGGGGRYSDTPSRRCLCSGAPRSAISSVSTGLHSLSTFRGLMKRRSSV    394
KCNK3_HORSE     HSSPGGGGRYSDTPSHRCLCSGAQRSAISSVSTGLHSLSTFRGLMKRRSSV    403
                **************: *****: **************:************
```

Residue	Colour	Property
AVFPMILW	RED	Small (small+ hydrophobic (incl.aromatic -Y))
DE	BLUE	Acidic
RK	MAGENTA	Basic - H
STYHCNGQ	GREEN	Hydroxyl + sulfhydryl + amine + G
Others	Grey	Unusual amino/imino acids etc

3 Alignment of native and optimized equine KCNK3 nucleotide sequences

```
CLUSTAL O(1.2.4) multiple sequence alignment

native_sequence_joint_exons_1_2                 ATGAAGCGGCAGAACGTGCGCACGCTGGCGCTCATCGTGTGCACCTTCACCTACCTGCTG 60
sequance_from_insilico_reverse_transcription    ATGAAGAGGCAGAACGTGAGGACCCTGGCCCTGATCGTGTGCACCTTCACCTACCTGCTG 60
                                                ****** *********** * ** ***** ** ****************************

native_sequence_joint_exons_1_2                 GTGGGCGCCGCGGTCTTCGACGCGCTGGAGTCGGAGCCCGAGATGATCGAGCGGCAGCGG 120
sequance_from_insilico_reverse_transcription    GTGGGCGCCGCCGTGTTCGACGCCCTGGAGAGCGAGCCCGAGATGATCGAGAGGCAGAGG 120
                                                *********** ** ******** ******   ****************** ***** **

native_sequence_joint_exons_1_2                 CTGGAGCTGCGGCAGCAGGAGCTGCGGGCGCGCTACAACCTCAGCCAAGGCGGCTACGAG 180
sequance_from_insilico_reverse_transcription    CTGGAGCTGAGGCAGCAGGAGCTGAGGGCCAGGTACAACCTGAGCCAGGGCGGCTACGAG 180
                                                ********* ************** ****  * ******** ***** ************

native_sequence_joint_exons_1_2                 GAGCTCGAGCGCGTCGTGCTGCGCCTCAAGCCACACAAGGCCGGCGTGCAGTGGCGCTTC 240
sequance_from_insilico_reverse_transcription    GAGCTGGAGAGGGTGGTGCTGAGGCTGAAGCCCCACAAGGCCGGCGTGCAGTGGAGGTTC 240
                                                ***** *** * ** ****** * ** ***** ********************** * ***

native_sequence_joint_exons_1_2                 GCCGGCTCTTTCTACTTCGCCATCACCGTCATCACCACCATCGGCTATGGCCACGCAGCT 300
sequance_from_insilico_reverse_transcription    GCCGGCAGCTTCTACTTCGCCATCACCGTGATCACCACCATCGGCTACGGCCACGCCGCC 300
                                                ******   ********************* ****************** ******** **

native_sequence_joint_exons_1_2                 CCCAGCACGGATGGCGGCAAGGTGTTCTGCATGTTCTACGCGCTGCTGGGCATCCCGCTC 360
sequance_from_insilico_reverse_transcription    CCCAGCACCGACGGCGGCAAGGTGTTCTGCATGTTCTACGCCCTGCTGGGCATCCCCCTG 360
                                                ******** ** ******************************** ************** **

native_sequence_joint_exons_1_2                 ACGCTCGTCATGTTCCAGAGCCTGGGCGAGCGCATCAACACCTTCGTGAAGTACCTGCTG 420
sequance_from_insilico_reverse_transcription    ACCCTGGTGATGTTCCAGAGCCTGGGCGAGAGGATCAACACCTTCGTGAAGTACCTGCTG 420
                                                ** ** ** ********************** * ***************************

native_sequence_joint_exons_1_2                 CACCGCGCCAAGAGGGGGCTGGGCATGCGGCGCGCCGACGTGTCCATGGCCAACATGGTG 480
sequance_from_insilico_reverse_transcription    CACAGGGCCAAGAGGGGCCTGGGCATGAGGAGGGCCGACGTGAGCATGGCCAACATGGTG 480
                                                *** * *********** ********* ** * *********  ****************

native_sequence_joint_exons_1_2                 CTCATCGGCTTCTTCTCGTGCATCAGCACGCTGTGCATCGGCGCCGCCGCCTTCTCCTAC 540
sequance_from_insilico_reverse_transcription    CTGATCGGCTTCTTCAGCTGCATCAGCACCCTGTGCATCGGCGCCGCCGCCTTCAGCTAC 540
                                                ** ************   *********** ************************  ****

native_sequence_joint_exons_1_2                 TACGAGCACTGGACCTTCTTCCAGGCCTACTACTACTGCTTCATCACGCTCACCACCATC 600
sequance_from_insilico_reverse_transcription    TACGAGCACTGGACCTTCTTCCAGGCCTACTACTACTGCTTCATCACCCTGACCACCATC 600
                                                ************************************************ *********

native_sequence_joint_exons_1_2                 GGCTTCGGCGACTACGTGGCGCTGCAGAAGGACCAGGCGCTGCAAACGCAGCCGCAGTAC 660
sequance_from_insilico_reverse_transcription    GGCTTCGGCGACTACGTGGCCCTGCAGAAGGACCAGGCCCTGCAGACCCAGCCCCAGTAC 660
                                                ******************** ***************** ***** ** ***** ******

native_sequence_joint_exons_1_2                 GTGGCCTTCAGCTTCGTCTACATCCTCACCGGCCTCACGGTCATCGGCGCCTTCCTCAAC 720
sequance_from_insilico_reverse_transcription    GTGGCCTTCAGCTTCGTGTACATCCTGACCGGCCTGACCGTGATCGGCGCCTTCCTGAAC 720
                                                ***************** ******** ******** ** ** *************** ***

native_sequence_joint_exons_1_2                 CTCGTGGTGCTGCGCTTCATGACCATGAACGCCGAGGACGAGAAGCGCGACGCCGAGCAC 780
sequance_from_insilico_reverse_transcription    CTGGTGGTGCTGAGGTTCATGACCATGAACGCCGAGGACGAGAAGAGGGACGCCGAGCAC 780
                                                ** ********* * ******************************** * ************

native_sequence_joint_exons_1_2                 CGCGCGCTGCTCACGCGCAACGGGCAGGCGGGCGGGGCCTGCGGCGGCGGCGGCGGGGGT 840
sequance_from_insilico_reverse_transcription    AGGGCCCTGCTGACCAGGAACGGCCAGGCCGGCGGCGCCTGCGGCGGCGGCGGCGGCGGC 840
                                                 * ** ***** **  * ***** ***** ***** ******************** **

native_sequence_joint_exons_1_2                 GGCGCGGGCGGCAGCGCGCACACCACGGACACCGCCTCGTCCACGGTGGCGGCCGGCGGC 900
sequance_from_insilico_reverse_transcription    GGCGCCGGCGGCAGCGCCCACACCACCGACACCGCCAGCAGCACCGTGGCCGCCGGCGGC 900
                                                ***** *********** ******** *********     *** ***** *********

native_sequence_joint_exons_1_2                 GGCGGCGGCGGCTTCCGCAACGTGTATGCCGAGGTGCTGCACTTCCAGTCCATGTGCTCG 960
sequance_from_insilico_reverse_transcription    GGCGGCGGCGGCTTCAGGAACGTGTACGCCGAGGTGCTGCACTTCCAGAGCATGTGCAGC 960
                                                *************** * ******** ********************  *******

native_sequence_joint_exons_1_2                 TGCCTCTGGTACAAGAGCCGCGAGAAGCTGCAGTACTCCATCCCCATGATCATCCCGCGG 1020
sequance_from_insilico_reverse_transcription    TGCCTGTGGTACAAGAGCAGGGAGAAGCTGCAGTACAGCATCCCCATGATCATCCCCAGG 1020
                                                ***** ************ * ****************  ******************  **

native_sequence_joint_exons_1_2                 GACCTCTCCACGTCCGACACATGCGTGGAGCAGAGCCACTCGTCGCCGGGAGGGGGCGGC 1080
sequance_from_insilico_reverse_transcription    GACCTGAGCACCAGCGACACCTGCGTGGAGCAGAGCCACAGCAGCCCCGGCGGCGGCGGC 1080
                                                *****   ***   ****** ******************      ** ** ** ******

native_sequence_joint_exons_1_2                 CGCTACAGCGACACGCCCTCGCACCGCTGCCTGTGCAGCGGGGCGCAGCGCTCCGCCATC 1140
sequance_from_insilico_reverse_transcription    AGGTACAGCGACACCCCCAGCCACAGGTGCCTGTGCAGCGGCGCCCAGAGGAGCGCCATC 1140
                                                 * ************ ***   *** * *************** ** *** *   *******

native_sequence_joint_exons_1_2                 AGCTCGGTGTCCACGGGCCTGCACAGCCTGTCCACCTTCCGCGGCCTCATGAAGCGCAGG 1200
sequance_from_insilico_reverse_transcription    AGCAGCGTGAGCACCGGCCTGCACAGCCTGAGCACCTTCAGGGGCCTGATGAAGAGGAGG 1200
                                                ***   ***  *** ***************  ******* * ***** ****** * ***

native_sequence_joint_exons_1_2                 AGCTCCGTA    1209
sequance_from_insilico_reverse_transcription    AGCAGCGTG    1209
                                                ***  ***
```

4 Primer designs

No.	Oligo Name	Sequence (5' -> 3')	Yield [OD]	Yield [µg]	Yield [nmol]	Concentration [pmol/µl]	Vol. for 100pmol/µl	Tm [°C]	MW [g/mol]	GC-Content	Synthesis Scale	Purification
1	T1_N250stop_F	CTGCGCTTCATGACCATGTGAGCCGAGGACGAGAAGCGC (39)	17.31	487	40.4	-	404	> 75	12043	61.5 %	0.05 µmol	HPSF
2	T1_N250stop_R	GCGCTTCTCGTCCTCGGCTCACATGGTCATGAAGCGCAG (39)	19.19	571	47.8	-	478	> 75	11936	61.5 %	0.05 µmol	HPSF
3	T1_L135F_R137K_F	GGCGAGCGCATCAACACCTTCGTGAAGTACCTGCTGCACCGCGCCAAG (48)	22.02	631	42.9	-	429	> 75	14708	62.5 %	0.05 µmol	HPSF
4	T1_L135F_R137K_R	CTTGGCGCGGTGCAGCAGGTACTTCACGAAGGTGTTGATGCGCTCGCC (48)	21.28	625	42.1	-	421	> 75	14833	62.5 %	0.05 µmol	HPSF
5	T1_H180Y_F	GCCGCCGCCTTCTCCTATTACGAGCACTGGACC (33)	18.09	550	55.1	-	551	> 75	9986	63.6 %	0.05 µmol	HPSF
6	T1_H180Y_R	GGTCCAGTGCTCGTAATAGGAGAAGGCGGCGGC (33)	16.48	458	44.5	-	445	> 75	10285	63.6 %	0.05 µmol	HPSF
7	T1_K145R_F	TACCTGCTGCACCGCGCCAAGAGAGGGCTGGGCATG (36)	18.10	518	46.6	-	466	> 75	11112	66.7 %	0.05 µmol	HPSF
8	T1_K145R_R	CATGCCCAGCCCTCTCTTGGCGCGGTGCAGCAGGTA (36)	17.97	538	48.9	-	489	> 75	11014	66.7 %	0.05 µmol	HPSF
9	T1_L35M_F	TGGAGTCGGAGCCCGAGATGATCGAGCGGCAG (32)	14.98	414	41.5	-	415	> 75	9980	65.6 %	0.05 µmol	HPSF
10	T1_L35M_R	CTGCCGCTCGATCATCTCGGGCTCCGACTCCA (32)	16.93	523	54.1	-	541	> 75	9673	65.6 %	0.05 µmol	HPSF